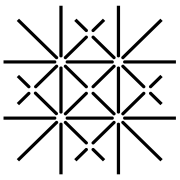

Universität Basel

Ultra-Fast Spectroscopy on Single Self-Assembled Quantum Dots with Rapid Adiabatic Passage

Inauguraldissertation

zur Erlangung der Würde eines Doktors der Philosophie
vorgelegt der
Philosophisch-Naturwissenschaftlichen Fakultät
der Universität Basel von

Timo Kaldewey
aus Wesel, Deutschland

Basel, January 2017

Genehmigt von der Philosophisch-Naturwissenschaftlichen Fakultät
auf Antrag von
Prof. Dr. Richard J. Warburton
Prof. Dr. Anthony Mark Fox

Basel, den 13. Dezember 2016

Prof. Dr. Jörg Schibler
Dekan

Creative Commons License Deed

Attribution-NonCommercial-NoDerivatives 4.0 International

This is a human-readable summary of (and not a substitute for) the license.

You are free to:

Share — copy and redistribute the material in any medium or format

The licensor cannot revoke these freedoms as long as you follow the license terms.

Under the following terms:

Attribution — You must give appropriate credit, provide a link to the license, and indicate if changes were made. You may do so in any reasonable manner, but not in any way that suggests the licensor endorses you or your use.

NonCommercial — You may not use the material for commercial purposes.

NoDerivatives — If you remix, transform, or build upon the material, you may not distribute the modified material.

No additional restrictions — You may not apply legal terms or technological measures that legally restrict others from doing anything the license permits.

Notices:

You do not have to comply with the license for elements of the material in the public domain or where your use is permitted by an applicable exception or limitation.

No warranties are given. The license may not give you all of the permissions necessary for your intended use. For example, other rights such as publicity, privacy, or moral rights may limit how you use the material.

Abstract

Self-assembled semiconductor quantum dots are often referred to as artificial atoms. They are bright single photon sources implemented in an environment easier scalable then implementations with single atoms. These properties promote quantum dots as promising candidates for quantum information technology. A high fidelity state preparation reduces the error rate in quantum information protocols and is hence an essential requirement.

In this thesis the technique of rapid adiabatic passage is implemented with ultra-fast pulse parameters and is used to study single self-assembled quantum dots by detecting the resonance fluorescence signal following an optical excitation. Different experimental schemes provide insights into different aspects of a quantum dot and its environment.

The negative trion transition in a single quantum dot represents a good approach to creating an ideal two-level system. With this two-level system, the interaction of the electron trapped in the QD and phonons in the host material is studied with a single chirped pulse. Measuring the resonance fluorescence response of the quantum dot as a function of the pulse area for a set of chirp parameters reveals the electron-phonon interaction. Phonons in the semiconductor environment are a source of decoherence. The non-monotonic behaviour of the coupling to phonons is experimentally demonstrated. Furthermore, a decoupling regime where the electron oscillation is too fast for phonons to follow is reached. A high fidelity state preparation with a vanishing coupling to phonons is demonstrated. Experimental results are affirmed with an excellent agreement with simulations.

In another scheme, a three-level system consisting of the crystal ground state of the quantum dot, the neutral exciton and the biexciton is investigated. The goal in this experiment is a coherent, resonant and high fidelity preparation of a biexciton state robust against system parameter fluctuations. A biexciton in a semiconductor quantum dot is a source of polarization-entangled photons with high potential for implementation in scalable systems. An excitation with chirped pulses applying the technique of rapid adiabatic passage is the key for the biexciton preparation scheme. In contrast to other state of the art techniques, an interaction with phonons is here intentionally minimized reducing the dephasing and maintaining at the same time a robustness with respect to pulse area and detuning. A fidelity close to one is reached over a pulse area range of more than π. Also in this case, the interpretation of the experiment is confirmed by an excellent agreement with simulations which include a microscopic coupling to phonons.

In a third experiment, a sequence of two chirped pulses with different point spread functions is used to overcome the diffraction limit in spectroscopy. A universal technique — optical nanoscopy via quantum control — to perform diffraction-unlimited spectroscopy on two-level systems is presented. A model for simulating the system is developed and gives a prediction for the expected spatial resolution as a function of the pulse parameters. The concept is demonstrated and the prediction is fulfilled on self-assembled semiconductor quantum dots. A resolution down to 30 nm with an excitation wavelength of 950 nm is reached.

Contents

Part I

Introduction

1 Quantum Dots

Self-assembled semiconductor quantum dots (QDs) are often referred to as artificial atoms. Although they consist of 10^5 atoms, they behave in many ways like single atoms. They feature a discrete level structure opening an easy access to the world of quantum physics. Famous experiments from two-level systems in atomic physics were already successfully performed on single quantum dots as for example: Rabi oscillation [Stievater et al., 2001; Zrenner et al., 2002; Stufler et al., 2005; Krenner et al., 2005; Stufler et al., 2006a; Zecherle et al., 2010; Ramsay et al., 2010b,a], resonance fluorescence [Vamivakas et al., 2009], Zeeman splitting [Jovanov et al., 2012], photon antibunchingMichler et al. [2000] and the Mollow triplet. QDs are bright single photon sources implemented in easily scalable semiconductor diodes [He et al., 2013]. The control of quantum properties promotes quantum dots as promising candidates for quantum information technology [Loss and DiVincenzo, 1998; Gisin et al., 2002]: they are suitable entities for quantum computing [Zrenner et al., 2002]. Furthermore, they form an excellent interface between flying qubits (photons) and anchored matter-spin qubits (electron or hole spin).

1.1 Self-Assembled Quantum Dots

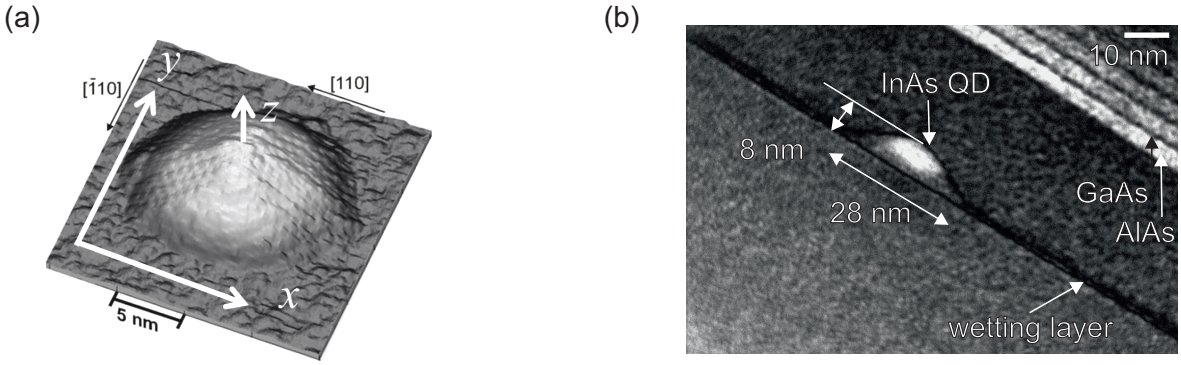

Figure 1.1.1: **A self-assembled InAs quantum dot.** Image taken with **(a)** a scanning tunnelling microscope (STM) [Márquez et al., 2001] and **(b)** with a transmission electron microscope (TEM) [Jean-Michel Chauveau, Arne Ludwig].

We begin with a very brief introduction to the optical and electrical properties of self-assembled quantum dots. Self-assembled InGaAs quantum dots grow in the Stranski-Krastanov mode in molecular beam epitaxy. The growth process takes place in two steps. In the first step, a complete film of a InAs monolayer (ML) grow on a GaAs substrate. This two dimensional quantum well is the so-called wetting layer. After a critical thickness of around 1.6 ML is reached, InGaAs islands begin to form, induced by strain and energy minimization [Goldstein et al., 1985]. The QDs are 'born'. A scanning tunnelling microscope (STM) image of a self-assembled InAs QD is shown in Figure 1.1.1(a). The geometry has the shape of a lens and typically features a height of about 5 nm and a diameter of around 20 nm to 50 nm. Figure 1.1.1(b) shows a cross-section of an InAs QD taken with a transmission electron microscope (TEM). The wetting layer on top of the substrate is shown as well as the QD capped with a layer of GaAs. The periodic structure on top of the capping layer is a superlattice preventing a current flow through the device (see Section 1.2).

Since charge carriers in quantum dots experience a confinement in all three dimensions, quantum dots are called quasi-zero dimensional nanostructures. The electronic bandstructure is schematically depicted in Figure 1.1.2. The bandstructure in the growth direction (z) has a different confinement potential than in the (x,y)-direction: in the (x,y)-plane (Fig. 1.1.2(a)) it can, to a good approximation, be described as a two dimensional harmonic oscillator [Warburton et al., 1998]; however, in the growth direction (z) (Fig. 1.1.2(b)) it is formed by the potential wells of both the wetting layer and the quantum dot (a two step like behaviour in 1.1.2(b)). At low temperatures, the conduction band is empty while the valence band is completely filled with electrons. In the experiments covered in this thesis, the QDs were kept at a sample temperature of 4.2 K, and hence the neutral ground state corresponds to an empty conduction band.

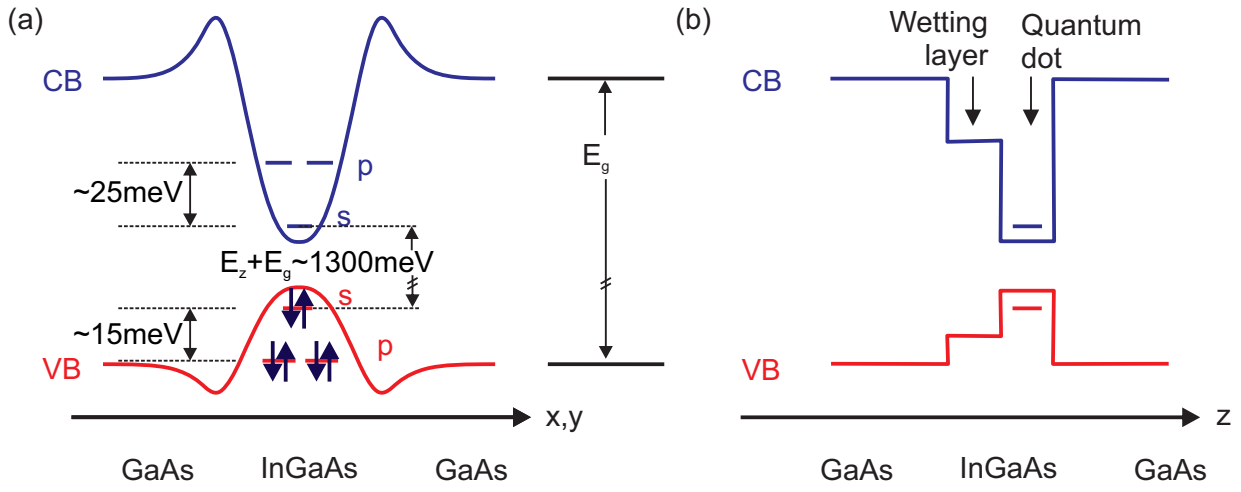

Figure 1.1.2: **Schematic electronic bandstructure of a self-assembled quantum dot.** In the crystal ground state, the energetic higher conduction band (CB) is empty and the energetic lower valence band (VB) is fully occupied. Discrete energy states are depicted as horizontal lines. **(a)** Perpendicular to the growth direction: (x,y)-plane. **(b)** In growth direction: z. Adapted from [Kaldewey, 2012].

The confinement, on the order of the de Broglie wavelength of the electrons, results in discrete energy levels as depicted in Figure 1.1.2. Each level can be occupied by at most two electrons due to the Pauli exclusion principle. Interband transitions can be efficiently driven by photons without involving phonons since the compound materials GaAs and InGaAs are semiconductor materials with a direct band gap. The band gap of InGaAs varies between ∼1.0 eV and ∼1.4 eV depending on the In concentration and allows an optical excitation with a near-infrared laser. In case of a resonant excitation, a photon is absorbed by the QD and one electron (blue arrow) is excited from the highest energy-level of the valence band into the lowest energy-level of the conduction band. The missing electron in the valence band can formally be treated as a hole (red arrow). This electron hole pair forms a quasi particle, the neutral exciton, X^0, as depicted in Figure 1.1.3(a). The crystal ground state and the exciton state form together a two-level system which serves as a qubit in quantum information technology.

Summarized, if the QD is resonantly excited with laser light, a dipole transition from the crystal ground state to the single exciton state is driven. The energy needed for this transition is determined by the energy separation of the initial and final electron level. The spin of the electron and hole is determined by the optical polarisation.

In a two-photon process two electrons are excited. Laser light of high intensity, or alternatively two laser pulses, generates two electron hole pairs. The state formed by two electrons in the conduction band and two holes in the valence band, illustrated in 1.1.3(b), is called the biexciton, $2X^0$. The biexciton decays radiatively in a cascade of two photons. The energy of the first emitted photon E_{2X^0} differs from the energy of the second emitted photon E_{X^0} by the exciton binding

energy E_B. The biexciton energy is among other contributions a result of the Coulomb interaction between electrons and holes in the QD. The sign and magnitude depends on the quantum dot size and on the growth conditions [Young et al., 2005; Langbein et al., 2004]. The biexciton binding energy of InGaAs QDs lies typically in the order of a few meV [Young et al., 2005; Rodt et al., 2005; Langbein et al., 2004].

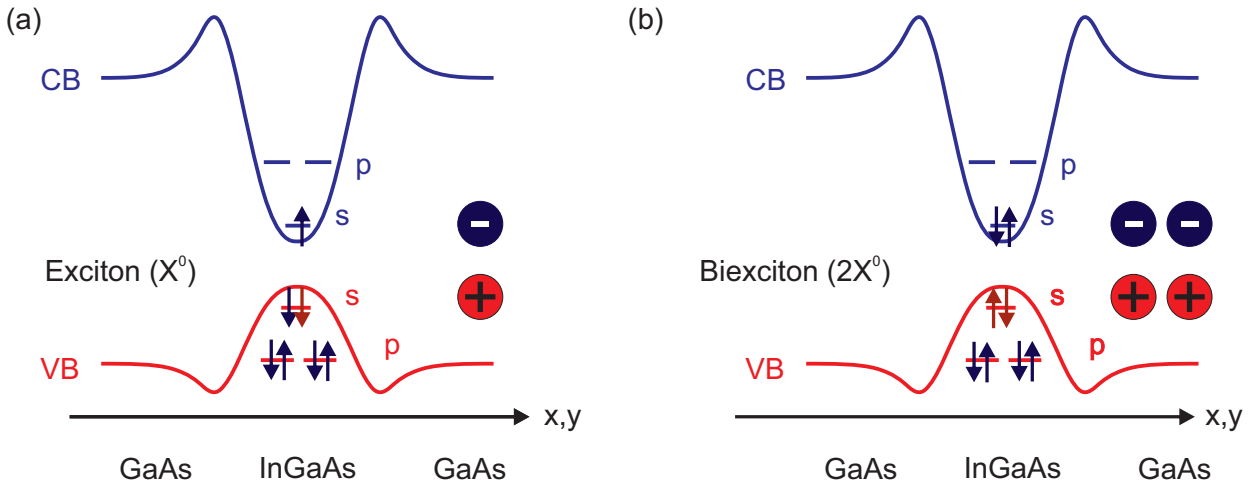

Figure 1.1.3: **Electron hole pairs in a QD.** (a) Schematic illustration of an optically excited electron hole pair in the quantum dot bandstructure: the neutral exciton. The electron is depicted with a blue arrow in the conduction band (CB) and the hole with a red arrow in the valence band (VB). (b) Two electron hole pairs form a biexciton. A more simplified description of the charge situation in the QD is depicted on the right side of each panel using + and - charges instead of arrows, neglecting the spin. Adapted from [Kaldewey, 2012].

1.2 Quantum Dots Embedded in a Diode Heterostructure

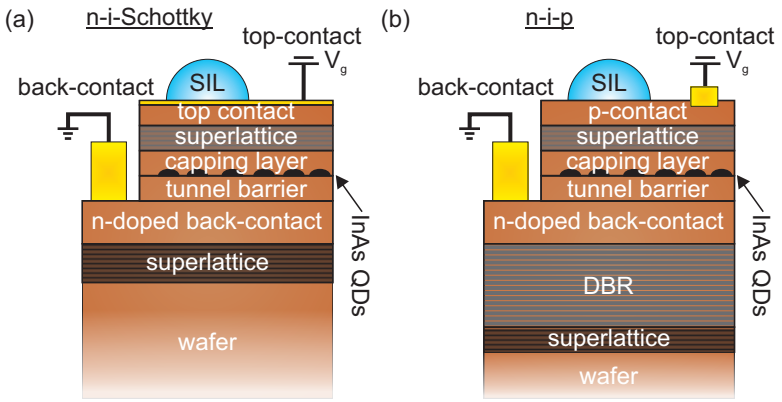

Figure 1.2.1: **Quantum dots embedded in heterostructures, layer structure.** (a) n-i-Schottky diode and (b) n-i-p diode.

Semiconductor quantum dots are often embedded into a diode structure allowing for a control of electric fields experienced by the QDs as well as a control of charge states. The diode consists mainly of three parts: the top gate, a layer with QDs and a back gate.

In the framework of this PhD thesis III-V semiconductor self-assembled InGaAs quantum dots (QD) were studied in four samples from two different heterostructures: Bo14598 and Bo13759, as listed in Table 1.2.1. In both cases the QDs are embedded in a GaAs diode grown by molecular

beam epitaxy in the group of Prof. Andreas Wieck at the Ruhr-Universität Bochum, Germany. The first one is an n-i-Schottky diode [Drexler et al., 1994; Warburton et al., 2000] (Bo13759) and the second is an n-i-p diode [Prechtel et al., 2016] (Bo14598), Figure 1.2.1(a) and (b), respectively.

The first sample, the n-i-Schottky diode, consists of an n-doped back-contact and a semi-transparent metallic top-contact (Ti/Au 3 nm/7 nm). The n-i-p sample on the other hand has an epitaxial top gate made from carbon-doped GaAs instead of a metallic top gate. A final layer of 44 nm undoped GaAs places the epitaxial top gate around a node-position of the standing electromagnetic wave in the n-i-p diode. A selective etching of the capping allows contacts to be made to the buried p-layer. Access to the n-layer is provided in both samples by wet etching of a mesa structure around the solid immersion lens (SIL) (see Section 2.2.1). The n-i-p diode additionally features a distributed Bragg reflector (DBR) which increases the collection efficiency of photons.

Beside these main differences, both heterostructures have similar features. The first superlattice following the GaAs wafer (and buffer) smooths the surface and keeps impurities from the wafer polishing process away from the relevant QD layer. The electron reservoir (the n-doped layer) together with the tunnel barrier allow in both heterostructures a controlled loading of single electrons into the QD by means of the gate voltage. In both devices the n-contact is grounded and a gate voltage V_g is applied to the Schottky gate or p-contact. The gate voltage allows control over the charge characteristics: in the Coulomb blockade regime single electrons can be loaded one by one into the QD and excitonic resonances can be shifted by the DC Stark effect [Warburton et al., 2000; Dalgarno et al., 2008; Warburton, 2013]. The bias leads to a tilt of the bandstructure in the diode and hence moves the energy levels in the conduction band of the QD above or below the Fermi level loading one additional electron into the QD or removing it. The calculated bandstructure and the Fermi level (green) of the n-i-p diode are shown in Figure 1.2.2. The blocking barrier (short period superlattice, SPS) blocks a current flow through the diode.

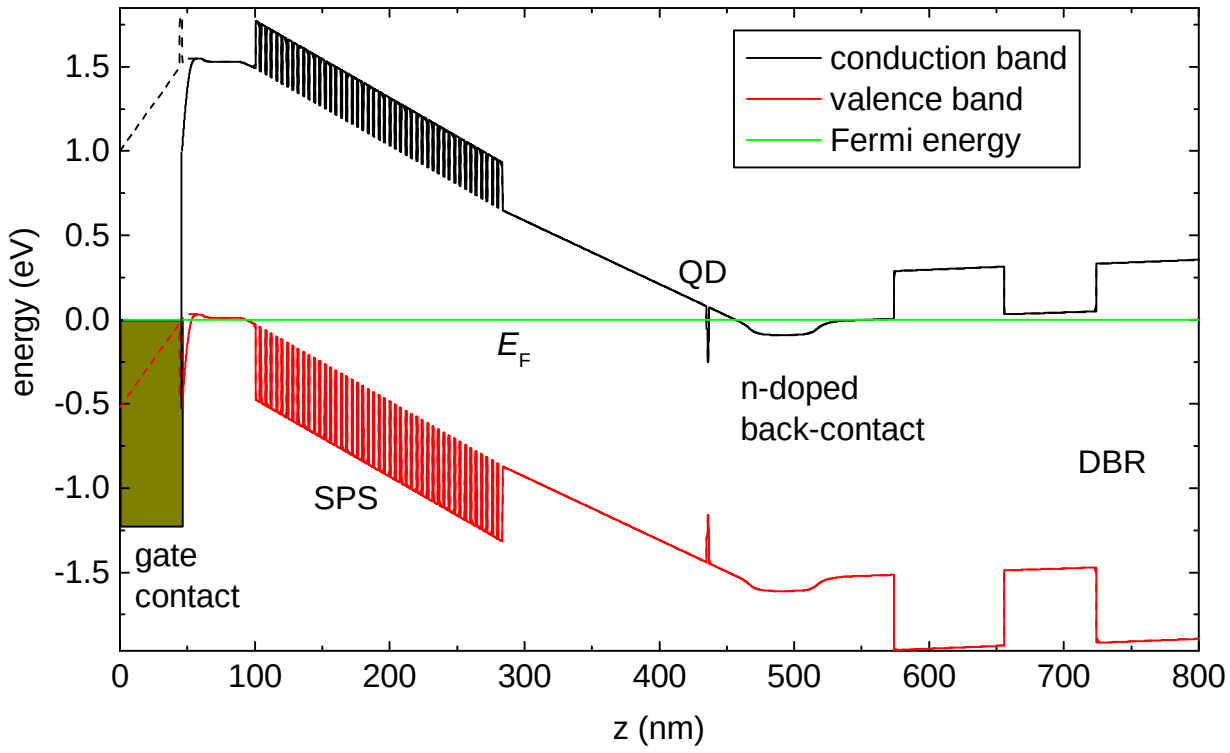

Figure 1.2.2: **Bandstructure of the n-i-p diode along the growth direction z.** The alternating structure in the left part is the short period superlattice (SPS) preventing a current flow. The right part shows the first periods of the distributed Bragg reflector (DBR). Figure provided by Arne Ludwig, University of Bochum, Germany.

Both heterostructures were grown with a wafer rotation stop during the In-flushing, resulting in a gradient of the QD density on the wafer. The nominal QD density in the workhorse in this thesis, sample Bo14598h, is $10^8\,\mathrm{cm}^{-2}$. The complete layer structures for the n-i-Schottky diode and the n-i-p diode are given in Table 1.2.2 and Table 1.2.3, respectively.

n-i-Schottky: Bo13759	n-i-p: Bo14598
Bo13759#12	Bo14598g
	Bo14598e
	Bo14598h

Table 1.2.1: **List of quantum dot samples studied in this PhD thesis.**

wafer	GaAs	
buffer	GaAs	50 nm
superlattice, 30 periods	AlAs, GaAs 2 nm each	120 nm
	GaAs	50 nm
electron reservoir, back contact	GaAs:Si	50 nm
tunnel barrier	GaAs	25 nm
InGaAs QDs	InAs	∼1.6 ML
capping layer	GaAs	150 nm
blocking barrier, 68 periods	AlAs, GaAs	272 nm
cap	GaAs	10 nm

Table 1.2.2: **Layer structure of the n-i-Schottky diode.** Quantum dots (QDs) are formed by depositing 1.6 monolayers (ML) of InAs.

wafer	GaAs	
buffer	GaAs	50 nm
superlattice, 18 periods	GaAs, AlAs 2 nm each	72 nm
DBR, 16 periods	GaAs, AlAs	2400 nm
	GaAs	57.3 nm
electron reservoir, back contact	GaAs:Si	50 nm
tunnel barrier	GaAs	30 nm
InGaAs QDs	InAs	∼1.6 ML
capping layer	GaAs	153 nm
blocking barrier, 46 periods	AlAs, GaAs	184 nm
p-doped top contact	GaAs:Si	30.5 nm
	GaAs	1 nm
etch stop	AlAs	2 nm
places p-layer to an field node	GaAs	44 nm

Table 1.2.3: **Layer structure of the n-i-p diode.** Quantum dots (QDs) are formed by depositing 1.6 monolayers (ML) of InAs. The distributed Bragg reflector (DBR) increases the collection efficiency.

The performance of the QDs in both diode structures is quite similar. The main advantage of the n-i-p diode over the n-i-Schottky device is a strongly enhanced photon collection. This is achieved on the one hand by the DBR which reflects photons emitted downwards. On the other hand, the absorption of photons in the top-gate is reduced by an epitaxial gate. The epitaxial gate is transparent for near-infrared photons in contrast to a metal gate.

1.3 Quantum Confined Stark Effect

The dc Stark effect is known from atom physics; it shifts the energy levels of atoms in a static electric field.

In semiconductor heterostructures, the Stark effect occurs due to internal electric fields (e.g. charge noise, Houel et al. [2012]) as well as external applied electric fields and is known as the Quantum Confined Stark Effect (QCSE). The shift of discrete energy levels changes the resonance condition in the resonant fluorescence spectroscopy as a function of the resulting field. Typical values obtained in our measurements on InGaAs QDs are $\mathrm{d}E/\mathrm{d}V_g = 55\,\mathrm{meV/V}$.

The QDs in this work are embedded in a diode (see Section 1.2). The resulting field experienced by the QDs is controlled and varied by applying a voltage to the diode. The resulting field in the diode can be calculated from the diffusion potential, the so called 'built-in' potential V_{bi}, the applied gate voltage V_g and the distance d from the sample's top contact to the n-doped layer:

$$F = \frac{V_g - V_{\mathrm{bi}}}{d}. \tag{1.3.1}$$

The built-in potential is the difference of the potentials across a p-n or Schottky junction without an external applied field [Groß, 2012]. It can experimentally be estimated by recording the I-V-characteristic of the diode, it corresponds roughly to the knee voltage obtained in forward direction as shown in Figure 1.3.1. From perturbation theory, one can deduce the shifted eigenenergies as a function of the electric field F:

$$E(F) = E_0 - p_{\mathrm{int}}F - \alpha F^2, \tag{1.3.2}$$

where E_0 is the eigenenergy without an internal field, p_{int} is the electric dipole moment and α is the polarisability. More details about the QCSE can be found for example in [Fox, 2010].

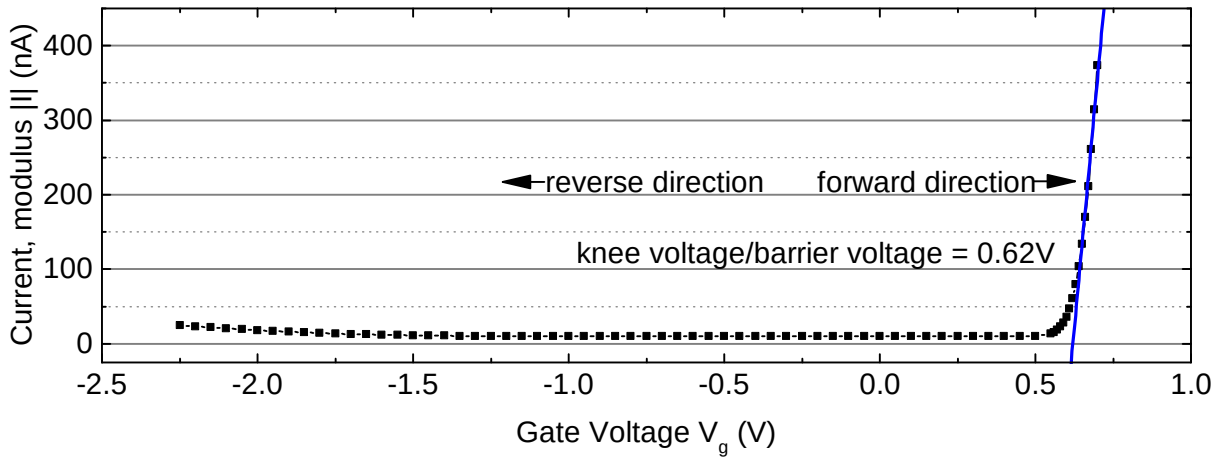

Figure 1.3.1: **Diode characteristic of sample Bo14598h.** The figure shows the absolute value of the current measured as function of the applied gate voltage. A linear curve (blue, solid line) is fitted to the forward current. The intersection with the x axis is the knee voltage.

1.4 Other Excitonic States - Charged States

As mentioned earlier, we study QDs at liquid helium temperature of 4.2 K. At low temperature, the number of electrons in the quantum dot's ground state can be controlled by means of the applied gate voltage V_g [Warburton et al., 2000; Ediger et al., 2005; Dalgarno et al., 2008; Warburton, 2013]. Figure 1.4.1(a) shows the spectrally resolved photoluminescence (PL) as a function of the applied gate voltage. The map shows clearly four bright plateaus in the photon energy. We identified and labelled them as the radiative transitions from an excited state (triply negatively charged exciton

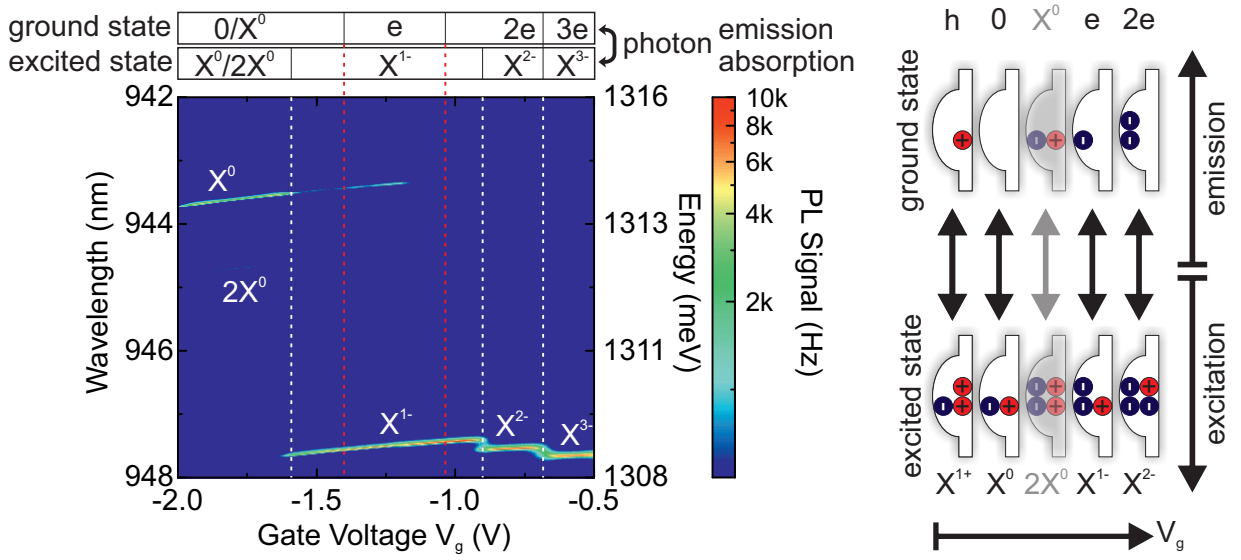

Figure 1.4.1: **Charge states in a quantum dot embedded in a diode. (a)** Photoluminescence (PL) as a function of the gate voltage applied to the diode. The QD in sample Bo13759#12 was excited non-resonantly with a wavelength of 830 nm, wetting layer excitation. **(b)** Sketch of different optical transitions.

(X^{3-}), doubly negative charged exciton (X^{2-}), negatively charged exciton (X^{1-}) and neutral exciton (X^0)) to the ground state (three electrons, two electrons, one electron and zero electrons in the QD, respectively). The pattern of discrete steps is caused by the Coulomb blockade. The electron repulsion due to the electron-electron Coulomb interaction in the nanoscale QD is stronger than the thermal energy K_B at low temperatures of 4.2 K. The Coulomb blockade prevents other electrons to flow [Warburton et al., 2000]. The concrete tunnel process of electrons into the QD and out of the QD as function of the gate voltage is reviewed in [Warburton, 2013]. Furthermore, the Figure shows also a much weaker PL emission from biexciton, $2X^0$, generated by a two-photon excitation. A sketch summarising the optical transitions for different charge levels is shown in Figure 1.4.1(b).

1.5 Optical Selection Rules

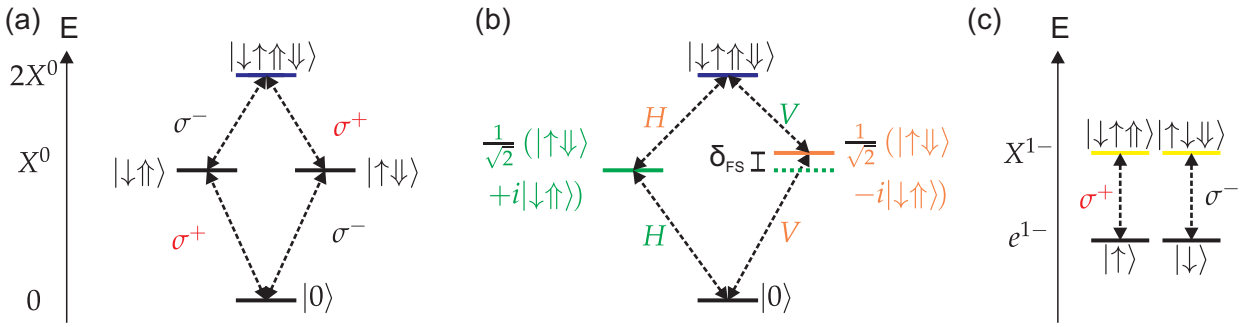

Figure 1.5.1: **Optical selection rules (a)** Exciton - Biexciton system in a symmetric QD driven by circularly polarised light and **(b)** in an asymmetric QD with fine structure splitting δ_{FS} driven by linearly polarised light. **(c)** Negative trion driven with circularly polarised light.

So far we neglected the spin of the photon as well as of the optically created electron hole pair. We give here a very short overview of relevant allowed transitions. More details can be found for example in Fox [2006, p. 54 ff.]. The exciting photon is a bosonic particle and, as a consequence, it carries a spin of 1. The electron on the other hand is a fermion, a spin 1/2 particle

$(S, S_z = 1/2, \pm 1/2)$. The electron and hole in a semiconductor can occupy different bands which can be approximately described by the effective mass model, the $\mathbf{k} \cdot \mathbf{p}$ model [Groß, 2012]. The hole in a semiconductor such as GaAs has contributions from different bands: the heavy-hole band, the light-hole band and the spin-off band. In the ground state, the dominant contribution comes from the heavy hole band with $J, J_z = 3/2, \pm 3/2$. Neglecting the other contributions to the hole wave function, the neutral bright exciton can accommodate two possible spin configurations of the electron hole pair. Here, the electron spin and the hole spin are anti-parallel: $\uparrow$ $(+1/2)$, $\Downarrow$ $(-3/2)$ or $\downarrow$ $(-1/2)$, $\Uparrow$ $(+3/2)$ for electron and heavy hole, respectively. These two spin states are almost energetically degenerate in a symmetric QD [Stufler et al., 2006a] besides a small splitting caused by the inversion asymmetry of the GaAs lattice. The excitation with left- and right-circularly polarised light (σ^+, σ^-) is shown for the exciton in Figure 1.5.1(a) The excitation with linear polarisation (H, V) is shown in 1.5.1(b) for an asymmetric QD with a fine structure splitting (FSS) δ_{FS}. Depending on the In concentration in the InGaAs QD the shape of the dot changes from round, symmetric to elliptical, asymmetric [Li et al., 2000b]. This asymmetry leads to a FSS and hence, a lift of the degeneracy [Bayer et al., 1999; Gammon et al., 1996] of the exciton spin states. The two eigenstates in an asymmetric QD can be excited with a set of two orthogonal linear polarisations: horizontal polarisation (H) and vertical polarisation (V). In case of a large FSS ($\delta_{\mathrm{FS}} > 30\,\mu\mathrm{eV}$), these polarisations tend to lie along the major axis $[\bar{1}10]$ and the minor axis $[110]$ of the QD (see Fig. 1.1.1) [Seidl et al., 2008]. On the other hand, H and V vary from dot to dot for a small FSS. Typical values of the FSS for InGaAs QDs are around $20\,\mu\mathrm{eV}$.

The optical excitation of the negative trion state is depicted in Figure 1.5.1(c). The two eigenstates are driven by circularly polarised light.

2 Experimental Set-Up

This chapter introduces the set-up designed and built in the framework of this thesis used to perform all presented pulsed experiments. We start with an overview and discuss further details in the following sub-chapters, dividing the set-up into three main parts:

1. Ultra-short laser pulse generation, manipulation and characterisation
2. The confocal multi-purpose microscope
3. Photon detection and analysis

The scheme in Fig. 2.0.1 gives a simplified overview of the set-up. All the quantum dot experiments were performed at a liquid helium temperature of 4.2 K in a bath cryostat due to superior vibrational performance compared to a flow-cryostat system on an optical table and due to the option to study samples in high magnetic fields. Therefore, the four parts are spatially separated and connected through the multi-purpose confocal microscope and single mode (SM) optical fibres.

A tunable, mode-locked titanium sapphire (Ti:Sa) solid-state laser pumped with a semiconductor laser is used to create ultra-short transform-limited pulses with a repetition rate of 76 MHz. A home-built auto-correlator and frequency-resolved optical gating (FROG) set-up combination determines the pulse duration to be up to 100 fs (full-width-at-half-maximum (FWHM) in intensity). The pulse train from the Ti:Sa laser is expanded in an asymmetric telescope and spatially filtered with a pinhole. The expansion increases the spectral resolution in the subsequent pulse-shaper units and reduces the laser intensity on the optical components. The spatial filter has the purpose to decouple the set-up on the optical table from a beam walking in the laser system while tuning the lasers wavelength or changing the alignment. A half-wave plate ($\lambda/2$) rotates the linear polarisation in order to match the polarisation axis for the best performance of the subsequent optical elements. A small part of the beam is then sent to a mini spectrometer (MS) for mode-locking control and wavelength control.

A plate beamsplitter splits the expanded beam into two. The individual pulse trains were directed into home-built compact pulse-shaper units (PS1, PS2) and chirped by introducing a wavelength dependent phase term. The pulse-shaper provides full control of the sign and magnitude of the chirp.

Following PS1 and PS2, the chirped pulse trains were delayed with respect to each other in a 300 mm delay line leading to a delay of up to 2 ns in a double-pass arrangement. Before coupling the individual pulse trains into SM glass fibres, the power and polarisation are accurately controlled with a combination of neutral density (ND) filters (coarse power control) and a sequence of a half-wave plate, a polariser and, again, a half-wave plate (fine power control and control of the linear polarisation axis). The glass fibres can be plugged into an auto-correlator-FROG unit in order to determine the chirp of the pulses after the SM glass fibres. Also, a free-space analysis of the pulses is possible using a flip mirror (not shown here).

Depending on the exact experiment, pulse trains were sent into one or both of the excitation arms of the multi-purpose confocal microscope. Here, the beams are sent through cube beamsplitters and a laser window to the cold sample in the cryostat. Quantum dots (QDs) can be brought into focus and scanned by a three-axis piezo driven nano-positioning system. Light emitted by a QD is collected through a hemispherical zirconia (ZrO_2) solid immersion lens (Z-SIL) by an objective with an numerical aperture (NA) of 0.68. Back-reflected laser light is filtered from the QD emission by means of a cross-polarised dark-field technique. The signal is coupled into a SM fibre in the

detection arm. Depending on the kind of measurement performed, the signal is spectrally resolved and detected in a spectrometer or with a silicon single-photon avalanche diode (SPAD).

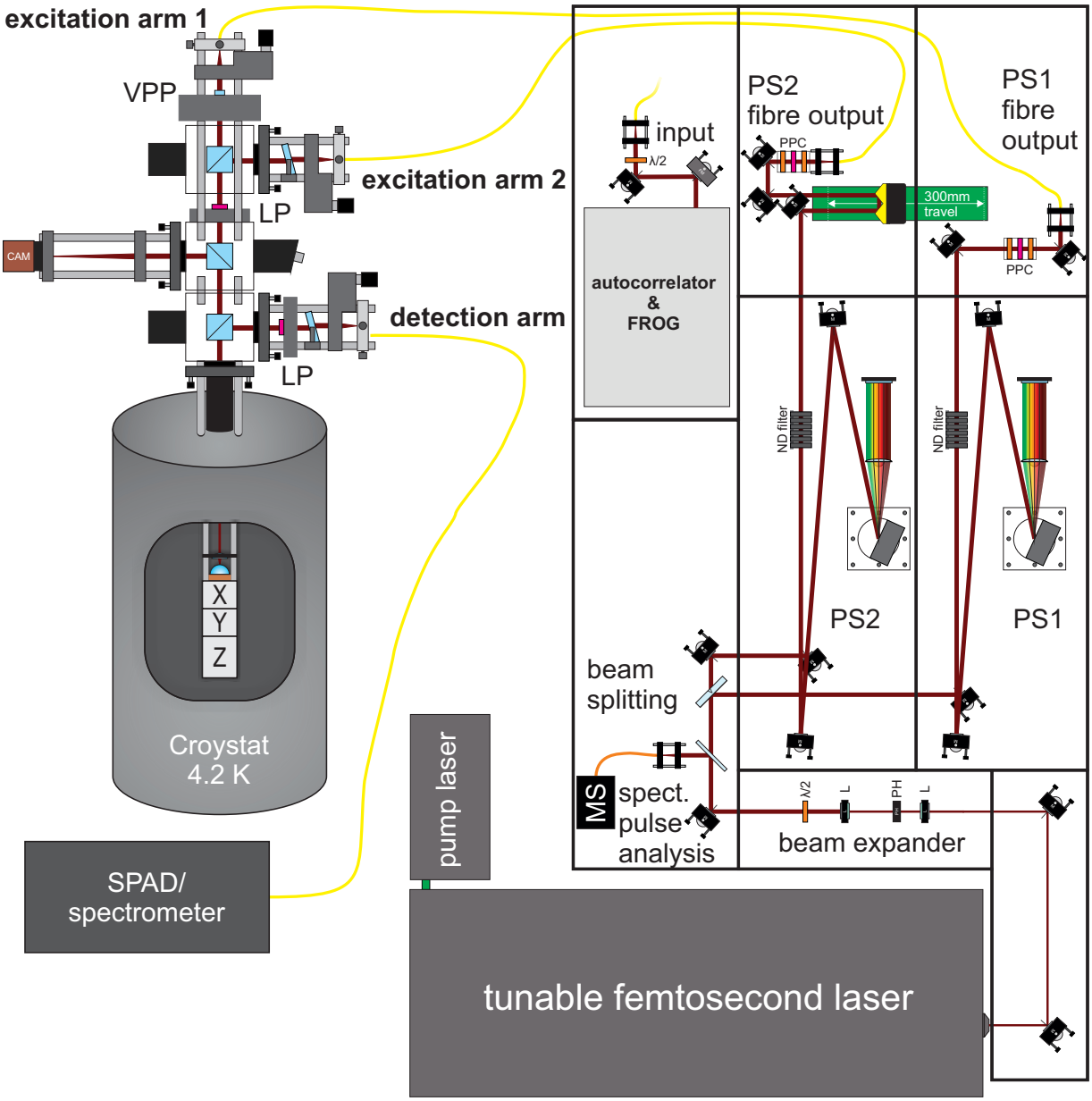

Figure 2.0.1: **Schematic overview of the experimental set-up.** L lens, PH pin-hole, $\lambda/2$ half-wave plate, MS mini-spectrometer, PS pulse-shaper, ND neutral density filter, PPC power-polarization-control, FROG frequency-resolved-optical-gating, VPP vortex phase-plate, LP linear polariser, SPAD single photon avalanche diode.

2.1 Ultra-short Laser Pulse Generation, Manipulation and Characterisation

2.1.1 Ultra-short Laser Pulses

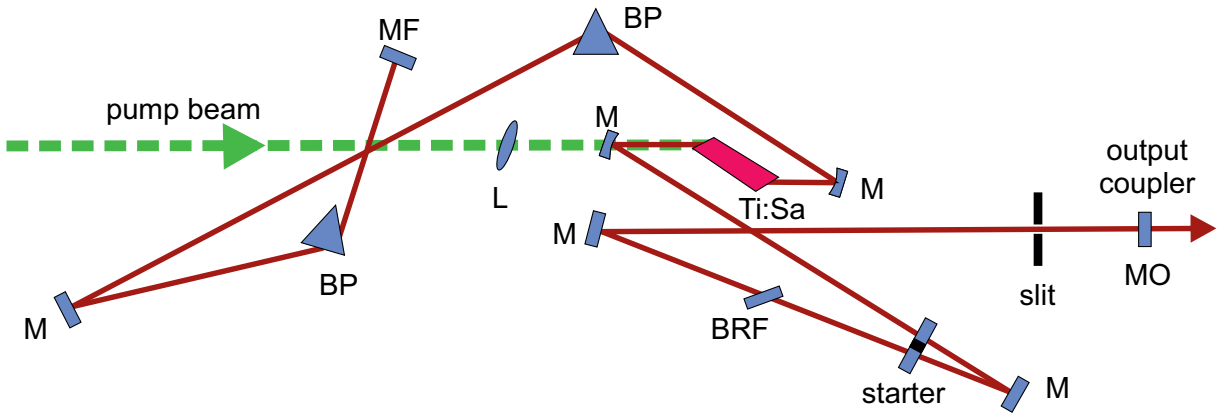

Figure 2.1.1: **Mira 900 Ti:Sa femtosecond laser.** Laser Resonator consists of mirrors (M), birefringent filter (BRF), Brewster prisms (BP) and focussing lens (L).

A passively mode-locked tunable femtosecond laser (Mira900, Coherent) is used to generate pulses with a temporal FWHM in intensity of up to 100 fs. A brief review of the main aspects of the working principle of the laser system is given in this section. A deeper inside can be found, for example, in [Milonni and Eberly, 1988] or [Coherent, 2004].

A green semiconductor laser (Verdi G10, Coherent) pumps the gain medium, a titanium doped Al_2O_3 (corundum) crystal, at a wavelength of 532 nm with up to 10 W. Longitudinal resonator modes, gained by the titanium:sapphire (Ti:Sa) were locked in phase. This mode-locking leads to a pulsing of the laser light emission. The more modes involved, the broader the pulses become in the spectral domain and the shorter in time.

A scheme of the laser resonator is sketched in Fig. 2.1.1. The green laser is focused by the lens (L) into the gain medium (Ti:Sa), which starts to fluoresce. The fluorescence oscillates between the output coupler mirror (MO) and the second final mirror (MF). On every cycle, the light is amplified by stimulated emission and attenuated by losses in the resonantor. At a threshold in pumping, the gain matches the losses and lasing occurs. In the Mira900 laser the mode-locking technique is passive in femtosecond operation; the self-focussing Kerr effect in the gain medium is combined with an optical slit. In this arrangement shorter pulses are privileged; they experience less losses at the optical slit since they are focused more strongly and become dominant in the cavity.

An oscillating glass plate (starter) introduces an initial first pulsing by changing rapidly the resonator length (the optical path length through the plates varies as function of the oscillation). Then the passive mode-locking starts and the system regulates itself (self-phase modulation) to an equilibrium where the modes are locked and ultra-short laser pulses are propagating in the laser resonator. In order to achieve a stable mode-locking, the positive group velocity dispersion experienced in the Ti:Sa crystal and other dispersive elements in the resonator must be compensated otherwise a chirp would be introduced per round-trip. For this purpose, a prism pair (Brewster prisms, BPs) is placed in the laser cavity.

The output coupler mirror (MO) transmits 25% of the propagating intensity out of the resonator into our optical set-up. The combination of a birefringent plate (BRF) with the Brewster prisms (BP) acts as a bandpass-filter (also known as Lyot filter): the resonator mode which is not affected by the BRF and maintains its linear polarization experience less reflection losses on the Brewster windows. A tuning of the laser wavelength is possible by rotating the BRF. The measured out-put

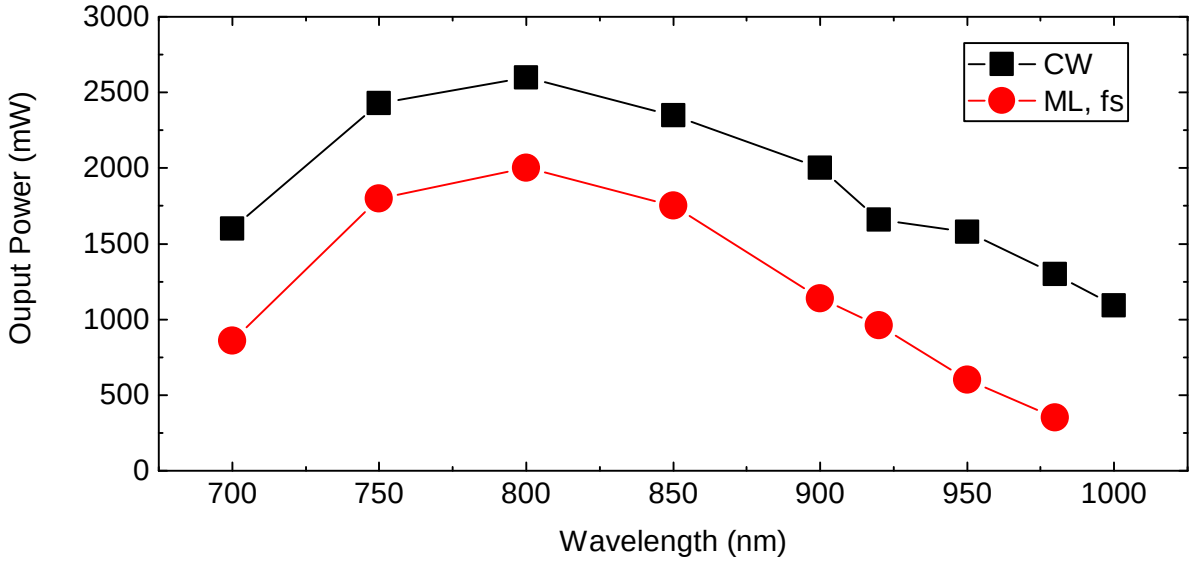

Figure 2.1.2: **Mira 900 output power as function of centre wavelength.** Black data points are measured in continous wave (CW) mode and red data points are measured in mode-locked (ML) operation.

power as function of the centre wavelength is shown in Fig. 2.1.1. It qualitatively reproduces the gain spectrum of the titanium sapphire crystal, having a maximum at 800 nm.

The temporal profile of the laser pulses is best described with a hyperbolic secant [Coherent, 2004]. A good agreement was found between the profile measured with an auto-correlator and a Gauss function, which is similar to the hyperbolic secant. Therefore, a Gauss function is used to describe the temporal as well as the spectral envelope of the pulses. Temporal and spectral domains are related by a Fourier transform. For transform-limited pulses, i.e. for unchirped pulses the time-bandwidth product translates the FWHM in intensity of the pulse duration $\Delta t^I_{\mathrm{FWHM}}$ easily in the FWHM in intensity of the pulses' frequency bandwidth $\Delta\nu^I_{\mathrm{FWHM}}$:

$$\Delta t^I_{0,\mathrm{FWHM}} \times \Delta\nu^I_{0,\mathrm{FWHM}} = 2\ln(2)/\pi \approx 0.44. \tag{2.1.1}$$

The product increases for chirped pulses correspondingly.

2.1.2 Ultra-fast Pulse-Shaping

The key component for the pulse preparation in the presented work is a folded $4f$ pulse-shaper. Pulse-shapers in various designs are used to manipulate femtosecond pulses [Weiner, 2000]. Often the goal is simply to compress pulses that have been undesirably chirped by dispersion in optical elements. Also, more complex manipulations of the pulse characteristics are possible using a phase mask (micro-lithographically fabricated or a programmable liquid crystal) in the focal plane of a pulse-shaper. Depending on the mask, the pulse can be delayed (using a linear mask), stretched or compressed (using a quadratic mask) and even a splitting into two pulses is possible [Weiner et al., 1992].

A very compact and simple form of a pulse-shaper was built: a folded $4f$ design. It contains only three optical elements as sketched in Fig. 2.1.3(a): a high resolution blazed grating (1800 grooves/mm), a cylindrical lens ($f = 150$ mm) and a mirror. An unchirped pulse is directed with two mirrors (mirror 1 and 2) onto a grating and its first order diffraction is then focused by a lens onto the folding mirror. The folding mirror is slightly tilted, hence, the reflected pulse comes back with a small angle (out of the plane of the figure). The transformation of lens and grating is reversed, the beam comes back to mirror 2, then overshoots mirror 1 and is finally picked up by

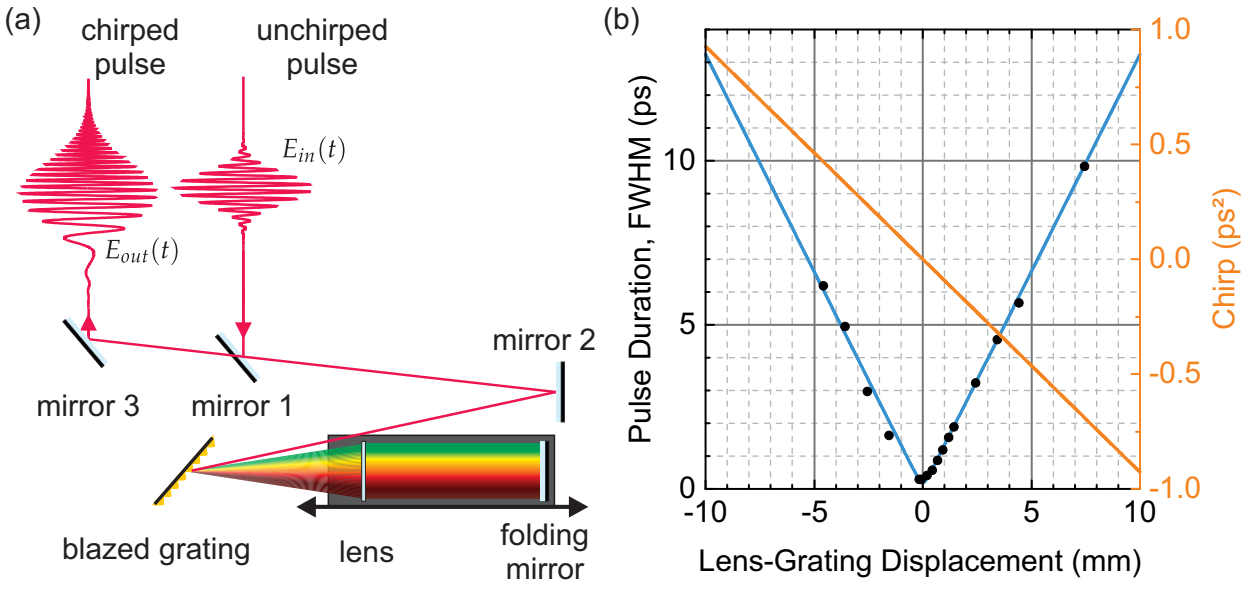

Figure 2.1.3: **Pulse-shaper: concept and performance. (a)** Scheme of our folded $4f$ pulse-shaper. The incident beam is directed with mirror 1 and 2 on a blazed grating, is diffracted and then focused in the focal plane by a cylindrical lens. A folding mirror is placed at the image-side focal plane and reflects the beam with a slight tilt in order to overshoot mirror 1 on the way back. The lens and the folding mirror are mounted on a moving platform enabling the variation of the displacement from grating to lens while keeping the folding mirror lens distance constant. **(b)** Chirped pulse duration as function of the lens-grating displacement, measured after a 8 m long SM fibre with our home-build auto-correlator-FROG combination. For a displacement of zero the lens grating distance matches the focal length and the pulse-shaper is in its zero dispersion setting. The measured data points (black circles) are fitted (blue solid line) using the model described in the text. In addition the calculated chirp is shown in orange (right axis).

mirror 3. In this setting the pulse-shaper has a zero net dispersion: it doesn't change the pulse characteristic.

Instead of the often used phase plate or a spatial light modulator in the focal plane, we use a different approach. We mounted the lens and the folding mirror together on a platform movable with a micrometer linear stage (Fig. 2.1.3(b)). This allows a variation of the grating-lens separation while keeping the folding mirror in the focal plane of the lens. A separation larger than the focal length (positive displacement) introduces a negative chirp, a smaller separation (negative displacement) results in a positive chirp [Martinez, 1987]. We demonstrate in Fig. 2.1.3(b) a stretching of originally transform-limited pulses of a duration of $\Delta t^I_{0,\mathrm{FWHM}} = 130\,\mathrm{fs}$ to more than 10 ps, a factor of 100.

In order to derive a function relating the displacement of the platform to the resulting chirp, we start by recapitulating and defining some basic pulse parameters. As stated earlier, the unchirped pulse can be described with a Gaussian envelope in the time domain:

$$E(t) = E_0 \exp\left(\frac{-t^2}{2\tau_0^2} - i\omega_0 t\right) \tag{2.1.2}$$

$$\Delta t^I_{0,\mathrm{FWHM}} = \tau_0\ 2\sqrt{\ln 2} \tag{2.1.3}$$

whereby ω_0, τ_0 and E_0 are the centre angular frequency of the wave packet, the unchirped pulse

duration and the electric field amplitude, respectively. Equally in the angular frequency domain:

$$E(\omega) = E_0 \tau^2 \exp\left(-\frac{\tau_0^2}{2}(\omega-\omega_0)^2\right) \tag{2.1.4}$$

$$\Delta\omega^I_{0,\mathrm{FWHM}} = \frac{2\sqrt{\ln 2}}{\tau_0}. \tag{2.1.5}$$

The role of the pulse-shaper is to add a phase, individually for each frequency component:

$$E(\omega) = E_0 \tau^2 \exp\left(-\frac{\tau_0^2}{2}(\omega-\omega_0)^2 + i\psi(\omega)\right), \text{ with} \tag{2.1.6}$$

$$\psi(\omega) = \psi_0 + \psi_1(\omega-\omega_0) + \psi_2\frac{(\omega-\omega_0)^2}{2} + O\left(\omega^3\right). \tag{2.1.7}$$

The result is, as mentioned earlier, a delay of the whole wave packet in the case of a linear phase term ($\psi_1 \neq 0$, $\psi_2 = 0$) and a stretching in the case of a quadratic phase contribution ($\psi_2 \neq 0$). We consider here only quadratic contributions. The chirped pulse duration is then a function of the chirp, ψ_2:

$$\Delta t^I_{\mathrm{FWHM}} = \sqrt{\left(\Delta t^I_{0,\mathrm{FWHM}}\right)^2 + \left(\frac{\psi_2\ 4\ln 2}{\Delta t^I_{0,\mathrm{FWHM}}}\right)^2} \tag{2.1.8}$$

$$\tau = \sqrt{\tau_0^2 + \left(\frac{\psi_2}{\tau_0}\right)^2} \tag{2.1.9}$$

The quadratic phase term is directly proportional to the grating-lens displacement in a pulse-shaper [Weiner, 2009, p. 166]:

$$\psi_2 = \frac{\lambda^3(l_1+l_2)}{2\pi c^2 d^2 \cos^2\Theta_D}, \tag{2.1.10}$$

where λ, c, d and Θ_d are the centre wavelength $\lambda = 2\pi c/\omega_0$, the speed of light, the spatial period of the grating and the incidence angle onto the grating, respectively. In our case the displacement s equals $(l_1+l_2)/2$ and hence, putting the fixed parameters in a constant C we can write:

$$\psi_2 = C\ s \tag{2.1.11}$$

$$\Delta t^I_{\mathrm{FWHM}} = \sqrt{\left(\Delta t^I_{0,\mathrm{FWHM}}\right)^2 + \left(\frac{C\ s\ 4\ln 2}{\Delta t^I_{0,\mathrm{FWHM}}}\right)^2}. \tag{2.1.12}$$

The pulse duration $\Delta t^I_{\mathrm{FWHM}}$ was measured as function of the grating-lens separation s as shown in Fig. 2.1.3(b). The relation between the pulse duration and the displacement is fitted to the data (blue curve). The calculated corresponding chirp is shown in orange. From the fit an incident angle of $76.68 \pm 1.00°$ is extracted which matches the angle on the optical table $77.50 \pm 0.89°$ quite well. This result confirms the applicability of eq. 2.1.10. As seen in Figure 2.1.3(b), the pulse-shaper is capable of creating a chirp up to a few ps^2 with positive and negative sign.

An important parameter for rapid adiabatic passage (RAP) (see Chapter 3) is the sweep rate α. In correspondence with the definition in [Zener, 1932; Landau, 1932] we define it as:

$$\frac{\mathrm{d}}{\mathrm{d}t}\omega(t) = \alpha = \frac{\psi_2}{\tau_0^4 + \psi_2^2} \tag{2.1.13}$$

With a transform-limited pulse duration $\Delta t^I_{0,\mathrm{FWHM}} = 130\,\mathrm{fs}$ and a chirp ranging from $0\,\mathrm{ps}^2$ to $1\,\mathrm{ps}^2$ we can reach sweep rates from $1\,\mathrm{ps}^{-2}$ to $80\,\mathrm{ps}^{-2}$. Since the inversion probability of RAP, described

by the Landau-Zener factor, depends on the ratio of sweep rate to Rabi frequency squared, we note here that the maximal sweep rate introduced by our pulse-shaper competes with Rabi frequencies in the terahertz range: $80\,\mathrm{ps}^{-2}$=$80\,\mathrm{THz}^2$ and is at least three orders of magnitude larger than reported for a similar quantum dot RAP experiment [Simon et al., 2011]. RAP is discussed in more detail in Chapter 3.

Equation 2.1.13 can be approximated for our usual pulse parameter where $\tau_0^2 \ll \psi_2$:

$$\alpha \approx \frac{1}{\psi_2}, \tag{2.1.14}$$

and hence the sweep rate is inversely proportional to the chirp.

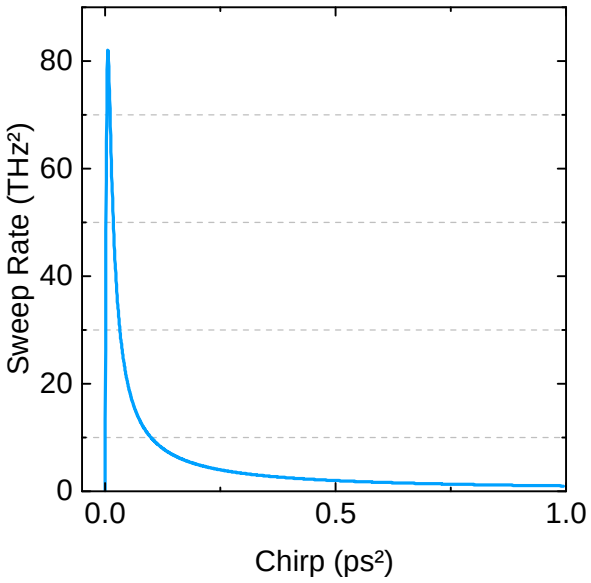

Figure 2.1.4: **Sweep rate as a function of the quadratic phase term, the chirp.** The transform-limited pulse duration is here $\Delta t^I_{\mathrm{FWHM}} = 130\,\mathrm{fs}$.

The SM glass fibres used in the experiments introduce a positive chirp, which is compensated by our pulse-shaper. The amount of chirp introduced by the fibre can be calculated using the dispersion parameter D from the manufacturer, the spectral pulse width and the length of the fibre. For example, one of the SM glass fibres used in the experiments (Thorlabs, 780hp) has $D = 60\,\mathrm{fs\,nm^{-1}\,m^{-1}}$. A spectral width of $\Delta\lambda^I_{\mathrm{FWHM}} = 10\,\mathrm{nm}$ together with the length of 8 m elongates the pulse duration by 4.8 ps. Using equation 2.1.8, the chirp is calculated to be $\psi_2 = 0.225\,\mathrm{ps}^2$. Another way is to perform a measurement as in Fig. 2.1.3(b) but measure the pulse duration after the glass fibre. The minimum in the lens-grating separation shifts by Δs depending on the sign and magnitude of the chirp introduced by the fibre: $\psi_2 = C\ \Delta s$. For the 8 m fibre we measured $\Delta s = 3.991 \pm 0.050\,\mathrm{mm}$, together with the free-space calibration ($C = 0.0927 \pm 0.0698\,\mathrm{ps^2\,mm^{-1}}$) we calculate $\psi_2 = 0.370 \pm 0.280\,\mathrm{ps}^2$.

Useful relations between the electric field, average power and peak power

The envelope of the pulses in intensity can be described by Gaussian function, following Eq. 2.1.2

$$I(t) = I_{\mathrm{peak}} \exp\left(\frac{-t^2}{\tau^2}\right), \tag{2.1.15}$$

where τ is the pulse duration also taking an optional chirp into account, Eq. 2.1.9. A slow detector like a photodiode measures an averaged intensity:

$$I_{\text{average}} = \langle I(t) \rangle = \frac{1}{T} \int_0^T I(t)\,\mathrm{d}t \tag{2.1.16}$$

$$= I_{\text{peak}}\ \frac{1}{T}\ \tau\sqrt{\pi} \tag{2.1.17}$$

$$= I_{\text{peak}}\ f_{\text{rep}}\ \tau\sqrt{\pi} \tag{2.1.18}$$

$$\approx I_{\text{peak}} f_{\text{rep}}\ \Delta t^I_{\text{FWHM}} \tag{2.1.19}$$

Analogously, the averaged power P_{average} is the peak power P_{peak} multiplied by the duty cycle $f_{\text{rep}}\ \tau\sqrt{\pi}$:

$$P_{\text{average}} = P_{\text{peak}}\ f_{\text{rep}}\ \tau\sqrt{\pi} \approx P_{\text{peak}}\ f_{\text{rep}}\ \Delta t^I_{\text{FWHM}}. \tag{2.1.20}$$

We can calculate the electric field amplitude in the focal spot from the measured averaged power and pulse duration:

$$E_{\text{peak,chirped}} = \sqrt{\frac{2P_{\text{average}}}{Ac\epsilon_0 n\sqrt{\pi} f_{\text{rep}}} \frac{\tau_0}{\sqrt{\tau_0^4 + \psi_2^2}}} \tag{2.1.21}$$

$$= \sqrt{\frac{2P_{\text{average}}}{Ac\epsilon_0 n\sqrt{\pi} f_{\text{rep}}} \frac{1}{\tau}}\,, \tag{2.1.22}$$

with A and ϵ_0 being the area of the focal spot and the vacuum permittivity, respectively. The amplitude of the electric field shrinks from originally $E_{\text{peak,unchirped}}$ to $E_{\text{peak,chirped}}$ when stretching the pulse:

$$E_{\text{peak,chirped}} = E_{\text{peak,unchirped}} \sqrt{\pi / (2\tau\tau_0)}. \tag{2.1.23}$$

2.1.3 Pulse Characterisation

The ultra-short pulses created by the femtosecond laser and manipulated in the pulse-shaper units have pulse durations from just below 100 fs up to tens of picoseconds. In order to perform experiments with a precisely controlled magnitude and sign of chirp, we need a reliable way to characterise these pulses. Typical photon detectors, as for example photodiodes, photomultipliers and avalanche-photodiodes, are very slow compared to ultra-short laser pulses. They have rise and fall times in the order of nanoseconds. Nowadays, fast models reach a time resolution of a few tens of picoseconds, but that is still too slow for a characterisation of ultra-short pulses. That is the typical dilemma in ultra-fast optics: in order to measure a fast event in time you need something with an even shorter duration.

As mentioned earlier the spectral and temporal pulse intensity profiles are related by the Heisenberg uncertainty principle, equivalently a Fourier transform. Measuring the intensity spectrum of a pulse with a slow detector also gives information about the temporal evolution. However, no phase information can be resolved in this slow measurement, neither the spectral phase $\psi(\omega)$ nor the temporal phase $\phi(t)$. The (temporal or spectral) phase determines the pulse's frequency versus time, the so called instantaneous frequency: $\omega(t) = \mathrm{d}\phi/\mathrm{d}t = \omega_0 - \alpha t + O\left(t^2\right)$, with α being the sweep rate or chirp rate as defined in Eq. 2.1.13. In the case of a transform-limited pulse, the temporal phase is only determined by $\omega_0 t$ and the instantaneous frequency is constant.

For a full characterisation of unknown pulses, the intensity and the phase have to be measured. The best way to do so is to measure the pulses in a cross-correlation with even shorter pulses. In our case, due to a lack of shorter pulses and the scope of our work, we decided on an easier method. The problem can be simplified since the spectral and temporal shape of the pulses used here is in a good approximation Gaussian. We also know that the main contribution of the pulse-shaper is a quadratic phase resulting in a linear chirp. Under this assumption an auto-correlation measurement

can be used to retrieve the unknown phase coefficient accurately. In addition, a FROG set-up is used to gather additional pulse information about higher order phase terms. A higher phase term contribution changes the symmetry in the spectrogram [Weiner, 2009, p. 122]. Therefore, it can be used without a phase-retrieval algorithm to prove the absence of higher order (> 2) phase terms.

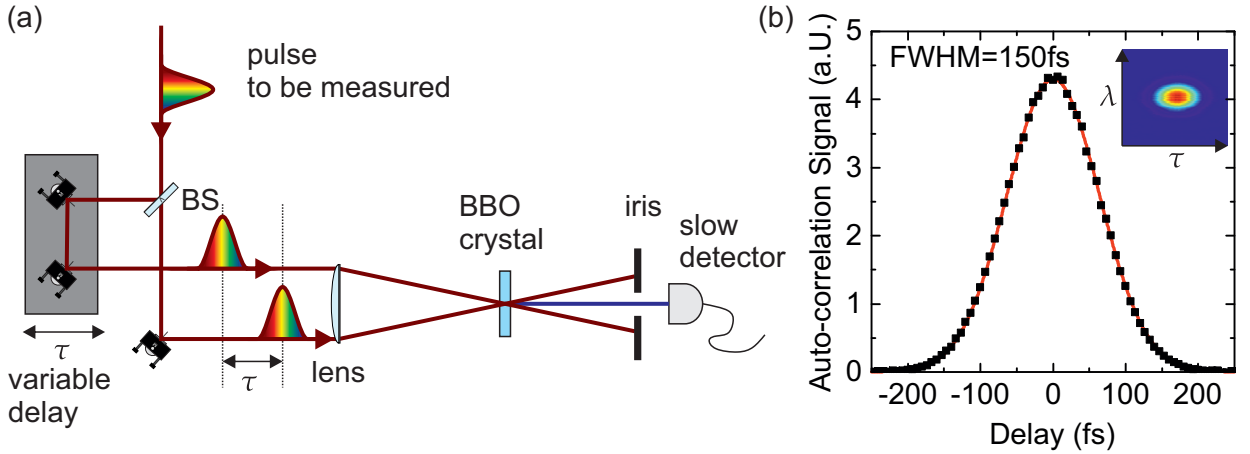

Figure 2.1.5: **Auto-correlator-FROG set-up (a)** Slightly simplified scheme of our home-built auto-correlator-FROG set-up. Beamsplitter (BS), barium borate (BBO) crystal. The slow detector is switchable between a photodiode and a fibre-coupled spectrometer. **(b)** Auto-correlation measurement showing a FWHM of 150 fs. The pulse duration $\Delta t^I_{\mathrm{FWHM}}$ can be calculated to 106.4 fs using eq.2.1.25. The inset shows the corresponding measured FROG trace, a spectrogram.The symmetry shows an absence of phase terms with an order higher than two [Weiner, 2009, p. 122].

Our home-built intensity auto-correlator-FROG set-up is depicted in Fig. 2.1.5(a). It is a typical auto-correlator set-up where the signal is also spectrally resolved, hence the name frequency-resolved-optical-gating (FROG). A beamsplitter splits the pulse train into two arms. The length of one arm is variable and leads to a delay τ, the other length is fixed. Both beams are focused into a non-linear medium (barium borate crystal, BBO). When both focal points overlap in space and time, a two-pulse second harmonic (SH) beam is generated with a wavevector k_{SH} which is the sum of both pulse train wavevectors $k_{1,2}$. An iris in front of the detector blocks the fundamental beams and the single pulse second harmonics with wavevectors $k_{1,2}$. The detector records the two-pulse SH signal as function of the delay τ. The electric field E_{SH} of the SH is proportional to the square of the electric field of the fundamental beam and therefore proportional to the product of the electric fields of the delayed pulse and the pulse from the fixed path length: $E_{SH}(\tau) \propto E(t-\tau)E(\tau)$. The slow detector measures the intensity integrated over the time t. The detector signal S is

$$S(\tau)) \propto \int_{t=-\infty}^{r=\infty} I(t-\tau)I(\tau)\,\mathrm{d}t = AC^2(\tau) \tag{2.1.24}$$

and hence is proportional to the auto-correlation $AC^2(\tau)$. A typical auto-correlation of our pulses is shown in Fig. 2.1.5(b). It has a perfect Gaussian shape with a FWHM of 150 fs. The pulse duration of the Gaussian pulse can be easily calculated with the FWHM of its auto-correlation:

$$\Delta t^I_{\mathrm{FWHM}} = \Delta t_{\mathrm{FWHM,AC}}/\sqrt{2}. \tag{2.1.25}$$

2.2 The Confocal Multi-Purpose Microscope

The microscope built and used in this work is based on a former version of an resonance fluorescence (RF) confocal microscope [Kuhlmann et al., 2013a]. The main difference is the existence of an additional excitation arm allowing to perform experiments with two excitation laser beams with

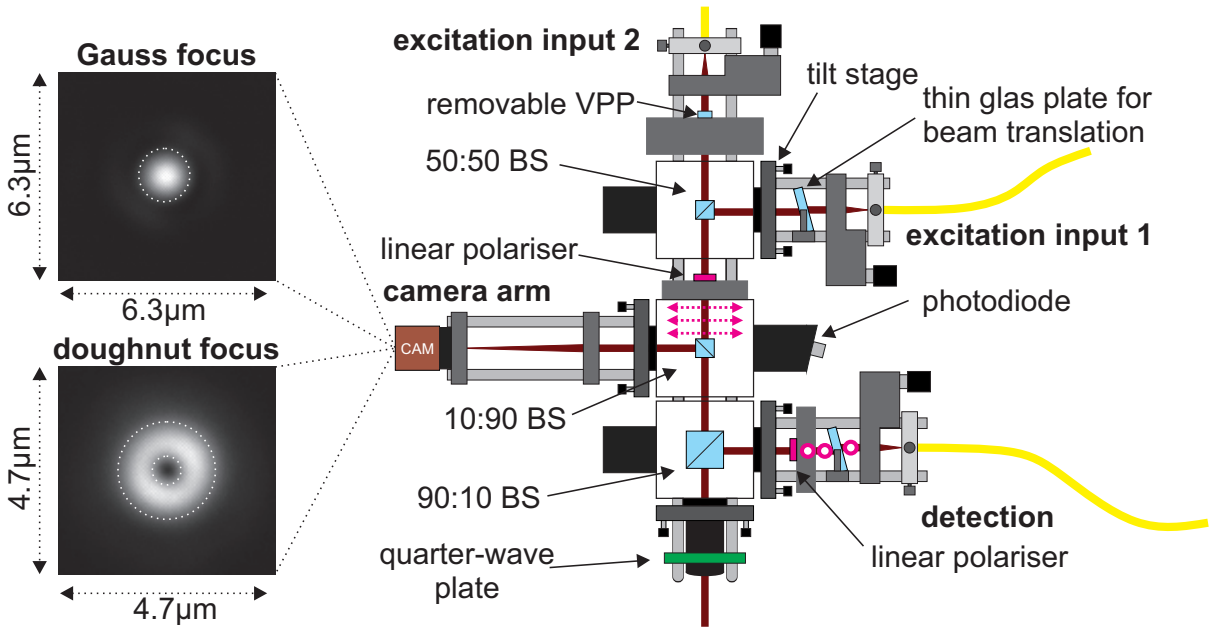

Figure 2.2.1: **Scheme of the confocal broad-band resonance fluorescence microscope.** Two independent excitation arms, a detection arm and a camera arm are combined by beamsplitters (BS) with reflection:transmission ratios as stated. The vortex phase plate (VPP), mounted in an x-y-stage of the vertical excitation arm can be inserted and removed in operando. The camera images depicted on the left were taken with a CMOS camera in reflection from the sample. The upper image was taken without a VPP, the lower one with a VPP in the beam path. The microscope's magnification of 48.4 (f_{obj} = 3.1 mm, f_{lens} = 150 mm) was used to transform the pixel (2.2 µmx2.2 µm) size into a length scale on the sample.

independent phase properties. The microscope consists of two main parts: the skeleton and the microscope head.

The skeleton contains the objective, here an aspheric lens with an NA of 0.68 (Thorlabs, C330TME-B) and the sample on an x-y-z piezo nano positioner (Attocube systems, ANPx101 and ANPz101) and xyz piezo scanner (Attocube systems, ANSxyz100/LT). A thin stainless-steal tube surrounds the skeleton. Once pumped and flushed with helium exchange gas, it is inserted in a liquid helium bath cryostat. Sealing and optical access is achieved with a laser window (Thorlabs, WL11050-C13). All other optics are outside of the cryostat in the microscope head at room-temperature.

The microscope head is sketched in Fig. 2.2.1: it contains two excitation arms and one detection arm, all fibre coupled to the excitation laser system and the detection system, respectively. The fibre coupling is realised with the fibre in an x-y-translation-stage and an aspheric lens (Thorlabs, C280TME-B) in a z-translation-stage. The beams of different arms were overlapped with three non-polarising cube beamsplitters (BS) with the following reflection to transmission split ratios: detection arm 90:10 (Thorlabs, BS028), camera arm 10:90 (Rocky Mountain Instrument Company, customised item) and 50:50 (Thorlabs, BS010) for the excitation arms.

In the vertical excitation arm (excitation input 2), a 2π vortex phase plate (VPP) (RPC Photonics, VPP-1a) adds an azimuthal phase dependency to the excitation laser beam which results in a doughnut shaped focus on the sample as shown in the camera image in Fig. 2.2.1. In our microscope design the VPP is easy to insert and to remove. It is removed for the alignment process of the individual beam paths.

The vertical excitation arm is the reference for all beam paths in the alignment process. After the correct alignment of all BSs is ensured, a tilt stage in the bottom part of the microscope head is used to ensure that the beam strikes the objective in the skeleton in its centre resulting in an aberration-free focal spot on the sample. The tilt stages in the other two arms (excitation input 1

and detection) are then used to overlay these two beam paths with the reference. The tilt stages give only the freedom of tilting the beam, while a parallel displacement of the beam can not be compensated. Parallel beam displacements up to a few hundred micrometers can be introduced during the construction of the microscope depending on the precision of the mechanics and the BS glueing process. In this microscope design, we can not translate the BSs along one of the two beam directions (x or y). In our single excitation arm confocal microscopes [Kuhlmann et al., 2013a], we relied on the precision of the mount and the glueing process. Even so, we achieved a high collection efficiency and almost aberration-free focal spots.

In the multi-purpose microscope presented here, there are two excitation arms and hence three beam paths to overlap. A common optical axis is crucial for the the laser suppression and for the two-pulse experiments. Therefore, another degree of freedom was necessary in order to compensate small parallel translations of the beams. Therefore, we inserted in the Gaussian excitation arm and in the detection arm a laser window, the 'translation window'. It is a 5 mm thick piece of high quality, flat, anti-reflection coated BK-7 glass (Thorlabs, WL11050-C13) in a gimbal rotation mount. It enables a precise parallel translation of the beam up to ±1 mm in x and y direction while keeping the reflection losses low. With this additional degree of freedom we can ensure that the beams strike the BS at right angles (tilt stage) and at the same position (translation windows). An optimal overlapping of all three beam paths was achieved in the experiments: we reached simultaneously a collection efficiency (measured in reflection on GaAs with a CW laser) of more than 59% with both excitation arms and laser suppression up to eight orders of magnitude, see table 2.2.1.

Besides the excitation and detection arms, the microscope features a camera arm containing an industrial CMOS camera (Allied Vision, Guppy Pro F-503) with a pixel size of 2.2 µm x 2.2 µm. It allows a live feedback and quality control of the focal spots during the alignment and helps in navigating on the sample. The camera image's magnification of an object in the focus on the sample is given by the ratio of the focal lengths of the objective and the lens in front of the camera:

$$m = \frac{x_1}{x_0} = \frac{f_{lens}}{f_{obj}} = \frac{3.1\,\text{mm}}{150\,\text{mm}} = 48.4 \tag{2.2.1}$$

For CW RF measurements and pulsed RF measurements (chapter 4 and 5) as well as for the imaging-two-pulse experiment (6), the laser suppression is an essential feature of the microscope. We use a dark-field technique based on orthogonally polarised excitation and detection. Two thin-film polarisers (Thorlabs, LPVIS050-MP), one after the excitation BS and one before the detection fibre, define a pair of orthogonal linear polarisations. The extinction factor for the reflected laser light depends strongly on the quality of the focal spot. On a bare piece of a GaAs wafer we reached extinction ratios of 10^8:1, while under a ZrO_2 SIL on GaAs in CW excitation we reached 10^7:1. With broad-band excitation pulses ($\Delta\lambda^I_{\text{FWHM}} \approx 10\,\text{nm}$) and a ZrO_2 SIL the ratio decreases to 10^5:1. A slow mechanical drift can diminish the extinction ratio slightly (maximum an order of magnitude) within the next 30 min after optimizing the microscope for the highest ratio. Afterwards, it remains stable: long-time measurements proved the stability of the complex microscope over several days.

Some experiments presented in this thesis were performed with circularly polarised excitation, for example, the imaging experiment. For this purpose, a quarter-wave plate just before the laser window is oriented at an angle of 45° with respect to the axis of the linear polarisation and hence, transforms the linear polarisation into circular polarisation. The pair of orthogonal excitation and detection polarisations are then σ^+ and σ^-, left and right circular respectively, or vice versa.

Excitation Input 1	
Confocal detection efficiency	59%
Back-reflected laser extinction ratio	$2.4 \times 10^8 : 1$
Calculated excitation efficiency	3.6%
Excitation Input 2	
Confocal detection efficiency	65%
Back-reflected laser extinction ratio	$3.2 \times 10^8 : 1$
Calculated excitation efficiency	3.6%
Detection Arm	
Calculated detection percentage (BS, lin.pol.)	$90\% * 81\% = 73\%$
Laser suppression optimized for both excitation beams	
Back-reflected laser extinction ratio, individual arms	$6 \times 10^6 : 1, 1.9 \times 10^6 : 1$
Back-reflected laser extinction ratio, both arms together	$4.2 \times 10^6 : 1$

Table 2.2.1: **Performance of the multi-purpose microscope** measured in reflection of a narrow CW laser on a piece of a GaAs wafer. For the confocal detection efficiencies the following transmission and reflection coefficients were taken into account : GaAs reflection 32%, polariser transmission 81%, 98% laser windows, 99.50% C280TME-B lens.

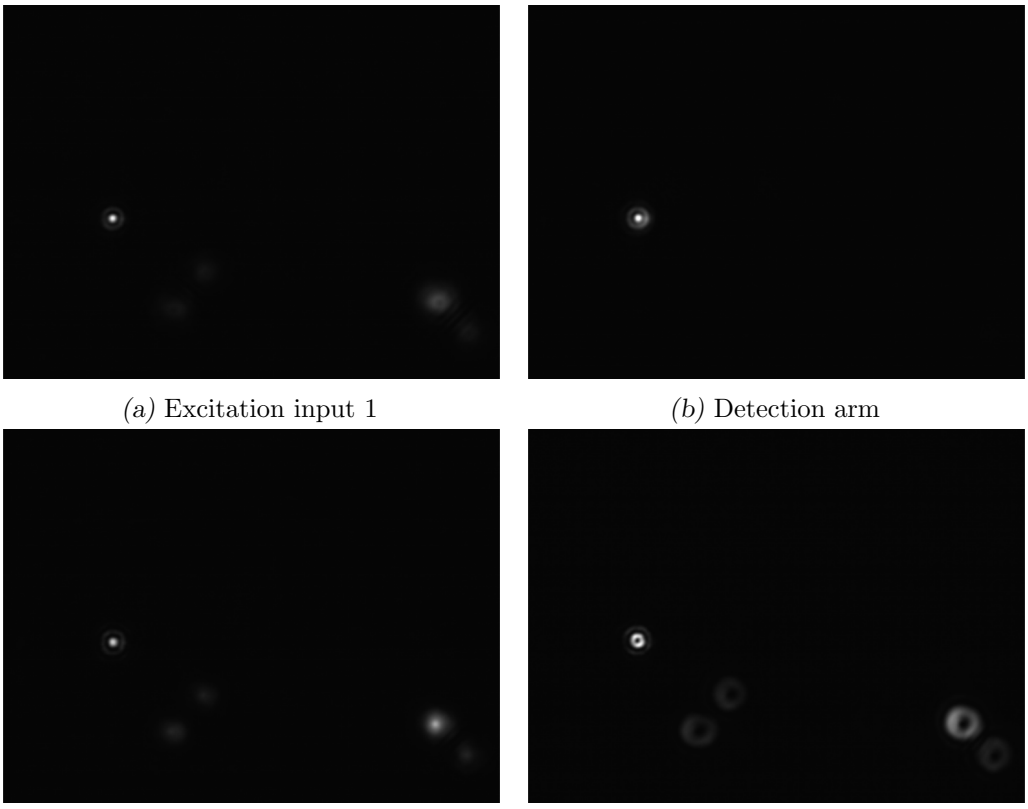

(a) Excitation input 1 *(b)* Detection arm

(c) Excitation input 2 without VPP *(d)* Excitation input 2 with VPP

Figure 2.2.2: **Images of the focal spots on the sample taken with the CMOS camera.** A CW laser is sent through the optical fibre of the microscope arm stated in the sub-caption. The focus on the sample is the tiny point in the left part of the images. In (a), (c) and (d) four ghost beam focal points from the first two cube-beamsplitters appear on the right side. The images have a size of 768×578 pixel^2 corresponding to an area on the sample of $35 \times 27\,\mu m^2$.

2.2.1 Solid Immersion Lens Microscopy

In our experiments we use hemispherical solid immersion lenses (SILs) on the one hand to decrease the focal spot size of our laser on the sample and on the other hand to increase the photon collection efficiency in our experiments [Serrels et al., 2008]. Both benefits are especially important for the imaging experiment in Chapter 6. A SIL is positioned on top of the quantum dot sample and fixed in position either by only Van der Waals forces (vaporising H_20 between SIL and sample) or using a thin film of vacuum grease.

The first benefit mentioned is the reduced diffraction limit using hemispherical SILs:

$$\Delta x = \frac{0.52\lambda}{n_{\mathrm{SIL}}\mathrm{NA}_{\mathrm{Obj}}}, \tag{2.2.2}$$

with n_{SIL} and $\mathrm{NA}_{\mathrm{Obj}}$ being the refractive index of the SIL and the numerical aperture of the objective, respectively.

The second benefit is the gain in collection efficiency by a SIL. In order to estimate the gain, we can consider the emission in the light cone collected by the microscope to be isotropic, even though the quantum dot's emission is a dipole field. This approximation is valid since the dipole lies in the (x, y) plane (see Fig. 1.2.1 and Fig. 1.1.1(a)) and the change of the intensity close to the maximum of the dipole radiation is rather flat. Therefore, the gain can be approximated by the ratio of the solid angle of the collection cone of the objective in the sample material without SIL to the cone in the material with SIL:

$$g = \frac{2\pi(1-\cos(\alpha_2))}{2\pi(1-\cos(\alpha_1))}, \text{ with} \tag{2.2.3}$$

$$\alpha_1 = \arcsin(\mathrm{NA}/n_{\mathrm{sample}}), \tag{2.2.4}$$

$$\alpha_2 = \arcsin(\mathrm{NA}\,\mathrm{n}_{\mathrm{SIL}}/n_{\mathrm{sample}}). \tag{2.2.5}$$

Also important to note is the optical lever effect. When a laser is focused through a hemispherical SIL the optical lever effect reduces the actual movement of the focus on the sample by a factor $1/n_{\mathrm{SIL}}$ to $\tilde{d} = d/n$ when moving the sample by the distance d [Serrels et al., 2008].

We used in our experiment two types of SILs: GaP SILs and ZrO_2 SILs. The ideal SIL would match the refractive index of our sample. The host material of our quantum dots is GaAs and has a refractive index of $n_{\mathrm{GaAs}}(950\,\mathrm{nm}) = 3.543$ at a wavelength of 950 nm and room temperature ($T = 295\,\mathrm{K}$, $dn/dT = \sim 3.2 \times 10^{-4}\,\mathrm{K}^{-1}$ [Skauli et al., 2003]).

The first type, a zirconium dioxide (ZrO_2) SIL is rather robust against imperfections in the height to radius ratio as well as to a gap between sample surface and the bottom of the SIL. Therefore it is straightforward to use and quite reliable. The refractive index at 950 nm and room-temperature is $n_{\mathrm{ZrO_2}}(950\,\mathrm{nm}) = 2.17$.

The expected gain in collection efficiency is

$$g(NA = 0.68, n_{\mathrm{SIL}} = 2.17, n_{\mathrm{sample}} = 3.543) = 4.88. \tag{2.2.6}$$

A GaP SIL has a higher refractive index than ZrO_2; it is close to GaAs: $n_{\mathrm{GaP}}(950\,\mathrm{nm}) = 3.129$. A GaP SIL promises a higher collection efficiency:

$$g(NA = 0.68, n_{\mathrm{SIL}} = 3.129, n_{\mathrm{sample}} = 3.543) = 10.77, \tag{2.2.7}$$

although it is harder experimentally to reach the resolution and collection efficiency expected from the theory since the GaP SIL is much more sensitive to imperfections than a ZrO_2 SIL. The gap between the bottom of the SIL and the sample must be way below 200 nm when working with a wavelength of 950 nm. The sweet spot, that is the area under the SIL without significant aberrations in the imaging, is reduced to a few tens of micrometer squared. Nevertheless we were

able to reach with the GaP SIL the diffraction limit of 220 nm with a wavelength of 950 nm and an NA of 0.68.

We performed measurements to verify the performance of the SILs at room-temperature and at low-temperature. A chrome-chequerboard and a chrome line-grating were used as test samples.

The sample was mounted on an *xyz* piezo nano positioner (Attocube systems, ANPx101 and ANPz101) and *xyz* piezo scanner (Attocube systems, ANSxyz100/LT). Using the large travel range (5 mm) of the positioners the sweet spot of the SIL is moved into the focus with nanometer precision. Imaging scans were then performed using the piezo scanner. The scanning range is 30 µm*30 µm*15 µm at liquid helium temperature. The scanner's position can be controlled by applying a voltage from 0 V up to 150 V. We use a low-noise DAC source providing voltage up to 10 V, then amplified by a factor of 10.

We performed measurements at liquid helium temperature and at room-temperature, without SIL, with a ZrO_2 SIL and with different GaP SILs. Here, we show only a short extract of all measurements; we show the measurements performed under the same conditions as in the imaging experiment (Chapter 6), once with a ZrO_2 SIL on top of the sample and once without, see Fig. 2.2.3 and 2.2.4, respectively.

In order to validate the linearity of the scanner and calibrate the transformation from voltage into a position we measured the reflectivity of a chrome line-grating with a periodicity of 1 µm as a function of the voltage amplified and applied to the scanner. In both cases we could prove a good linearity of the scanner. The optical lever effect that appears when imaging under a hemispherical SIL is a verification of the quality of the imaging: the ratio of the calibration with and without SIL, 2.10 ± 0.04, is almost identical to the refractive index of the ZrO_2 SIL ($n_{\mathrm{SIL}}(\lambda = 937\,\mathrm{nm}) = 2.13$).

We can extract from these measurements the actual focal spot size and can compare it to the diffraction limit. A Gaussian fit to the data (derivative of the reflectivity) reveals for the ZrO_2 SIL with 388 ± 3 nm a FWHM slightly worse than the diffraction limit:

$$\Delta x = \frac{0.52\lambda}{n_{\mathrm{SIL}}\mathrm{NA}_{\mathrm{Obj}}} = \frac{0.52 \times 937\,\mathrm{nm}}{2.13 \times 0.68} \approx 336\,\mathrm{nm}, \tag{2.2.8}$$

and without a SIL the FWHM with 668 ± 36 nm corresponds to the diffraction limit within the measurement error:

$$\Delta x = \frac{0.52\lambda}{\mathrm{NA}_{\mathrm{Obj}}} = \frac{0.52 \times 937\,\mathrm{nm}}{0.68} \approx 717\,\mathrm{nm}. \tag{2.2.9}$$

These measurements were performed with broad-band laser pulses (FWHM 10 nm) which are less effectively focused by the aspheric lens used here. Still, our microscope reaches close to diffraction limited performance.

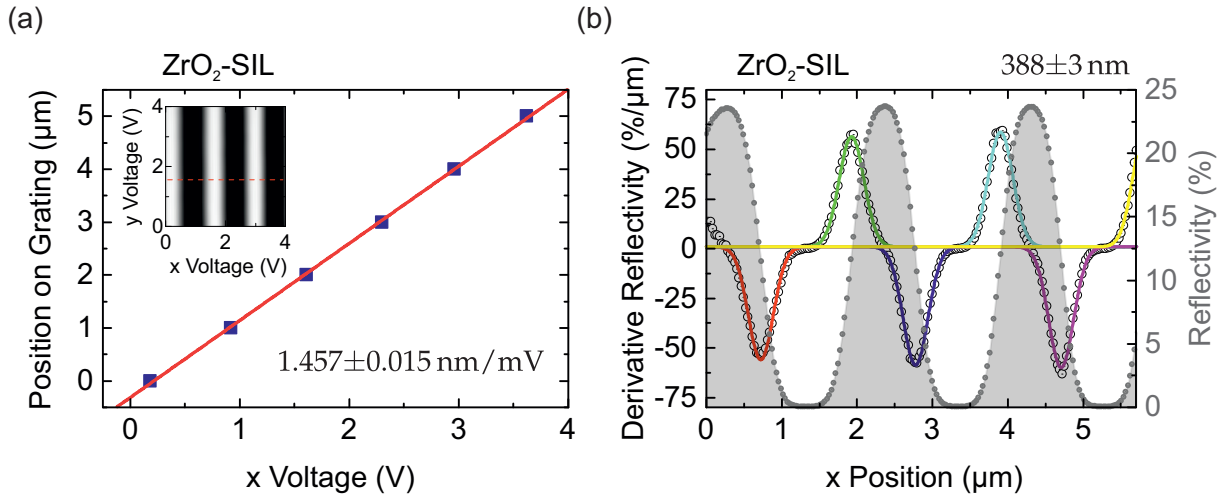

Figure 2.2.3: **Calibration of the low-temperature scanner with a ZrO_2 SIL.** Reflectivity measurement on a chrome line grating (1 µm periodicity) with broad-band pulsed laser. **(a)** Extracted position of maxima and minima on the grating as function of the applied voltage. A linear fit to the data shows a good linearity in the studied voltage range with a conversion factor of 1.457 ± 0.015 nm/mV. **(b)** Reflectivity signal (grey dots with filled area, right axis) and its derivative (black hollow circles, left axis) as a function of the converted scanner position. The derivative is fitted with Gaussian functions. The common FWHM of 388 nm demonstrates that the microscope operates close to the diffraction limit even when the using spectrally 10 nm broad pulses.

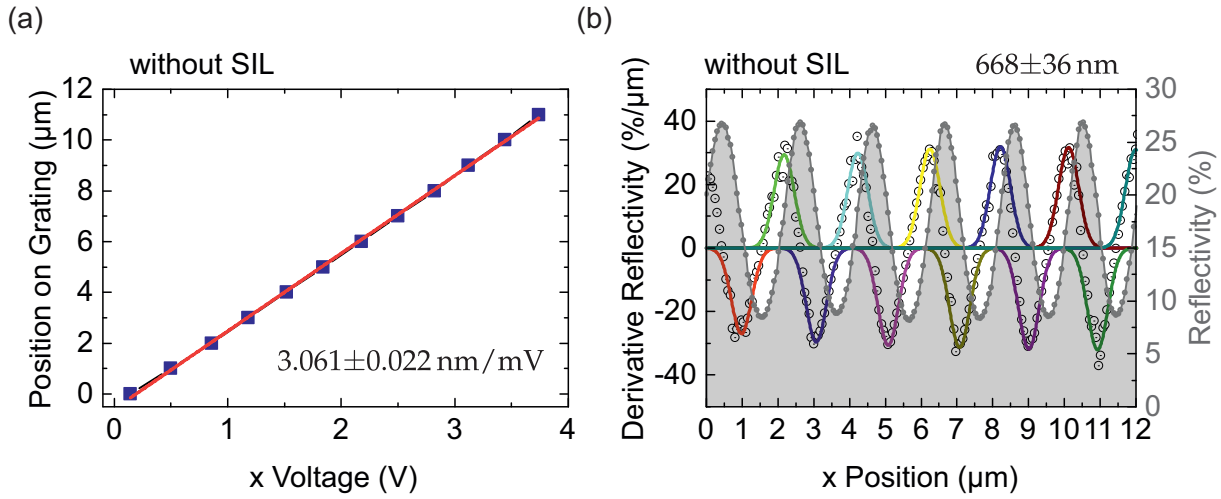

Figure 2.2.4: **Calibration of the low-temperature scanner without SIL.** Analogue to Fig. 2.2.3 with a common FWHM of 668 nm.

2.3 Photon Detection and Analysis

In our experimental set-up we use mainly two instruments for the detection of the fluorescence from quantum dots. The first one is a spectrometer with a CCD camera cooled with liquid nitrogen (Princeton Instruments, Acton SP2500). It features a grating turret with 1500 lines/mm, 1200 lines/mm and 300 lines/mm. The resolution on the CCD goes down to 0.1 nm. The other one is a single-photon-avalanche-photodiode (SPAD) (PicoQuant, Tau-Spad 20). The SPAD has an efficiency of 20 % at 950 nm, which is our region of interest for QD experiments. The dark-count rate is quite low on this SPAD model: below 20 cts/s. The dead time is around 70 ns. The photon timing resolution is 400 ps. We use the SPAD in combination with a home-built high-efficiency monochromator with a bandwidth of ∼0.5 nm.

2.4 Appendix: Detailed Scheme of the Femto Laser Set-up

A true to scale scheme of the set-up for the manipulation and characterisation of the ultra-short pulses is shown in Fig. 2.4.1.

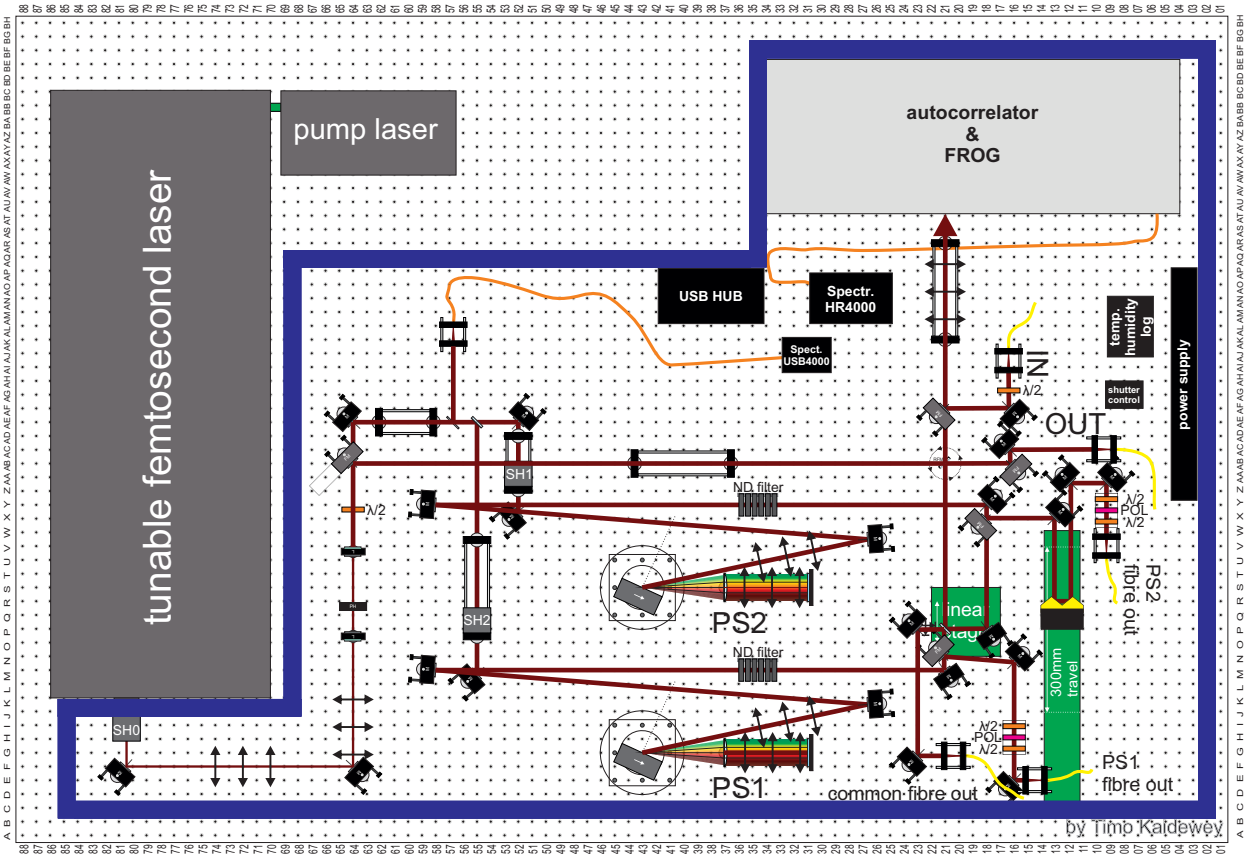

Figure 2.4.1: **Detailed scheme of the femtosecond laser set-up.** PS: pulse-shaper, SH: mechanical shutter, POL: linear polariser, FROG: frequency-resolved-optical-gating, M: mirror, L: lens, PH: pinhole, FM: flipping mirror, $\lambda/2$: half-wave plate.

3 Rapid Adiabatic Passage on a Two-Level System

In this chapter we review the basics of the theory of rapid adiabatic passage (RAP) for a robust occupation inversion of a two-level system. RAP overcomes the known disadvantage of conventional π-pulse excitation: a strong dependence on fluctuating experimental parameters. RAP is particularly attractive in solid-state quasi-two-level systems since fluctuations here are inherent to the system.

After the discussion of single pulse RAP we go over to a two pulse RAP sequence. In particular, we expand RAP to a new tool for a coherent, super resolution imaging of two-level systems in the far-field. Thereby, we introduce a sequence of two RAP pulses and develop a model to simulate the effect on a two-level system and show how we can overcome with this technique the diffraction limit of conventional microscopy. The corresponding experimental realisation and confirmation of our model is presented in Chapter 6.

3.1 Introduction

In optical two-level systems, complete occupation of the excited level can theoretically be reached with a pulse area of π. Thereby, the pulse area depends on parameters such as pulse duration and laser power. Also detuning from the resonant transition energy plays an important role as it reduces the transition probability. The better these parameters can be controlled, the higher is the fidelity of population inversion. However, in most experiments all these parameters fluctuate in a significant way. In the case of self-assembled quantum dots embedded in diodes, the transition energy can be fine tuned by the electric field in the diode due to the quantum confined Stark effect and hence, the detuning depends on the stability of the electric field experienced by the quantum dot. Fluctuations of an external applied field as well as charge fluctuations [Houel et al., 2012] reduce the fidelity of optical transitions.

3.2 Rabi Oscillations

Before discussing an alternative approach for robust inversion, it is helpful to recapitulate the basic description of two-level systems. Here, we consider a semi-classical theory where the electromagnetic field is treated classically and the light-matter interaction quantum-mechanically. Beginning with the Schrödinger equation, considering the interaction as a dipole interaction, separating the time evolution of the unperturbed system, and making the rotating wave approximation [Allen et al., 1988] leads to the following Hamiltonian:

$$H_{\mathrm{RWA}} = \hbar \begin{pmatrix} 0 & -\Omega^*/2 \\ -\Omega/2 & \Delta \end{pmatrix},$$

where the resonant Rabi frequency Ω and the detuning Δ are defined as:

$$\Omega = \vec{\mu}_{21}\ \hat{\epsilon}\ E_0/\hbar, \tag{3.2.1}$$

$$\Delta = (E_2 - E_1)/\hbar - \omega = \omega_{21} - \omega, \tag{3.2.2}$$

where $\vec{\mu}_{21}$ is the dipole matrix element, E_0 the electric field amplitude, $\hat{\epsilon}$ the polarization and the eigenenergies E_1 and E_2 correspond to the bare eigenstates $|1\rangle$ and $|2\rangle$ of the unperturbed system,

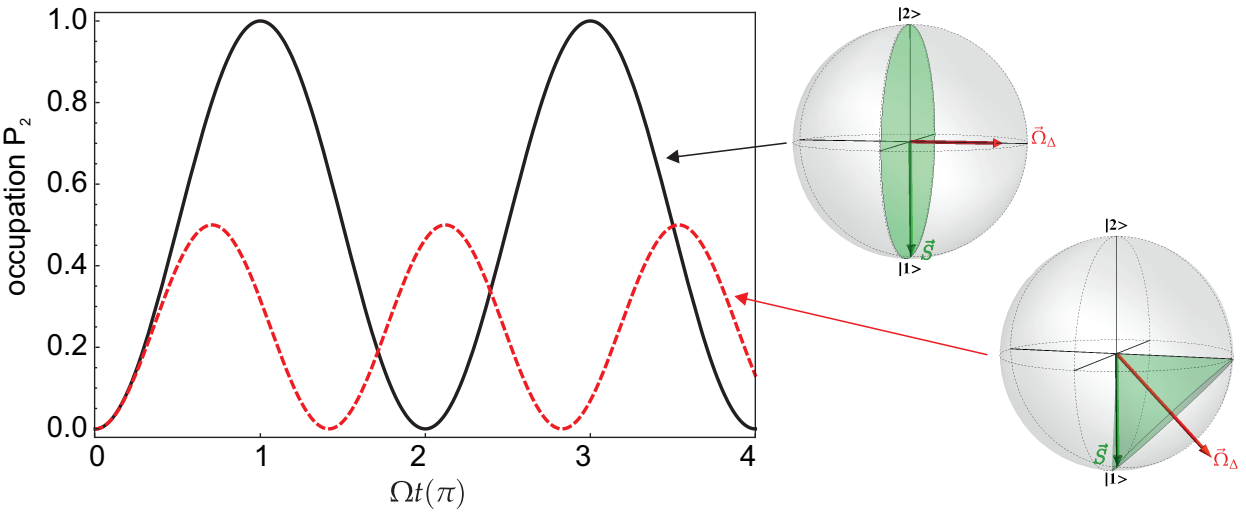

Figure 3.2.1: Rabi oscillations for resonant ($\Delta = 0$, solid line) and detuned ($\Delta = \Omega/2$, red dashed line) optical excitation. In the resonant case full occupation of level 2 can be reached by a pulse area of π. Detuning reduces the occupation and alters the effective frequency. On the right side the two cases are sketched on the Bloch sphere with the Bloch vector $\vec{S}$ precessing around the torque vector $\vec{\Omega}_\Delta$.

respectively.
Assuming a small, constant detuning (near resonant case) and an initial occupation of level 1 at $t = 0$ leads to the solution $|\varphi\rangle = c_1 |1\rangle + c_2 |2\rangle$ of the Schrödinger equation that describes an oscillation of the occupation in time:

$$P_2 = |c_2(t)|^2 = \frac{1}{2}\left(\frac{\Omega}{\Omega_\Delta}\right)^2 \left[1 - \cos\left(\Omega_\Delta t\right)\right]. \tag{3.2.3}$$

Thereby, we introduced the precession frequency $\Omega_\Delta = \sqrt{\Omega^2 + \Delta^2}$. Figure 3.2.1 shows the probability to find the system in state 2 versus time or equivalently versus the pulse area [Allen et al., 1988]. In an excitation with a long rectangular pulse the pulse area is the product of interaction time t and the constant Rabi frequency Ω_Δ. The sinusoidal occupation oscillations between level 1 and 2 are called Rabi oscillations. The figure demonstrates a significant deviation from 100 % occupation of level 2 for detuning from resonance and for a pulse area unequal to odd multiples of π.

3.3 Rapid Adiabatic Passage

Rapid adiabatic passage (RAP) overcomes the problem of fluctuating parameters at the expense of a more complex experimental realisation. In RAP, the detuning between the electromagnetic field and the resonance is swept from a large negative amount through zero detuning (resonance) to a large positive amount. In fact, a maximal absolute detuning of several inhomogeneous linewidths of the resonance is enough [Allen et al., 1988]. Sweeping the detuning results in a rotation of the torque vector $\vec{\Omega}_\Delta = (-\Omega, 0, \Delta)$ in the Bloch sphere from the initial state $|1\rangle$ to the final state $|2\rangle$ as sketched in Figure 3.3.1. When sweeping adiabatically, the faster precession of the Bloch vector $\vec{S}$ can follow the torque vector and hence, the two-level system is inverted [Allen et al., 1988].

The light-matter Hamiltonian in section 3.2 leads to the dressed eigenenergies of the two-level system:

$$E_\pm(t) = \frac{\hbar}{2}\left(\Delta(t) \pm \sqrt{\Delta(t)^2 + |\Omega(t)|^2}\right). \tag{3.3.1}$$

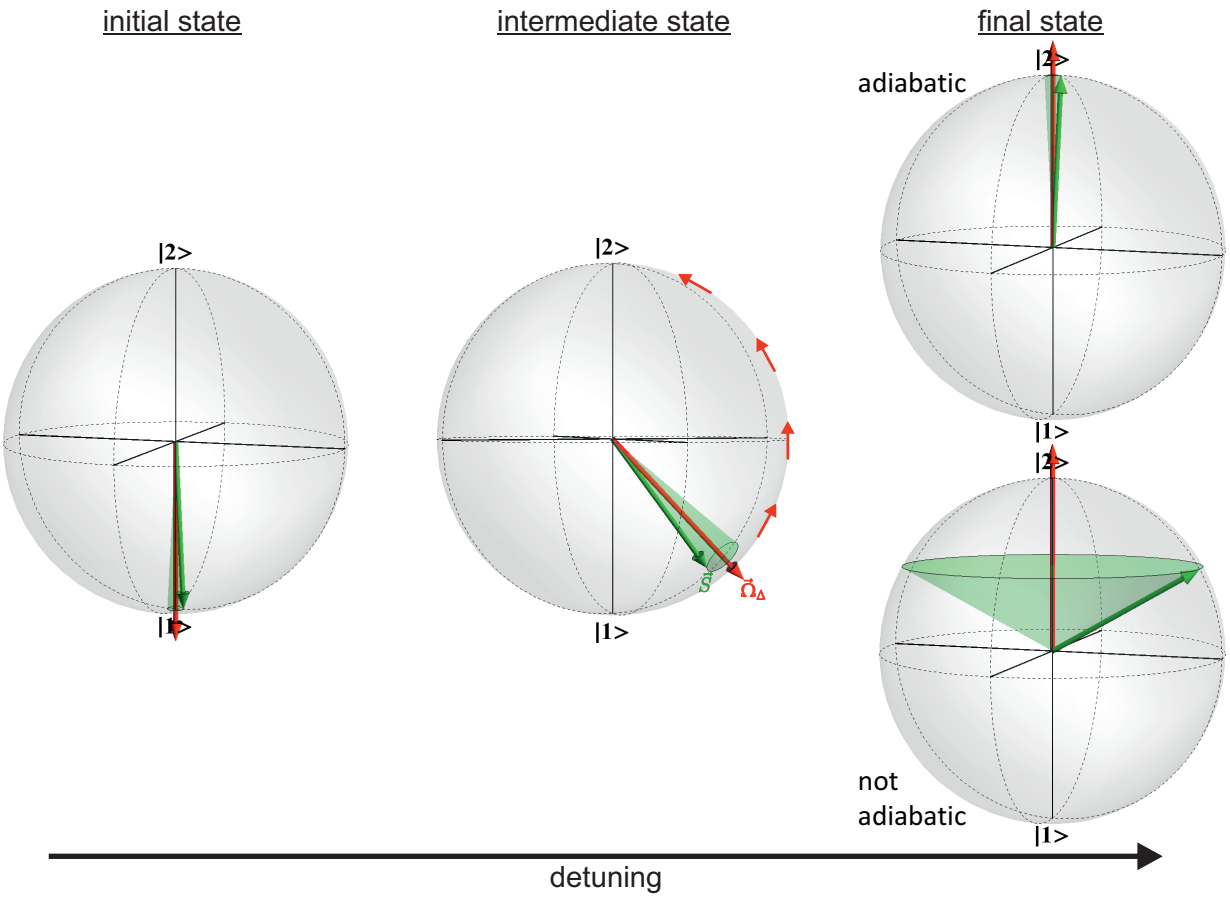

Figure 3.3.1: Rapid adiabatic passage concept on the Bloch sphere.

Figure 3.3.2 shows the dressed (solid lines) and bare (dashed lines) eigenenergies as a function of the detuning. The bare states are linear functions of the detuning; the dressed eigenenergies on the other hand are hyperbolae with an avoided crossing at zero detuning. The closest separation between E_+ and E_- is given by the Rabi frequency and often referred to as Rabi splitting.

For large absolute detuning $|\Delta|$ the dressed and bare states converge. If Δ is tuned over the resonance slowly enough that the system does not change eigenstates during the evolution, the system is inverted from the initial state $|1\rangle$ to the final state $|2\rangle$. This could also been seen by considering the dressed eigenstates [Melinger et al., 1994]

$$|-\rangle(t) = \cos(\theta(t)/2)\,|1\rangle - \sin(\theta(t)/2)\,|2\rangle\,, \tag{3.3.2}$$

$$|+\rangle(t) = \sin(\theta(t)/2)\,|1\rangle + \cos(\theta(t)/2)\,|2\rangle \tag{3.3.3}$$

with $\tan(\theta(t)) = |\Omega|/\Delta(t)$. The description with dressed eigenstates is quite illustrative on the Bloch sphere: θ is the angle between the torque vector Ω and the equatorial plane. While adiabatically moving from one limit $|+\rangle(t) \overset{\Delta\to-\infty}{\longrightarrow} |1\rangle$ to the other $|+\rangle(t) \overset{\Delta\to\infty}{\longrightarrow} |2\rangle$, the expectation value evolves from pure occupation of level 1 to pure occupation of level 2. A condition to ensure an adiabatic process is defined. In the picture of the Bloch sphere, it is easy to imagine that the precession frequency $|\vec{\Omega}_\Delta|$ of the Bloch vector around the torque vector $\vec{\Omega}_\Delta$ has to be much faster than the rotation of the torque vector $|\mathrm{d}\theta(t)/\mathrm{d}t|$ in order to ensure that the Bloch vector follows the torque vector and hence [Allen et al., 1988; Malinovsky and Krause, 2001; Zhdanovich et al., 2008; Wu et al., 2011]:

$$|\vec{\Omega}| = \sqrt{\Delta(t)^2 + |\Omega(t)|^2} \gg \left|\frac{\mathrm{d}}{\mathrm{d}t}\theta(t)\right|. \tag{3.3.4}$$

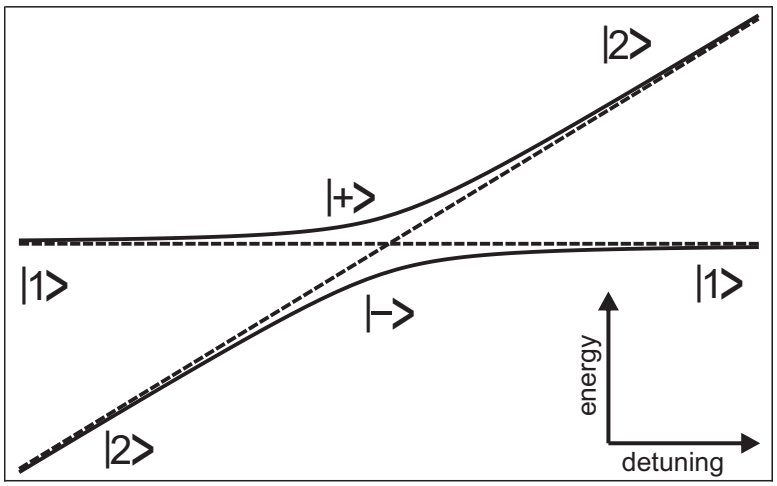

Figure 3.3.2: Eigenenergies E_1, E_2 and E_-, E_+ of the unperturbed (dashed) and perturbed (solid) Hamiltonian as function of detuning Δ.

A more quantitative description of the condition for an adiabatic transfer was given independently by Landau [Landau, 1932] and Zener [Zener, 1932] a long time ago. They derived in the dressed state picture of a driven two-level system the probability for the system to make a transition from one branch in Figure 3.3.2 to the other branch. Today, this probability is commonly known as the Landau-Zener factor p_{LZ}:

$$p_{\mathrm{LZ}}(\Omega, \alpha) = \exp\left(-\frac{\pi\Omega^2}{2\alpha}\right) \tag{3.3.5}$$

$$\Omega = E_0 \, \frac{\vec{\mu}_{21}\hat{\epsilon}}{\hbar}, \tag{3.3.6}$$

where Ω is the angular Rabi frequency and α the sweep rate. They assumed the difference of the bare states to be a linear function in time and the splitting of the asymptotes, here the Rabi frequency, to be constant in time. The outcome is similar to the condition illustrative geometrical consideration on the Bloch sphere: the Rabi frequency must be much faster than the sweep rate (more precisely $\Omega^2 \gg \alpha$) for a high inversion probability of the system.

3.4 Sweeping the Detuning - Chirped Pulses

There are several methods to alter the detuning with time. They can be sorted in two general classes: either the resonance frequency ω_0 of the two-level system or the frequency of the electromagnetic field ω is a function of time.

RAP in the optical regime was first demonstrated by Loy by varying the resonance frequency ω_0 in a NH_3 vapour [Loy, 1974]. In semiconductors it is also possible to tune ω_0, for example by means of the quantum confined Stark effect.

We focus in this thesis on the second class: the laser frequency ω is tuned. Pulsed excitation is here necessary since a tuning of the laser cavity would be too slow compared to the life time and coherence time of semiconductor quantum dots. Short pulses are needed to provide the spectral bandwidth for the detuning range. A chirp in the pulses provides the sweeping of the detuning. In a chirped pulse, the instantaneous frequency changes in time over the duration of the pulse. Or in other words, different spectral components appear at different times. An originally transform-limited pulse gathers a chirp while propagating through dispersive media.

RAP using chirped pulses was demonstrated on among others on Na vapour by Melinger [Melinger et al., 1994] and on quantum dots [Simon et al., 2011; Wu et al., 2011] using a grating pair and a long optical fibre (both dispersive elements). In the framework of this thesis, a pulse shaper was

built in order to control precisely the magnitude and sign of the chirp introduced. More details about pulse shaping are given in Section 2.1.2 of Chapter 2.

3.5 Rabi Rotations and RAP with Gaussian Pulses

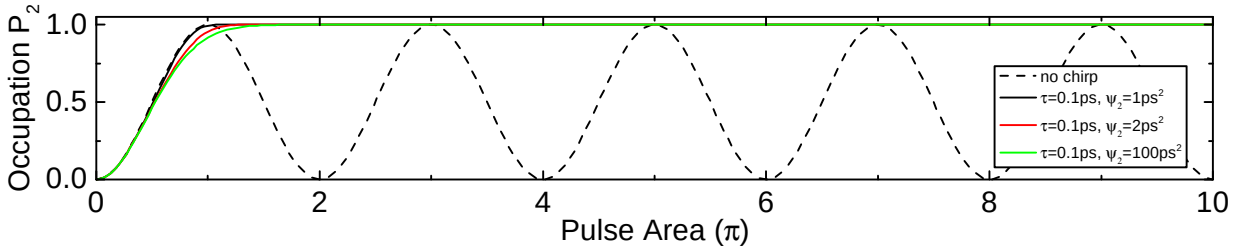

Figure 3.5.1: Occupation of the second level as function of the pulse area for four different magnitudes of chirp as stated in the legend.

In this section we compare ideal Rabi rotations to the RAP response. Thereby, we expand the model from a long rectangular pulse where the Rabi frequency is constant in time (as assumed by Landau and Zener) to a case where we use Gaussian pulses with Gaussian evolution of the Rabi frequency. For this purpose, we replace the product of the constant Rabi frequency and a time with the pulse area, the temporally integrated Rabi frequency. We then express the pulse area as function of parameters accessible in the experiment such as the averaged excitation power P_{avg}, the chirp rate α, the transform-limited pulse duration τ_0 and the area of the focal spot A. The projection of the dipole coupling $\vec{\mu}_{21}\hat{\epsilon}$ can then be extracted from the experiment by fitting the data.

The occupation of the second level, P_2, with chirp ($P_{2,\mathrm{LZ}}$, Landau-Zener) and without chirp ($P_{2,\mathrm{Rabi}}$, Rabi) is given by the following relations:

$$P_{2,\mathrm{LZ}}(\Omega(\psi_2),\alpha) = 1-\exp\left(-\frac{2\pi\Omega(\psi_2)^2}{4\alpha}\right) \qquad P_{2,\mathrm{Rabi}}(\Omega) = \frac{1}{2}\left[1-\cos\left(\Omega t\right)\right] \tag{3.5.1}$$

$$P_{2,\mathrm{LZ}}(\Theta_{\mathrm{LZ}}) = 1-\exp\left(-\Theta_{\mathrm{LZ}}^2/4\right) \qquad P_{2,\mathrm{Rabi}}(\Theta_R) = \frac{1}{2}\left[1-\cos\left(\Theta_R\right)\right] \tag{3.5.2}$$

Here we defined the pulse area Θ as the integral in time over the Rabi frequency $\Omega(t)$ of the pulse which leads for a Gaussian pulse with amplitude Ω_{peak} to:

$$\Theta_{\mathrm{LZ}} = \frac{\sqrt{2\pi}\,\Omega_{\mathrm{peak}}(\psi_2)}{\sqrt{\alpha}} \qquad \Theta_{\mathrm{R}} = \Omega_{\mathrm{peak}}\tau_0\sqrt{2\pi} \tag{3.5.3}$$

$$\Theta_{\mathrm{LZ}} = \sqrt{2\pi}\,\frac{\vec{\mu}_{21}\hat{\epsilon}}{\hbar}\sqrt{\frac{2P_{\mathrm{avg}}\tau_0}{A\sqrt{\pi}f_{\mathrm{rep}}c\epsilon_0 n}\frac{\sqrt{\tau_0^4+\psi_2^2}}{\psi_2}} \qquad \Theta_{\mathrm{R}} = \sqrt{2\pi}\,\frac{\vec{\mu}_{21}\hat{\epsilon}}{\hbar}\sqrt{\frac{2P_{\mathrm{avg}}\tau_0}{A\sqrt{\pi}f_{\mathrm{rep}}c\epsilon_0 n}} \tag{3.5.4}$$

$$\Theta_{\mathrm{LZ}} = \Theta_{\mathrm{R}}\sqrt{\frac{\sqrt{\tau_0^4+\psi_2^2}}{\psi_2}} \approx \Theta_{\mathrm{R}} \qquad \Theta_{\mathrm{R}} = \sqrt{2\pi}\,\frac{\vec{\mu}_{21}\hat{\epsilon}}{\hbar}E_{\mathrm{peak}}\tau_0 \tag{3.5.5}$$

The pulse area is proportional to the square root of the transform-limited pulse width as well as to the square root of the measured averaged excitation power. In our pulse parameter range the pulse area is independent of the chirp and hence $\Theta_{\mathrm{LZ}} \approx \Theta_{\mathrm{R}} = \Theta$.

The equations in 3.5.2 are plotted in Figure 3.5.1. For small pulse areas, both functions $P_{2,\mathrm{LZ}}(\Theta)$ and $P_{2,\mathrm{Rabi}}(\Theta)$ are identical in their rise behaviour:

$$P_{2,\mathrm{LZ}}(\Theta) = \frac{\Theta^2}{4} + O\left(\Theta^4\right) \qquad P_{2,\mathrm{Rabi}}(\Theta) = \frac{\Theta^2}{4} + O\left(\Theta^4\right). \tag{3.5.6}$$

For higher pulse areas the occupation oscillates as a function of the pulse area without chirp and stays constant at 1 with chirp. The magnitude of the chirp does not influence the curve significantly. Even for the extreme case $\psi_2/\tau_0^2 = 10^4$ (green curve) the deviation is minimal. In the experiments we work with ψ_2/τ_0^2 up to 100. The RAP curve reaches an occupation of 92 % at a pulse area of π, slightly depending on the chirp. For higher pulse areas the occupation reaches 100 % and stays constant.

As stated in the last section, the Landau-Zener model assumes a rectangular pulse with constant Rabi frequency. Nevertheless, we use it here as simple model to approximatively describe the physics even with a Gaussian variation of the Rabi frequency. The approximation becomes valid due to our choice of pulse parameter. We use a spectral bandwidth of the pulses of around 15 meV, much larger than the linewidth of the resonance of a few µeV and also larger than the Rabi frequencies. Furthermore, the peak of the laser spectrum is chosen to lie close to the resonance. This means that in the region of the avoided crossing, the Rabi frequency is approximately constant in time, such that the Landau–Zener model is a reasonable one to describe our experiments. We use it to develop an analytical model to simulate the coherent nano imaging with a two-pulse RAP sequence in Section 3.6 which is applied in Chapter 6. However, for experiments in Chapters 5 and 4 we take the full Gaussian function of the pulses into account for numerical simulations which also involves an interaction with phonons in the semiconductor material.

3.6 Coherent Diffraction-Unlimited Imaging with Two-pulse RAP

3.6.1 Introduction to Diffraction-Unlimited Nano Imaging in the Far-Field

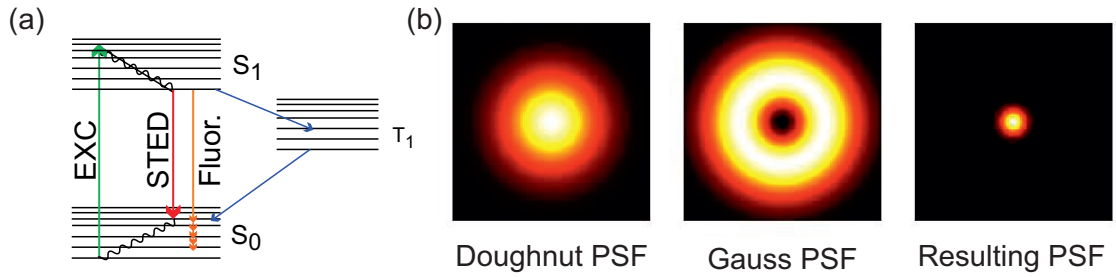

Figure 3.6.1: **Concept of the conventional STED nano imaging (a)** Level scheme adapted from [Hell, 2003] **(b)** Point spread functions of the Gaussian excitation beam, of the doughnut depletion (STED) beam and of the resulting emission. Adapted under CC BY-SA 3.0 from Marcel A. Lauterbach.

In conventional far-field microscopy the smallest distance d between still distinguishable objects in the focal plane is limited by diffraction. Ernst K. Abbe published the law of the diffraction limit for conventional microscopes in 1873. It says $d = \lambda/(2n \sin\alpha)$, where λ is the wavelength of the light, n the refractive index and α the half angle of the objective. More than hundred years later, Stefan W. Hell published the first proposal to overcome the diffraction limit in the far-field microscopy. He paved the way for a super resolution fluorescence microscopy using stimulated emission depletion (STED) [Hell and Wichmann, 1994]. The idea was to excite fluorophores in a diffraction limited focal spot with a laser pulse and then, before the fluorophores re-emit light, to deplete the molecules in a part of that area with one or two additional laser pulses. Hence, the remaining effective area of molecules capable of emitting light is reduced below the diffraction limit, here so far only in one dimension. In other words, a first pulse switches the fluorescence ON in a diffraction limited area and a second pulse (or two) switches it OFF in some part of this area reducing the effective fluorescing area below the diffraction limit.

The concept of STED requires a certain level structure of the emitters being imaged. There are at least four levels involved. A scheme of the level structure is shown in Figure 3.6.1(a). The first

laser pulse (EXC) excites the molecule from the ground state S_0 to the excited state S_1. Both levels have multiple vibrational sub-levels with very fast, non-radiative decay times. The delay between the first pulse (EXC) and the second pulse (STED) is chosen to be long enough to facilitate a relaxation into the lowest vibrational sub-level of the excited state. In areas without the depletion beam, in ON-areas, the system radiatively decays to the sub-levels of the ground state: it emits light by spontaneous emission. On the other hand in OFF-areas, after the non-radiative decay the STED beam depletes the lowest level of the excited state by means of stimulated emission. A fast non-radiative decay of the higher sub-levels of the ground state S_0 avoids re-excitation by the STED pulse provided that the STED beam is spectrally narrow.

Five years after Hell's proposal the first experimental proof of concept was published [Klar and Hell, 1999]. A Gaussian pulse was used to switch on the florescence of the marker molecule Pyridine 2. Subsequent to the first pulse, a second pulse with a delay of a few picoseconds and shifted in space with respect to the first beam switched the molecule off in one of the wings of the first pulse. A resolution improvement of 1.5 was achieved in one dimension, the first evidence of STED. One year later, already a factor of six along the optical axes and a factor of two in radial direction was achieved [Klar et al., 2000].

The next milestone after the proof of concept was reached by Westphal et al. in 2005 [Westphal and Hell, 2005]. Here, it was new to use a doughnut shaped focus for the STED pulse. This doughnut focus features a zero in intensity in the centre surrounded by a ring of high intensity as shown in Figure 3.6.1(b). The doughnut focus allows a symmetric depletion around the centre of the Gaussian focus (the excitation beam) everywhere where the intensity surpasses the threshold for depletion. The resulting point spread function is a small circle as shown on the right panel in Figure 3.6.1(b). In addition, they found a square root law connecting the intensity in the doughnut beam to the effective width of the point spread function. By increasing the intensity in the doughnut beam to extremely high values ($1\,\mathrm{GW\,cm^{-2}}$), the width of the effective point spread function was reduced to below 30 nm with an excitation wavelength of around 700 nm. Two dimensional images were recorded by scanning the sample.

STED became since then a very versatile technique with a broad bandwidth of applications, mainly in biological systems but not only. In 2009 the concept of STED was transferred by Rittweger et al. from fluorescence markers to a solid state system, namely a nitrogen-vacancy-centre in diamond [Rittweger et al., 2009]. A resolution down to slightly below 6 nm was achieved. Later, Wildanger et al. used STED to image the electron spin resonance in a nitrogen-vacancy-centre [Wildanger et al., 2011, 2012].

Besides the conventional STED technique, several imaging techniques not limited by diffraction were developed in parallel over the last years and are summarised for example in the review from S. W. Hell [Hell, 2007]. The techniques can be sorted into two classes.

The first class is called RESOLFT (REversible Saturable Optical Linear Fluorescence Transitions) and includes besides others STED and ground-state-depletion (GSD) [Bretschneider et al., 2007]. GSD uses a metastable dark-state as OFF state. All of them involves a switching technique and different intermediate states. They differ in the marker and in the ON, OFF states used.

The other class use statistical methods to localise single molecules at a time and then reconstruct the image in post-processing. Members of this class are PALM (photo activated localization microscopy) [Betzig et al., 2006] and STORM (stochastic optical reconstruction microscopy) [Rust et al., 2006] among others. Something that should be mentioned is that these techniques do not overcome the diffraction limit during the imaging but use a statistical technique to localise single molecules one at a time in a diffraction limited spot. The reconstructed image is not limited by diffraction [Betzig et al., 2006]. The requirements here are a low emitter concentrations and a low intensity excitation in order to prevent an excitation of two emitters at a time.

A problem in most of the techniques mentioned above is caused by blinking and photo-bleaching. During the scanning, single molecules are often switched on and off with high intensities. The probability for fluorophores to end in a dark-state and be temporally invisible in the imaging

increases with both the intensity as well as with the number of ON-OFF cycles. Even more, the fluorophore molecule can be irreversibly damaged by the high intensities.

We developed, in this thesis, a new technique for optical, diffraction unlimited imaging in the far-field. Our approach differs from all the techniques mentioned above in two main aspects. First, our approach is a coherent and diffraction unlimited imaging (in contrast to a coherent localization technique, e.g. [Gerhardt et al., 2010]) and does not rely on an incoherent process mediated by vibrational sub-levels. Second, our imaging method is as universal as one can imagine. It involves only two energy levels and a resonant, coherent transfer between them. The first state is the OFF state, the ground state $|1\rangle$, and the second state is the ON state, the excited state $|2\rangle$.

We adapt the existing concept of an ON- and OFF-switch with a Gaussian and a doughnut shaped point spread function and combine it with a universal coherent control technique: rapid

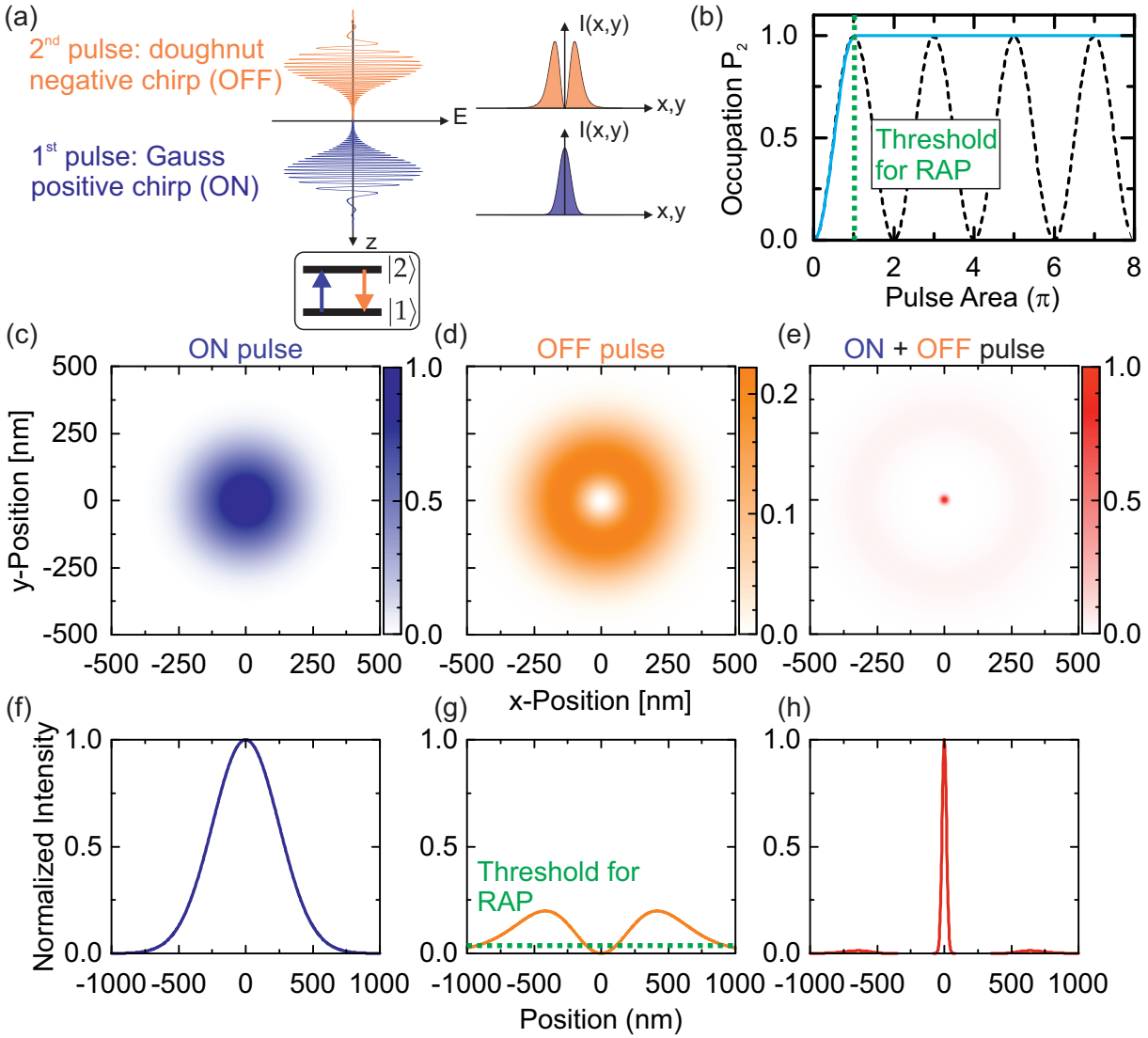

Figure 3.6.2: **Concept of our coherent nano imaging with RAP (a)** A sequence of two chirped pulses with different spatial profiles in the focal plane switches two-level system ON or 'ON and OFF' by means of RAP depending on the beam intensity at the particular position. **(b)** Response of the two-level system to a chirped pulse. Above the threshold the inversion fidelity is 1. RAP is a near ideal ON-OFF-switch. The threshold of the RAP-switch is shown with a green, dashed line. **(c-e)** Intensity profile as function of sample (x, y) position for only the ON pulse (c), only the OFF pulse (d) and ON pulse followed by the OFF pulse (e). **(f-h)** One dimensional cut through (c-e). In (g) the threshold of the RAP-switch is schematically depicted with a green, dashed line.

adiabatic passage. The concept is explained in a sketch in Figure 3.6.2. The requirements of our technique are minimal: a two-level system, a pair of broad-band chirped pulses, one with a Gaussian spatial profile and one with a doughnut spatial profile and a dark-field technique to suppress back-reflected laser light. That is all. The non-linear behaviour of RAP, a constant occupation of one above the threshold in intensity, is in our opinion an ideal match for the ON-OFF-switch concept.

The broad bandwidth of the RAP pulses facilitates an inherent multiplex capacity of the technique. Emitters with varying resonance condition within the bandwidth of the excitation can all be simultaneously be switched with the same pulse. In the detection the spectral information of individual emitters is conserved.

The energy dissipation per pulse in our concept is ideally zero due to the resonant driving of the two-level system and it is in fact very close to zero (as shown in Chapter 4). Therefore, we expect the problem of photo-bleaching and blinking to be less significant if existing at all with our approach.

In the following section of the chapter, we present an analytical model to describe and simulate the whole imaging experiment. The experimental realisation and first successful results are presented in Chapter 6.

3.6.2 Analytical Model

On the basis of the scalar diffraction theory and using the Landau-Zener factor we developed a model to simulate the spatial emission pattern of a QD subsequent to an excitation with a two-pulse sequence of chirped pulses. The model describes for both beams, the Gaussian beam as well as the doughnut shaped beam, the effect of their intensities as well as their spot sizes on the resulting emission profile and its spatial extent.

The Scalar Diffraction Theory

A doughnut shaped focus can be achieved experimentally with a 2π vortex phase plate (VPP) in the corresponding excitation arm of the microscope as described in Section 2.2. The effect of the phase plate is mathematically implemented in our model by adding a phase term $e^{i\phi}$ with the azimuthal angle ϕ in the complex E-field propagating towards the lens.

We use the scalar diffraction theory to transform the electric field (E-field) incident on the objective into the field distribution in the focal plane. There are two models describing the E-field before the objective that are analytically solvable and physically realistic.

The first one is to treat the E-field as a plane wave incident on the aperture of the objective. The lens and diffraction of the aperture transform the plane wave (no VPP) into a Bessel function describing the well known Airy discs. In contrast to that, the plane wave with the additional phase term from the VPP is transformed into a combination of Struve and Bessel functions, describing a doughnut shaped focus [Neupane et al., 2013].

In the second model, the E-field has a Gaussian wavefront and incidents on an objective lens with an infinitely large aperture. This model is chosen for the development of the imaging simulation. The choice is approved later by comparing both models to experimental data in Figure 3.6.3. The FWHM of the beam before the objective is $\Delta R_{I,\mathrm{FWHM}} = 2\sqrt{\ln(2)}\ \sigma$. The diffracted fields as function of the wave vector k are thus calculated as:

$$E_{\mathrm{G}}(k) = E_{0\mathrm{G}}/2 \int_{r=0}^{r=\infty} \int_{\phi=0}^{\phi=2\pi} e^{-i[kr\sin(\theta)\cos(\phi)+kr\cos(\theta)\sin(\phi)]-\frac{r^2}{2\sigma^2}} r\,\mathrm{d}r\mathrm{d}\phi + c.c. \text{ and} \tag{3.6.1}$$

$$E_{\mathrm{D}}(k) = E_{0\mathrm{D}}/2 \int_{r=0}^{r=\infty} \int_{\phi=0}^{\phi=2\pi} e^{-i[kr\sin(\theta)\cos(\phi)+kr\cos(\theta)\sin(\phi)]-\frac{r^2}{2\sigma^2}+i\phi} r\,\mathrm{d}r\mathrm{d}\phi + c.c.\,. \tag{3.6.2}$$

We assumed a radial symmetry of the problem and set without loss of generality the spherical coordinate θ to zero. The solution for E_G (no VPP) is a Gaussian and the solution for E_{D} (with

VPP) is a Gaussian weighted by Bessel functions and a linear function:

$$E_G(k) = E_{0G} \exp\left(-\frac{k^2\sigma^2}{2}\right) \tag{3.6.3}$$

$$E_D(k) = \frac{E_{0D}}{2}\sqrt{\frac{\pi}{2}}\, k\sigma\, \exp\left(-\frac{k^2\sigma^2}{4}\right)\left[I_0\left(\frac{k^2\sigma^2}{4}\right) - I_1\left(\frac{k^2\sigma^2}{4}\right)\right] \tag{3.6.4}$$

with I_0 and I_1 being the Bessel functions of the first kind $I_n(x)$ with $n = 0$ and $n = 1$, respectively. The FWHM of the Gaussian electric field distribution is $\Delta k_{E,\mathrm{FWHM}} = 2\sqrt{2\ln(2)}/\sigma$.

The wave vector k is transformed by the lens into a real space position (x, y). In a small angle approximation (assuming $\sqrt{x^2+y^2} \ll f$) the transformation is given by equation 3.6.5, where f, λ and n_{SIL} are the focal length, the centre wavelength of the light and the refractive index of the solid immersion lens, respectively. The intensity distributions as a function of the real space position are drawn in Figure 3.6.3(a).

$$k(x,y) = \frac{2\pi\sqrt{x^2+y^2}}{f\lambda/n_{\mathrm{SIL}}} \tag{3.6.5}$$

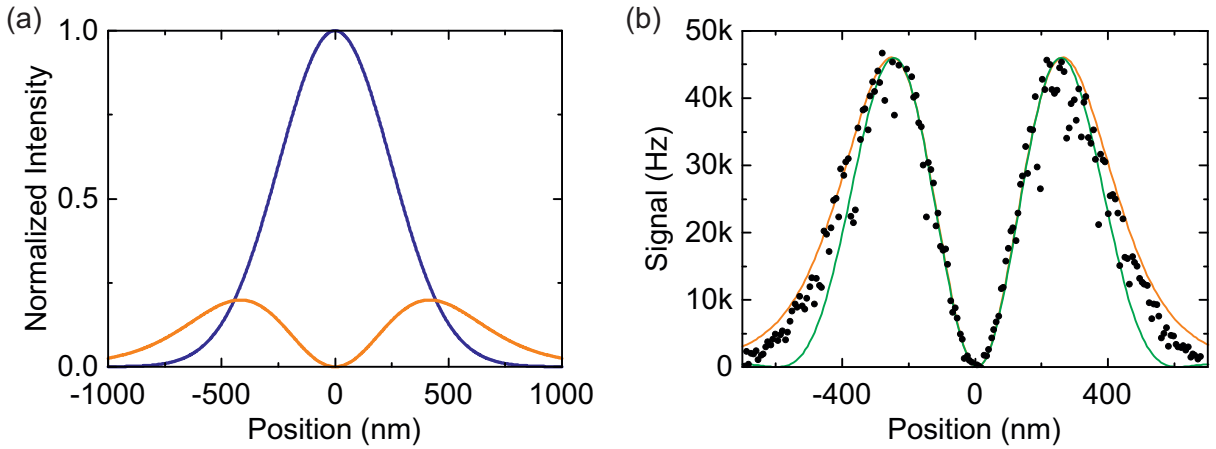

Figure 3.6.3: **Gauss and doughnut focal intensity distributions; and Gauss wavefront versus plane wavefront. (a)** $|E_G(x, y = 0)|^2$ and $|E_D(x, y = 0)|^2$ in eq. 3.6.3, 3.6.4 are plotted with $E_G^0 = E_D^0 = 1$ in blue and orange, respectively. **(b)** The solid curves show the calculated doughnut foci for a Gaussian wavefront incident on the objective lens (orange) and for a plane wavefront incident on the aperture of the objective lens (green). In our microscope the situation is in-between these two cases: a Gaussian wavefront is cut and diffracted by the aperture of the objective lens. We measured the point spread function (black circles) with a quantum dot and left circularly polarised light. In (b) the resolution increment through the confocal detection is also taken into account in the calculated curves. Parameters for the calculation in (a) and (b) are $\lambda = 940\,\mathrm{nm}$, $n_{\mathrm{SIL}} = 2.13$, $\Delta R_{I,\mathrm{FWHM}} = 2.0\,\mathrm{mm}$ ($\sigma = 1.2\,\mathrm{mm}$), $f = 5.9\,\mathrm{mm}$

In Figure 3.6.3(b) the calculated doughnut shaped foci for both models (plane wave, Gaussian wave) are plotted (green, orange) together with an experimental measured point spread function (black circles). The real experiment lies somewhere between the two ideal cases, slightly closer to the Gaussian case. This is in good agreement with our expectations since in our microscope the Gaussian mode of a single-mode glass fibre is collimated and sent into the finite clear aperture of the objective resulting in a clipping at about $1/e^2$ of the peak intensity. We choose for the rest of our calculations a Gaussian wavefront, although we want to note that the results are qualitatively similar with a plane wavefront.

Inversion Probability with Rapid Adiabatic Passage

With the knowledge of the electric field distributions in the focal spot, we can use the Landau-Zener factor introduced in equation 3.3.5 to calculate the occupation probability of the excited state in

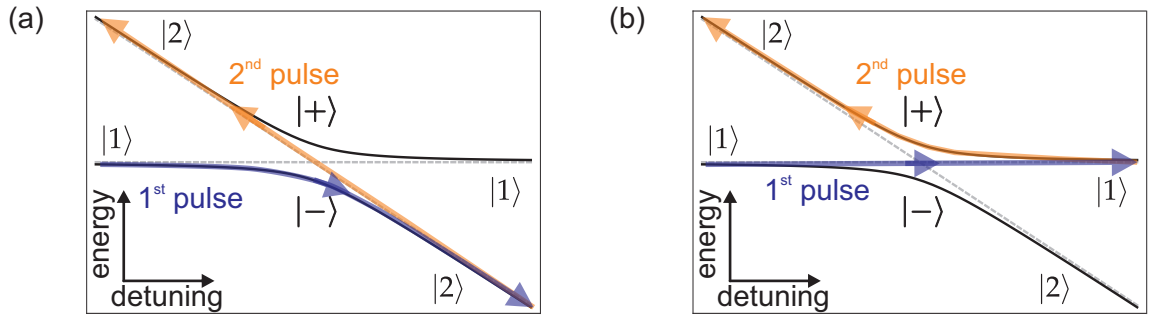

Figure 3.6.4: Two possible paths **(a)**, **(b)** with a two pulse sequence ending in the $|2\rangle$ state.

the two-level system. The nano imaging relies on a sequence of two pulses: the positively chirped Gauss pulse followed by the negatively chirped doughnut pulse. In a RAP excitation with this two-pulse sequence there are two possible paths reaching the excited state as final state as shown in the Landau-Zener level diagram in Figure 3.6.4. Thus, the individual probabilities for the system to end up in the excited state after an interaction with a two-pulse sequence with opposite sign of the chirps are:

$$p_{2,(a)} = (1 - p_{\mathrm{LZ}}(\Omega_{\mathrm{G}}, \alpha_{\mathrm{G}})) \times p_{\mathrm{LZ}}(\Omega_{\mathrm{D}}, \alpha_{\mathrm{D}}) \tag{3.6.6}$$

$$p_{2,(b)} = p_{\mathrm{LZ}}(\Omega_{\mathrm{G}}, \alpha_{\mathrm{G}}) \times (1 - p_{\mathrm{LZ}}(\Omega_{\mathrm{D}}, \alpha_{\mathrm{D}})), \tag{3.6.7}$$

where Ω is the angular Rabi frequency with $\Omega_{\mathrm{G,D}}(k) = E_{\mathrm{G,D}}(k)\ \vec{\mu}_{21}\hat{\epsilon}/\hbar$ and α is the sweep rate, for the Gauss and doughnut pulse, respectively. Adding them together leads to the total probability $p_2 = p_{2,(a)} + p_{2,(b)}$ for the system to be in the excited state after the two pulse sequence:

$$p_2 = p_{\mathrm{LZ}}(\Omega_{\mathrm{G}}, \alpha_{\mathrm{G}}) + p_{\mathrm{LZ}}(\Omega_{\mathrm{D}}, \alpha_{\mathrm{D}}) - 2p_{\mathrm{LZ}}(\Omega_{\mathrm{G}}, \alpha_{\mathrm{G}})p_{\mathrm{LZ}}(\Omega_{\mathrm{D}}, \alpha_{\mathrm{D}}). \tag{3.6.8}$$

The emission rate of the two level system is proportional to p_2. In order to describe the signal in the detection we multiply p_2 with the Gaussian point spread function of the detection $\exp\left(-k^2\sigma^2\right)$. Expressing the Rabi frequencies with the electric fields from eq. 3.6.3 and 3.6.3 leads to the signal as function of k:

$$\begin{aligned} S(k) = &\exp\left(-\frac{\pi\Omega_{0\mathrm{G}}^2}{2\alpha}\exp\left(-k^2\sigma^2\right) - k^2\sigma^2\right) \\ &\left[1 + \left(\exp\left(\frac{\pi\Omega_{0\mathrm{G}}^2}{2\alpha}\exp\left(-k^2\sigma^2\right)\right) - 2\right)\right. \\ &\left.\exp\left(-\frac{\pi^2k^2\sigma^2\Omega_{0\mathrm{D}}^2}{16\alpha}\exp\left(-\frac{k^2\sigma^2}{2}\right)\left(I_0\left(\frac{k^2\sigma^2}{4}\right) - I_1\left(\frac{k^2\sigma^2}{4}\right)\right)^2\right)\right], \end{aligned} \tag{3.6.9}$$

with the peak Rabi frequencies $\Omega_{0\mathrm{G}} = E_{0\mathrm{G}}\ \vec{\mu}_{21}\hat{\epsilon}/\hbar$, $\Omega_{0\mathrm{D}} = E_{0\mathrm{D}}\ \vec{\mu}_{21}\hat{\epsilon}/\hbar$ and the chirp rate $\alpha = \alpha_{\mathrm{G}} = -\alpha_{\mathrm{D}}$. We assume for simplicity an equal absolute magnitude of the chirp in the two pulses.

The result of the simulation, $S(k)$ or $S(x, y)$ is plotted for the Gauss pulse alone ($\Omega_{0\mathrm{G}} \neq 0$, $\Omega_{0\mathrm{D}} = 0$), the doughnut pulse alone ($\Omega_{0\mathrm{G}} = 0$, $\Omega_{0\mathrm{D}} \neq 0$) and with the doughnut pulse following the Gauss pulse in Figure 3.6.5.

Analytical Formula for the Effective Focal Spot Size

We use the model to deduce an analytical solution for the FWHM of the resulting emission peak as for example shown in Figure 3.6.5(c). The easiest way is to make an approximation right at the beginning of the derivation. Another approach, where we make an approximation at the end during

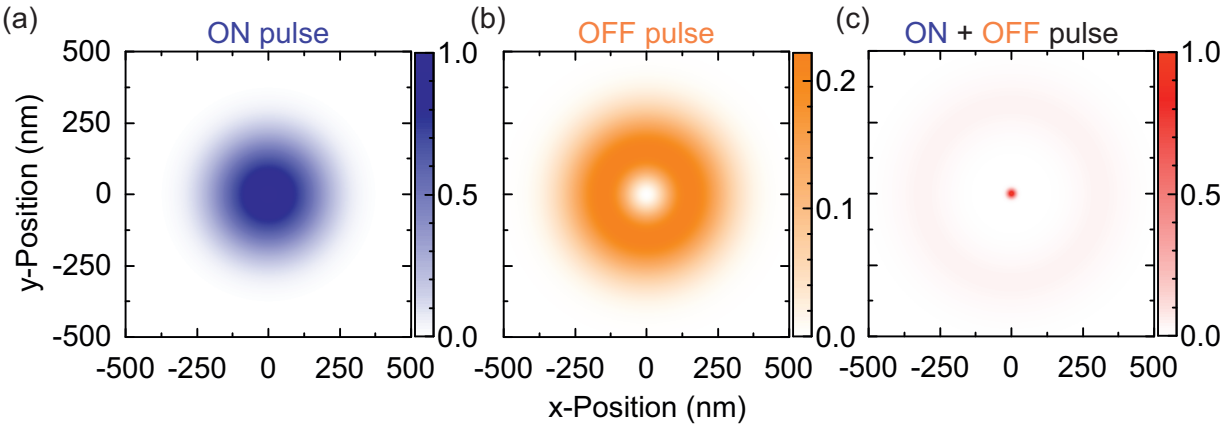

Figure 3.6.5: **Simulation of the imaging experiment.** The signal S as a function of sample (x, y)-position. **(a)** Gauss pulse only with $I_G^0 = 1I_T$; **(b)** doughnut pulse only with $I_D^0 = 1I_T$; **(c)** Gauss pulse $I_G^0 = 3I_T$ followed by doughnut pulse $I_D^0 = 205I_T$ resulting in a 15 times smaller spot size. Here we used the following parameters: wavelength 940 nm, refractive index solid immersion lens $n_{\mathrm{SIL}} = 2.13$, beam diameter before the objective $\Delta R_{I,\mathrm{FWHM}} = 2.0\,\mathrm{mm}$, focal length $f = 3.7\,\mathrm{mm}$, chirp $\alpha_{\mathrm{G}} = -\alpha_{\mathrm{D}} = 3.24\,\mathrm{ps}^{-2}$.

the actual calculation of the FWHM using the full model in eq. 3.6.9, is given in the appendix of this chapter. Here, we simplify the doughnut intensity distribution using a parabola:

$$I_{\mathrm{D}}(k) \propto E_{0\mathrm{D}}^2 \frac{\pi}{8} k^2 \sigma^2 \tag{3.6.10}$$

$$E_{\mathrm{D}}(k) \approx E_{0\mathrm{D}} \sqrt{\frac{\pi}{8}} k\sigma \tag{3.6.11}$$

The strategy to calculate the FWHM is to derive an analogous equation to eq. 3.6.9 with the parabola, S_{para} and then solve $S_{\mathrm{para}}(k_0) - S_{\mathrm{para}}(k=0)/2 = 0$ for k_0, since $\Delta k_{\mathrm{FWHM}} = |2k_0|$.

$$\begin{aligned}
S_{\mathrm{para}}(k_0) - S_{\mathrm{para}}(k=0)/2 = &-\frac{1}{2} && \text{(3.6.12a)}\\
&+\frac{1}{2}\exp\left(-\frac{\pi\Omega_{0\mathrm{G}}^2}{2\alpha}\right) && \text{(3.6.12b)}\\
&+\exp\left(-\frac{\pi\Omega_{0\mathrm{G}}^2}{2\alpha}\exp\left(-k_0^2\sigma^2\right) - k_0^2\sigma^2\right) && \text{(3.6.12c)}\\
&+\exp\left(-k_0^2\sigma^2\frac{16\alpha + \pi^2\Omega_{0\mathrm{D}}^2}{16\alpha}\right) && \text{(3.6.12d)}\\
&-2\exp\left(-\frac{\pi\Omega_{0\mathrm{G}}^2}{2\alpha}\exp\left(-k_0^2\sigma^2\right) - k_0^2\sigma^2\frac{16\alpha + \pi^2\Omega_{0\mathrm{D}}^2}{16\alpha}\right) && \text{(3.6.12e)}
\end{aligned}$$

The terms (3.6.12b), (3.6.12c) and (3.6.12e) converge towards zero if $\Omega_{0\mathrm{G}} > \Omega_{\mathrm{T}} = 4\sqrt{\alpha}/\pi$. Hence, we can neglect them assuming an intensity above the threshold in the Gaussian beam:

$$S_{\mathrm{para}}(k_0) - S_{\mathrm{para}}(k=0)/2 \approx -\frac{1}{2} + \exp\left(-k_0^2\sigma^2\frac{16\alpha + \pi^2\Omega_{0\mathrm{D}}^2}{16\alpha}\right) = 0. \tag{3.6.13}$$

Solving equation 3.6.13 for k_0 leads to the FWHM of the STED peak $\Delta k_{\mathrm{FWHM}} = |2k_0|$ under the assumption that the power in the Gauss pulse and in the doughnut-shaped pulse are above the

threshold:

$$\Delta k_{I,\mathrm{FWHM}} = \frac{\sqrt{2}}{\sigma}\frac{\sqrt{\ln 4}}{\sqrt{1+\frac{\pi^2\Omega_{0\mathrm{D}}^2}{16\alpha}}} \tag{3.6.14a}$$

$$= \frac{\Delta k^0_{E,\mathrm{FWHM}}}{\sqrt{2}}\frac{1}{\sqrt{1+\frac{\pi^2\Omega_{0\mathrm{D}}^2}{16\alpha}}} \tag{3.6.14b}$$

$$= \frac{\Delta k^0_{I,\mathrm{FWHM}}}{\sqrt{1+\frac{\pi^2\Omega_{0\mathrm{D}}^2}{16\alpha}}} = \frac{\Delta k^0_{I,\mathrm{FWHM}}}{\sqrt{1+(\Omega_{0\mathrm{D}}/\Omega_{\mathrm{T}})^2}}, \tag{3.6.14c}$$

or equivalently in the x direction:

$$\Delta x_{I,\mathrm{FWHM}} = \frac{\sqrt{2}}{\sigma}\frac{\sqrt{\ln 4}}{\sqrt{1+\frac{\pi^2\Omega_{0\mathrm{D}}^2}{16\alpha}}} \tag{3.6.15a}$$

$$= \frac{\Delta x^0_{E,\mathrm{FWHM}}}{\sqrt{2}}\frac{1}{\sqrt{1+\frac{\pi^2\Omega_{0\mathrm{D}}^2}{16\alpha}}} \tag{3.6.15b}$$

$$= \frac{\Delta x^0_{I,\mathrm{FWHM}}}{\sqrt{1+\frac{\pi^2\Omega_{0\mathrm{D}}^2}{16\alpha}}} = \frac{\Delta x^0_{I,\mathrm{FWHM}}}{\sqrt{1+(\Omega_{0\mathrm{D}}/\Omega_{\mathrm{T}})^2}}. \tag{3.6.15c}$$

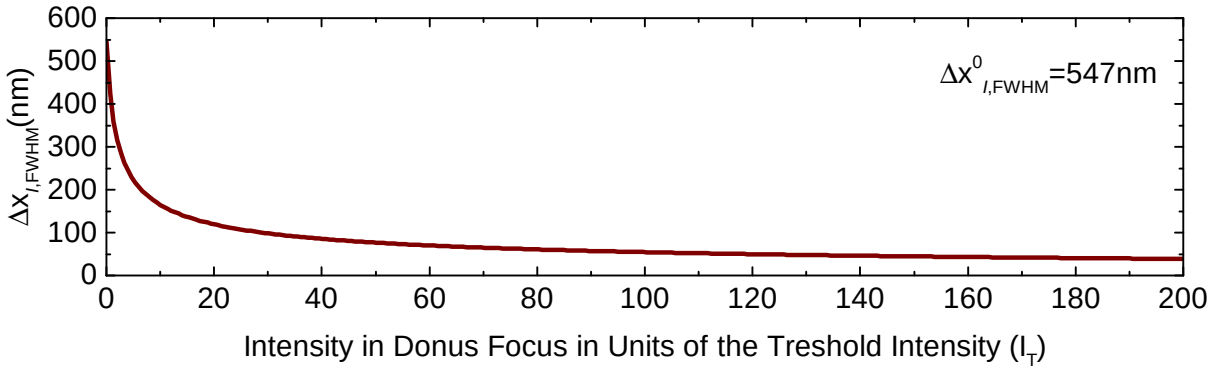

Figure 3.6.6: **Effective focal spot size, model: analytical solution.** The FWHM of the effective focal spot is plotted as function of the intensity in the doughnut focus in units of the threshold intensity. The diffraction limit is here $\Delta x^0_{I,\mathrm{FWHM}} = 547\,\mathrm{nm}$.

The threshold Rabi frequency defined earlier as $\Omega_T = 4\sqrt{\alpha}/\pi$ corresponds to a pulse area of $\Theta(\Omega_{\mathrm{T}}) = \sqrt{32/\pi} \approx 1.02\pi$ (using eq. 3.5.1) and hence an occupation probability of ~92 % with a single RAP pulse. For the experiments it is also useful to relate the FWHM of the effective focal spot to the intensities of the excitation pulses. Therefore, we transform the Rabi frequencies in intensities with $I = 1/2c\epsilon_0 n(\hbar\Omega)^2/(\vec{\mu}_{21}\hat{\epsilon})^2$:

$$\Delta x_{I,\mathrm{FWHM}} = \frac{\Delta x_{I,\mathrm{FWHM}}}{\sqrt{1+\frac{I_{0\mathrm{D}}}{I_{\mathrm{T}}}}}, \tag{3.6.16}$$

$$I_{\mathrm{T}} = \frac{8\alpha\hbar^2 c\epsilon_0 n}{\pi^2(\vec{\mu}_{21}\hat{\epsilon})^2}. \tag{3.6.17}$$

The equation 3.6.16 is plotted in Figure 3.6.6. A decrease of the effective focal spot size proportional to the square root of the intensity in the doughnut focus is visible. This functional relation is

matches the result known from STED experiments. This can be understand by considering the depletion behaviour in STED. The saturation of the depletion function [Klar et al., 2000, Fig. 2a] has a similar exponential decay as P_{LZ}.

The particular effect of the intensity in the Gaussian focus as well as in the doughnut shaped focus is shown in Figure 3.6.7. The first row reproduces the outcome of Figure 3.6.5. In the second row the decrease of the focal spot size with increasing doughnut intensity as discussed above is demonstrated in two dimensions. The third row shows how the non-linear response of RAP effects the focal spot size of a single Gaussian spot: for high intensities the resolution is decreased by a factor of $\sqrt{2}$, the factor we earn in a confocal detection. Here, the original Gaussian excitation becomes effectively rectangular due to the RAP effect, the collection is still Gaussian and therefore we lose at most the confocal factor.

Another interesting effect is demonstrated in the last row. When decreasing the Gauss intensity towards the threshold and further below the threshold while having a fixed doughnut intensity far above the threshold, a ring around the centre appears, becomes stronger and grows towards the centre. In these cases the much weaker Gauss pulse is at its spatial edges not longer strong enough to invert the system and hence prepare the state for the following doughnut pulse. Then the much stronger doughnut pulse switches the two-level system at these positions ON instead of OFF and a ring appears. In confocal detection the collection efficiency decreases away from the centre which explains the weakening of the ring with increasing distance to the centre.

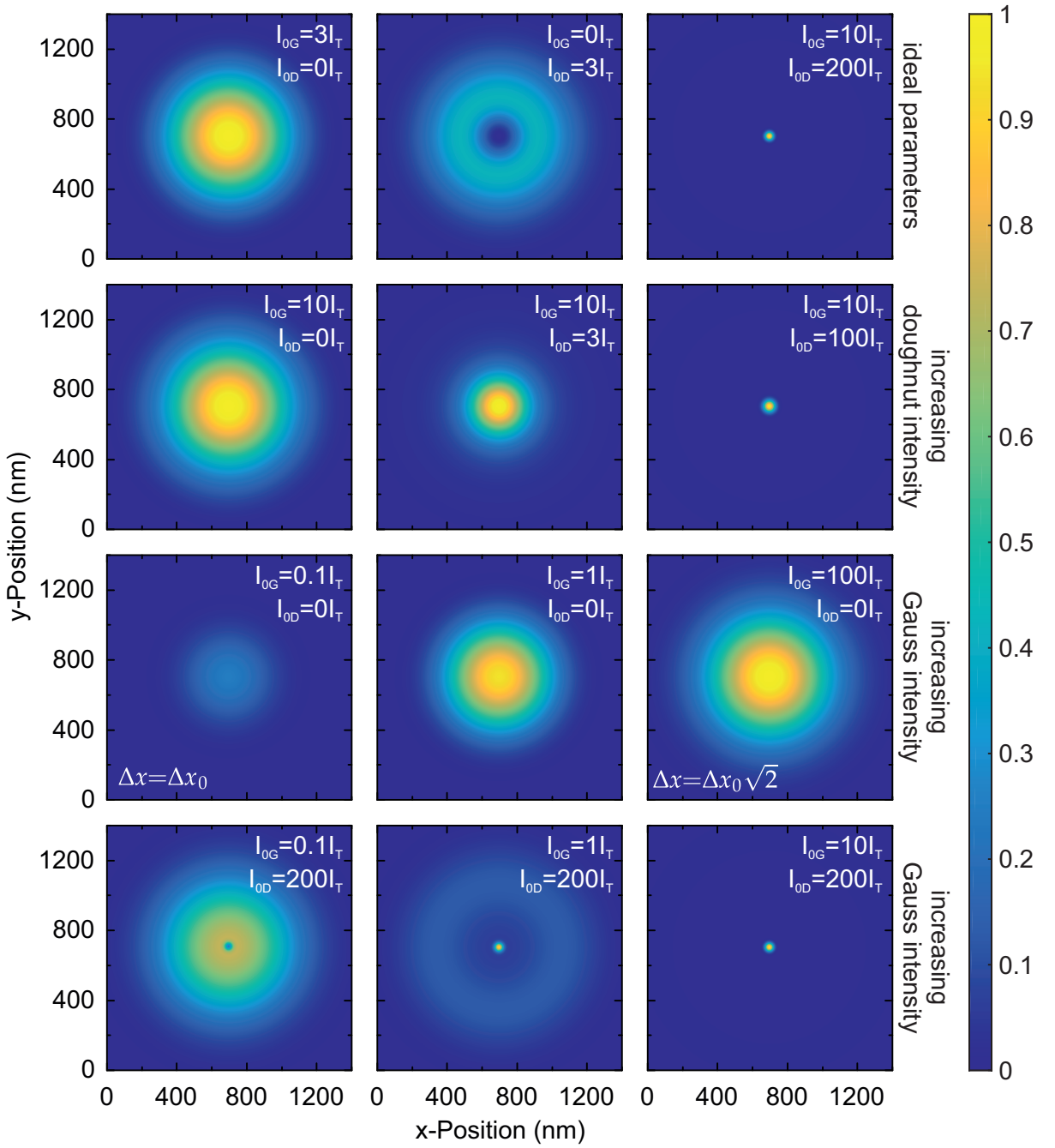

Figure 3.6.7: **Intensity dependency of the effective focal spot in the nano imaging model.** The intensities of the Gauss pulse and doughnut pulse are as stated in the panels. **First row:** Gauss pulse only, doughnut pulse only, both together for nano imaging. **Second row:** With a Gauss intensity above the threshold an increasing doughnut intensity decreases the effective spot size. **Third row:** With only the Gauss beam the effect on the FWHM caused by the non-linear intensity response of RAP is seen. The FWHM increases up to a factor of $\sqrt{2}$. **Fourth row:** For a fixed doughnut intensity far above the threshold a decreasing Gauss intensity causes the appearance of a ring around the central spot. This ring comes from an excitation by the doughnut beam in regions where the Gauss intensity was too weak to prepare the two-level system in the excited state. Parameters for the simulation are $\lambda = 940\,\mathrm{nm}$, $n_{\mathrm{SIL}} = 2.13$, $\Delta R_{I,\mathrm{FWHM}} = 2.0\,\mathrm{mm}$ ($\sigma = 1.2\,\mathrm{mm}$), $f = 5.9\,\mathrm{mm}$

Dependence of the Imaging Resolution on the Chirp

An obvious question is how to increase the resolution further with the RAP imaging technique. Equation 3.6.16 shows that the spot size can be decreased in two ways: increasing the intensity in the doughnut beam I_{0D} or decreasing the intensity threshold I_T by decreasing the sweep rate α. What is relevant in the first case is the peak intensity. The available laser source sets a limit, another limit is set by the damage threshold of the sample. One could consider to increase the resolution by decreasing the sweep rate by changing the amount of chirp. The problem here is that both the peak intensity as well as the sweep rate are functions of the chirp. For $\tau_0^2 \ll \psi_2$ we can simplify:

$$\alpha = \frac{\psi_2}{\tau_0^4 + \psi_2^2} \approx 1/\psi_2 \,, \tag{3.6.18}$$

$$I_{\text{peak}} \propto \frac{\tau_0}{\sqrt{\tau_0^4 + \psi_2^2}} \approx \frac{\tau_0}{\psi_2} \tag{3.6.19}$$

and hence, the Landau-Zener factor as well as the resolution in the RAP imaging experiment are independent of the chirp. The robustness of the Landau-Zener factor with respect to the chirp was already demonstrated in Figure 3.5.1. This is easily understood by considering that increasing the chirp decreases on the one hand the sweep rate but on the other hand the constant pulse energy is spread over a longer time scale and therefore the peak intensity decreases. Both effects cancel each other in the regime of strongly chirped pulses.

Beam Displacements

Another benefit of the model is that we can study the effect of a beam displacement with respect to the optical axis. This is shown in Fig. 3.6.8(b). In the right panel we simulated a displacement of the doughnut focus with respect to the detection focus. A displacement of $\Delta x = 20\,\text{nm}$ and $\Delta y = -20\,\text{nm}$ matches best our experimental data in the left panel. The measurement was performed with only the doughnut beam, left circularly polarised excitation and a QD as two-level system probe. As expected, the displacement does not change when scanning the sample; all QDs in a larger scan area showed the same slight distortion of the doughnut shape (not shown).

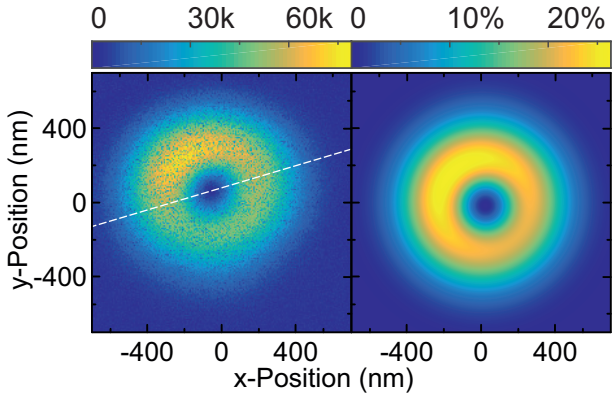

Figure 3.6.8: **Doughnut beam displacement.** Left: resonance fluorescence from a quantum dot measured with the doughnut shaped pulse alone and left circularly polarised excitation. The excitation intensity was $I_{0D} = 1.2 I_T$. A cut along the white dashed line is plotted in Fig. 3.6.3(b). Right: corresponding simulation with $I_{0D} = 1.2 I_T$, parameters as stated in Fig. 3.6.3 and a displacement of $\Delta x_D = 20\,\text{nm}$ and $\Delta y_D = -20\,\text{nm}$.

Appendix: Another Method for an Analytical Formula for the Effective Focal Spot Size

Another approach for an analytical formula estimating the FWHM of the effective focal spot is given in this appendix. The strategy here is to use the full model from eq. 3.6.9 and solve $S(k_0) - S(k=0)/2 = 0$ for k_0. The FWHM is then given by $\Delta k_{\mathrm{FWHM}} = |2k_0|$.

$$
\begin{aligned}
S(k_0) - S(k=0)/2 = &-\frac{1}{2} && \text{(3.6.20a)}\\
&+\frac{1}{2}\exp\left(-\frac{\pi\Omega_{0\mathrm{G}}^2}{2\alpha}\right) + \exp\left(-\frac{\pi\Omega_{0\mathrm{G}}^2}{2\alpha}\exp\left(-k_0^2\sigma^2\right) - k_0^2\sigma^2\right) && \text{(3.6.20b)}\\
&+\exp\left[-k_0^2\sigma^2\left[\frac{\pi^2\Omega_{0\mathrm{D}}^2}{16\alpha}\exp\left(-\frac{k_0^2\sigma^2}{2}\right)\right.\right. && \text{(3.6.20c)}\\
&\left.\left.\left(I_0\left(\frac{k_0^2\sigma^2}{4}\right) - I_1\left(\frac{k_0^2\sigma^2}{4}\right)\right)^2 + 1\right]\right]\\
&-2\exp\left[-\frac{\pi\Omega_{0\mathrm{G}}^2}{2\alpha}\exp\left(-k_0^2\sigma^2\right) - \frac{\pi^2 k_0^2\sigma^2\Omega_{0\mathrm{D}}^2}{16\alpha}\exp\left(-\frac{k_0^2\sigma^2}{2}\right)\right. && \text{(3.6.20d)}\\
&\left.\left(I_0\left(\frac{k_0^2\sigma^2}{4}\right) - I_1\left(\frac{k_0^2\sigma^2}{4}\right)\right)^2 - k_0^2\sigma^2\right],
\end{aligned}
$$

leading to a sum of five terms. The second, the third (3.6.20b) and the fifth (3.6.20d) terms converge towards zero for Rabi frequencies in the Gauss beam above the threshold $\Omega_{0\mathrm{G}} > \Omega_{\mathrm{T}} = 4\sqrt{\alpha}/\pi$. Hence, we can neglect them assuming an intensity above the threshold in the Gaussian beam:

$$
\begin{aligned}
S(k_0) - S(k=0)/2 \approx -\frac{1}{2} + \exp&\left[-k_0^2\sigma^2\left[\frac{\pi^2\Omega_{0\mathrm{D}}^2}{16\alpha}\exp\left(-\frac{k_0^2\sigma^2}{2}\right)\right.\right.\\
&\left.\left.\left(I_0\left(\frac{k_0^2\sigma^2}{4}\right) - I_1\left(\frac{k_0^2\sigma^2}{4}\right)\right)^2 + 1\right]\right]. \qquad \text{(3.6.21)}
\end{aligned}
$$

The remaining term, eq. 3.6.21 can be expanded by Taylor series around $k_0 = 0$:

$$
\begin{aligned}
S(k_0) - S(k=0)/2 \approx &+\frac{1}{2}\\
&-\frac{\left(16\alpha + \pi^2\Omega_{0\mathrm{D}}^2\right)}{16\alpha}k_0^2\sigma^2\\
&+\frac{\left(256\alpha^2 + 56\pi^2\alpha\Omega_{0\mathrm{D}}^2 + \pi^4\Omega_{0\mathrm{D}}^4\right)}{512\alpha^2}k_0^4\sigma^4\\
&-\frac{\left(4096\alpha^3 + 2376\pi^2\alpha^2\Omega_{0\mathrm{D}}^2 + 120\pi^4\alpha\Omega_{0\mathrm{D}}^4 + \pi^6\Omega_{0\mathrm{D}}^6\right)}{24576\alpha^3}k_0^6\sigma^6\\
&+O\left(k_0^8\right) \qquad \text{(3.6.22)}
\end{aligned}
$$

The series in order up to six in k_0 mimics perfectly the full function. A solution for the FWHM is found with an approximation quadratic in k_0. The distance of the two real roots of this function gives the FWHM in k:

$$
\begin{aligned}
\Delta k_{O(k^2),\mathrm{FWHM}} &= \frac{\sqrt{2}}{\sigma}\frac{1}{\sqrt{1+\frac{\pi^2\Omega_{0\mathrm{D}}^2}{16\alpha}}} && \text{(3.6.23)}\\
&= \frac{\Delta k_{I,\mathrm{FWHM}}}{\sqrt{2\ln(2)}}\frac{1}{\sqrt{1+\frac{\pi^2\Omega_{0\mathrm{D}}^2}{16\alpha}}}, && \text{(3.6.24)}
\end{aligned}
$$

But a comparison with numerical calculations with the full model shows that this result is too small by a factor of $\sqrt{2\ln 2}$.

Considering again the infinitely long Taylor expansion in eq. 3.6.22 and neglecting all terms besides terms with $\Omega_{0\mathrm{D}}^i/\alpha^j$ with $i+j \geq n$ in the order k^n results in an infinitely long series:

$$S(k_0) - S(k=0)/2 \approx \frac{1}{2} + \sum_{n=1}^{\infty} \left(-\frac{1}{2}\right)^n \frac{1}{n!} \left(\frac{k_0^2}{a}\right)^n \tag{3.6.25}$$

with $a = \sigma^2(16\alpha + \pi^2\Omega_{0\mathrm{D}}^2)/(8\alpha)$. Inserting the educated guess $k_0 = \sqrt{\ln(4)a}$ solves the system exactly:

$$S(k_0) - S(k=0)/2 \approx \frac{1}{2} + \sum_{n=1}^{\infty} \left(-\frac{1}{2}\right)^n \frac{1}{n!} \left(2\ln(2)\right)^n = 0. \tag{3.6.26}$$

The solution for k_0 is inserted in $\Delta k_{\mathrm{FWHM}} = |2k_0|$:

$$\Delta k_{I,\mathrm{FWHM}} = \frac{\sqrt{2}}{\sigma} \frac{\sqrt{2\ln 2}}{\sqrt{1 + \frac{\pi^2\Omega_{0\mathrm{D}}^2}{16\alpha}}} \tag{3.6.27a}$$

$$= \frac{\Delta k_{E,\mathrm{FWHM}}^0}{\sqrt{2}} \frac{1}{\sqrt{1 + \frac{\pi^2\Omega_{0\mathrm{D}}^2}{16\alpha}}} \tag{3.6.27b}$$

$$= \frac{\Delta k_{I,\mathrm{FWHM}}^0}{\sqrt{1 + \frac{\pi^2\Omega_{0\mathrm{D}}^2}{16\alpha}}} = \frac{\Delta k_{I,\mathrm{FWHM}}^0}{\sqrt{1 + (\Omega_{0\mathrm{D}}/\Omega_{\mathrm{T}})^2}}, \tag{3.6.27c}$$

or equivalent in x direction:

$$\Delta x_{I,\mathrm{FWHM}} = \frac{\sqrt{2}}{\sigma} \frac{\sqrt{2\ln 2}}{\sqrt{1 + \frac{\pi^2\Omega_{0\mathrm{D}}^2}{16\alpha}}} \tag{3.6.28a}$$

$$= \frac{\Delta x_{E,\mathrm{FWHM}}^0}{\sqrt{2}} \frac{1}{\sqrt{1 + \frac{\pi^2\Omega_{0\mathrm{D}}^2}{16\alpha}}} \tag{3.6.28b}$$

$$= \frac{\Delta x_{I,\mathrm{FWHM}}^0}{\sqrt{1 + \frac{\pi^2\Omega_{0\mathrm{D}}^2}{16\alpha}}} = \frac{\Delta x_{I,\mathrm{FWHM}}^0}{\sqrt{1 + (\Omega_{0\mathrm{D}}/\Omega_{\mathrm{T}})^2}}, \tag{3.6.28c}$$

This result is equivalent to the result obtained with the the quadratic approximation of the doughnut intensity profile.

Part II

Broadband Resonance Fluorescence and Rapid Adiabatic Passage on Single Quantum Dots

4 Entering a new Phonon Regime by Ultra-fast Rapid Adiabatic Passage

Adapted from:
"**Demonstrating the decoupling regime of the electron-phonon interaction in a quantum dot using chirped optical excitation**"

Timo Kaldewey[1], Sebastian Lüker[2], Andreas V. Kuhlmann[1,3], Sascha R. Valentin[4], Arne Ludwig[4], Andreas D. Wieck[4], Doris E. Reiter[2], Tilmann Kuhn[2], and Richard J. Warburton[1]

[1]Department of Physics, University of Basel, Klingelbergstrasse 82,
CH-4056 Basel, Switzerland

[2]Institut für Festkörpertheorie, Universität Münster, Wilhelm-Klemm-Strasse 10,
D-48149 Münster, Germany

[3]IBM Research-Zurich, Säumerstrasse 4,
CH-8803 Rüschlikon, Switzerland

[4]Lehrstuhl für Angewandte Festkörperphysik, Ruhr-Universität Bochum,
D-44780 Bochum, Germany

Submitted to: *Physical Review Letters*, November 2016

4.1 Abstract

Excitation of a semiconductor quantum dot with a chirped laser pulse allows excitons to be created by rapid adiabatic passage. In quantum dots this process can be greatly hindered by the coupling to phonons. Here we add a high chirp rate to ultra-short laser pulses and use these pulses to excite a single quantum dot. We demonstrate that we enter a regime where the exciton-phonon coupling is effective for small pulse areas, while for higher pulse areas a decoupling of the exciton from the phonons occurs. We thus discover a reappearance of rapid adiabatic passage, in analogy to the predicted reappearance of Rabi rotations at high pulse areas. The measured results are in excellent agreement with theoretical calculations.

4.2 Introduction

Phonons play a significant role in the ultra-fast quantum control of optical excitations in semiconductor quantum dots (QDs) [Reiter et al., 2014; Ramsay, 2010]. The phonons lead to a deterioration of the exciton preparation fidelity for schemes with resonant excitation for both unchirped [Ramsay et al., 2010a,b; Krügel et al., 2005; Vagov et al., 2007] and chirped pulses [Lüker et al., 2012; Gawarecki et al., 2012; Glässl et al., 2013; Mathew et al., 2014; Debnath et al., 2012; Wei et al., 2014]. The interaction with the phonons is sufficiently strong that state preparation relying on the electron-phonon interaction and a detuned pulse is possible [Reiter et al., 2012; Glässl et al.,

2013; Quilter et al., 2015; Bounouar et al., 2015; Ardelt et al., 2014]. A significant point is that the coupling to the phonons of an exciton in a QD depends non-monotonically on the phonon energy which, in optically driven QDs, translates into a non-monotonic dependence on the excitation power. Accordingly, excitation regimes can be found where the phonons are less influential [Wigger et al., 2014]. For Rabi rotations driven with resonant excitation of a QD, this leads to a fascinating behavior: for small pulse areas, almost no influence of the phonons is visible and almost unperturbed Rabi rotations can be achieved. With increasing pulse area, the coupling to the phonons leads to a damping of the Rabi rotations. This has been shown experimentally and the coupling to longitudinal acoustic (LA) phonons was identified as the main source of decoherence [Ramsay et al., 2010a,b]. For even higher pulse areas it has been predicted that the amplitude of the Rabi rotations should increase again, i.e. a so-called "reappearance" of the Rabi rotations is expected [Vagov et al., 2007]. The reason for the reappearance is a decoupling of the electron from the phonon system once the electronic oscillations are so fast that the phonons cannot follow anymore. The existence of a pulse area for which the coupling to the phonons is maximal is a direct consequence of the non-monotonic electron-phonon coupling [Vagov et al., 2007; Wigger et al., 2014]. We note that this phenomenon is quite different from the revival of occupation predicted in the Jaynes-Cummings model [Gerry and Knight, 2005], which occurs due to rephasing in time.

For Rabi rotations on self-assembled QDs, experiments have used $1-10$ ps laser pulses for which the reappearance regime can only be reached at extremely high pulse areas ($>20\pi$), too high to be reached experimentally. Here, we drive the QD with the full bandwidth of ~ 100 fs pulses such that the reappearance regime moves to much lower pulse areas ($>3\pi$). It is extremely difficult to avoid introducing chirp into ultra-fast laser pulses in a low temperature QD experiment. Instead, we embrace chirp: we deliberately introduce dispersion to the pulses and probe "rapid adiabatic passage" of the QD exciton. Rapid adiabatic passage (RAP) with the bandwidth of a $1-10$ ps laser pulse has been demonstrated [Simon et al., 2011; Wu et al., 2011] and phonons hinder the state preparation depending on the sign of the chirp [Lüker et al., 2012; Mathew et al., 2014]. It has been predicted that the Rabi reappearance regime translates to a non-monotonic RAP behavior as a function of the pulse area: at sufficiently high pulse areas RAP improves [Reiter et al., 2012]. We demonstrate this improvement here in a RAP experiment and present excellent agreement with theoretical calculations which account for the influence of the microscopic electron-phonon interaction on the QD exciton. We therefore present compelling evidence that we have entered the reappearance regime where the electronic system is effectively decoupled from the phonons. Furthermore, we argue that the reappearance phenomenon arises at smaller pulse areas in RAP than in a Rabi rotation for smoothly varying pulses.

4.3 Methods

We study a self-assembled InGaAs QD embedded in an n-i-p structure as displayed in Fig. 4.3.1(a). Detailed information about the structure can be found in the supplementary information (SI) (Section 4.5). By applying a gate voltage of 0.3 V, the QD is occupied by a single electron such that (in the absence of an external magnetic field) the QD mimics a two-level system. The ground state is the single electron state, $|\mathrm{e}^{1-}\rangle$, and the excited state the negatively-charged trion, $|\mathrm{X}^{1-}\rangle$. The QD is excited using chirped laser pulses. A passively mode-locked laser produces transform-limited pulses which are then manipulated in a folded $4f$ pulse-shaper [Martinez, 1987]. The transform-limited pulses have an intensity full-width-at-half-maximum (FWHM) of $\Delta t_{\mathrm{FWHM}} = 130\,\mathrm{fs}$ with close-to-Gaussian pulse form with $\Omega_0(t) = \frac{\Theta}{\tau_0\sqrt{2\pi}} \exp\left(-\frac{t^2}{2\tau_0^2}\right) \exp\left(-i\omega_L t\right)$, where Θ is the pulse area, $\tau_0 = \Delta t_{\mathrm{FWHM}}/(2\sqrt{\ln 2})$ is the pulse width and ω_L the center frequency. The Rabi frequency Ω is related to the electric field $\mathbf{E}$ of the laser pulse by the dipole matrix element $\mathbf{M}$ via $\hbar\Omega(t) = 2\mathbf{M}\cdot\mathbf{E}(t)$. The pulse-shaper adds a frequency dependent phase resulting in a chirp coefficient α. The chirp stretches the pulse in time to $\tau = \sqrt{\frac{\alpha^2}{\tau_0^2} + \tau_0^2}$. The instantaneous frequency of the laser pulse changes

in time with the frequency chirp rate $a = \mathrm{d}\omega/\mathrm{d}t = \frac{\alpha}{\alpha^2+\tau_0^4}$ [Malinovsky and Krause, 2001], such that after the pulse shaper the pulse reads

$$\Omega(t) = \frac{\Theta}{\sqrt{2\pi\tau_0\tau}} \exp\left(-\frac{t^2}{2\tau^2}\right) \exp\left(-i(\omega_L + \frac{1}{2}at)t\right). \tag{4.3.1}$$

The central wavelength ($2\pi c/\omega_L$) of the pulses is detuned by 2.58 nm from the trion transition, which corresponds to an energy of 3.63 meV. A chirp coefficient α of 0.31 ps^2 (0.66 ps^2) stretches the pulse length to 7 ps (15 ps). A sketch of the experiment is shown in Fig. 4.3.1(b): the QD at liquid helium temperature of $T = 4.2$ K is excited with a chirped pulse and the resonance fluorescence (RF) is detected. A scheme of the the complete set-up is described in the SI (Section 4.5.1). A cross-polarized dark-field technique suppresses the reflected laser light from the detection channel [Vamivakas et al., 2009; Yilmaz et al., 2010; Kuhlmann et al., 2013a,b]; further rejection of the laser light is carried out with a grating spectrometer (the laser pulse is broadband, the RF narrowband). The device works well even when excited with the broadband laser pulses. The Coulomb blockade is robust, which is confirmed in Fig. 4.3.1(c) showing the RF response to a broadband excitation as a function of the gate voltage (see also SI, Section 4.5.1). Within the X^{1-} plateau, RF emerges just from the X^{1-} validating the two-level assertion. For an excitation power of 0.9 µW or a pulse area of around π, the RF:background ratio is $\sim 100:1$, Fig. 4.3.1(d). In addition, for spectrally-narrower laser pulses, clear Rabi rotations are observed as a function of laser power as demonstrated in Fig. 4.3.1(e).

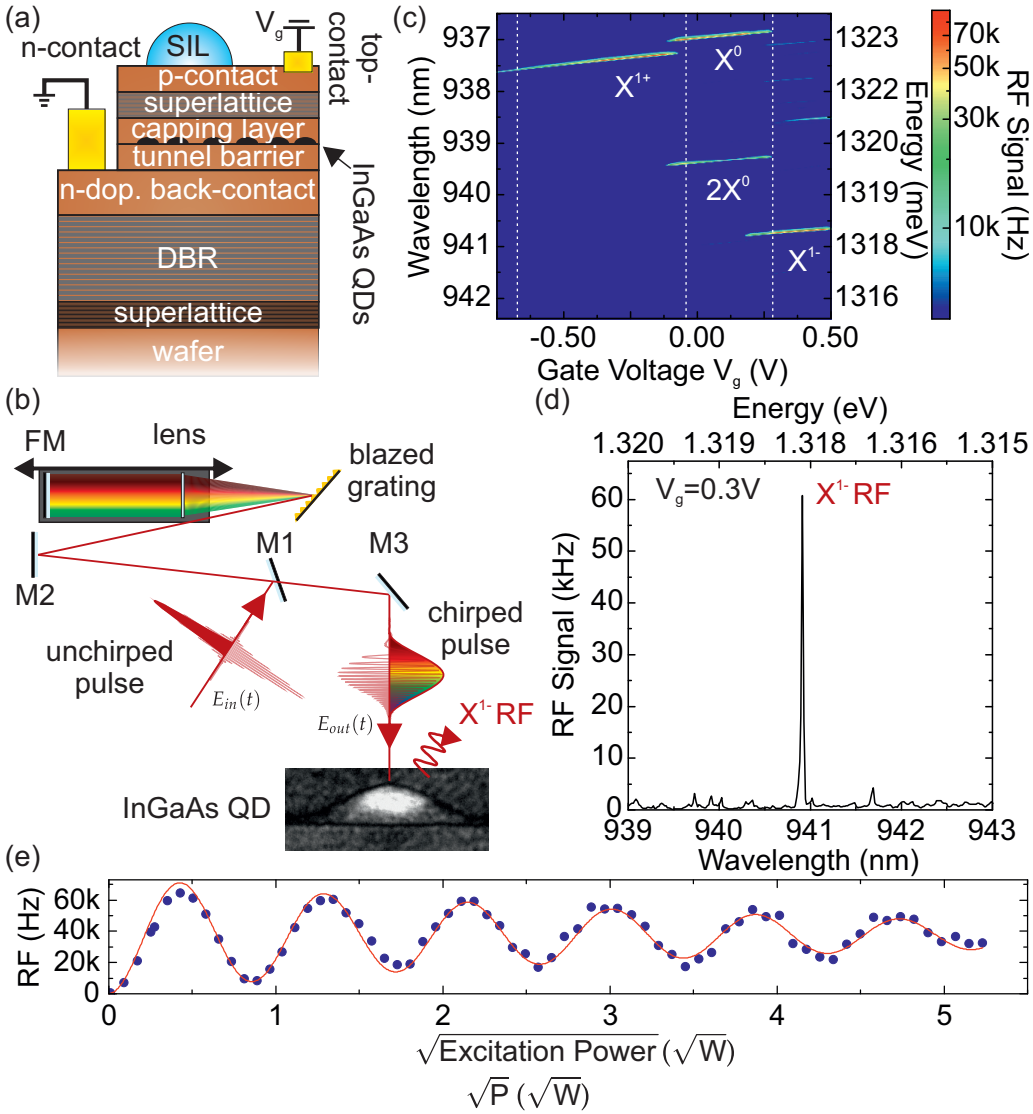

Figure 4.3.1: (a) Scheme of the n-i-p structure with an embedded layer of quantum dots (QDs). (b) Scheme of the folded $4f$ pulse-shaper to control the chirp introduced into an ultra-short, transform-limited laser pulse. The unchirped pulse is directed with mirrors (M) onto a grating, focused onto a folding mirror (FM) and back-reflected with a slight angle overshooting M1. The chirped pulse is then sent to the microscope (not shown) and excites the QD which emits an RF photon. (c) Response of the QD to broadband excitation as a function of V_g. A clear Coulomb blockade is observed. The excitonic transitions are identified. The excitation pulses had a linear polarization, a positive chirp and the center-wavelength was at 938.22 nm. (d) Detected resonance fluorescence (RF) signal after broadband excitation as a function of the detection wavelength. The peak arises from emission from the $|\mathrm{X}^{1-}\rangle \rightarrow |\mathrm{e}^{1-}\rangle$ transition. The gate voltage was $V_g = 0.3\,\mathrm{V}$ at which a single electron resides in the QD. (e) Rabi rotations driven on the $|\mathrm{X}^{1-}\rangle \leftrightarrow |\mathrm{e}^{1-}\rangle$ transition with a 2 ps long, transform-limited pulse. Blue points show the detected RF signal, red curve is a damped sine fit to the data.

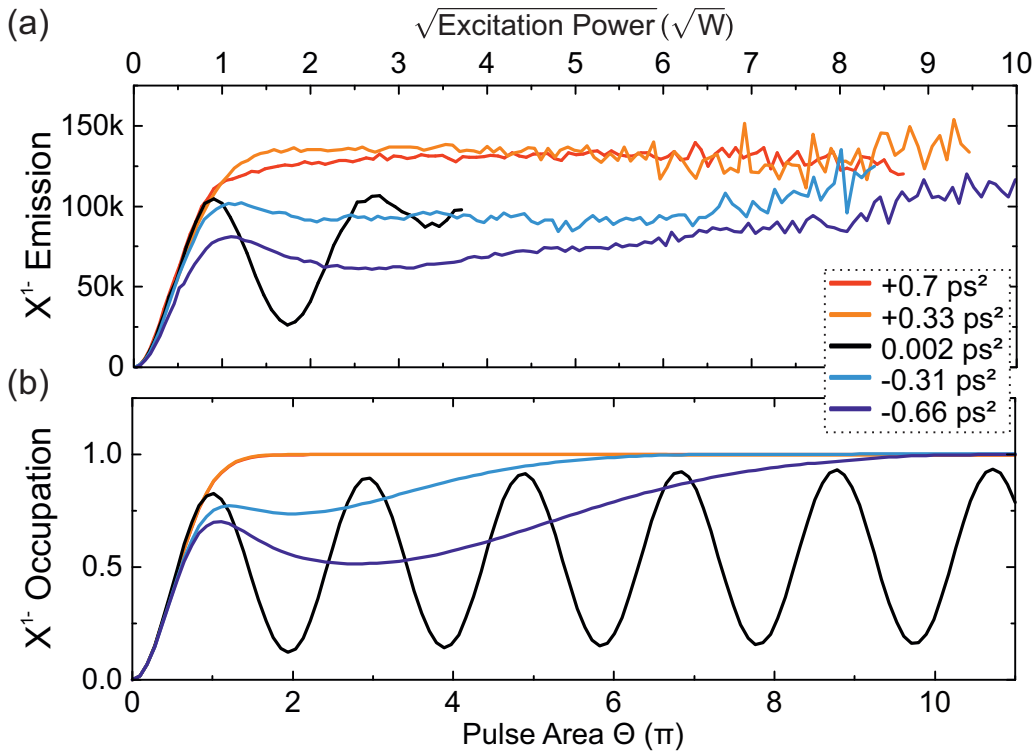

Figure 4.4.1: (a) Experimentally measured X^{1-} emission as a function of the square-root of the excitation power, and (b) calculated occupation of the $|X^{1-}\rangle$ as a function of pulse area for different chirp parameters as indicated.

To calculate the occupation of the trion state, we use the density matrix formalism for a two-level system. We take into account the standard pure dephasing-type coupling to LA phonons via the deformation potential coupling. The dispersion of the LA phonons is assumed to be linear with $\omega_{\mathbf{q}} = c_s|\mathbf{q}|$, with c_s the speed of sound and $\mathbf{q}$ the wave vector. Details on the Hamiltonian and the coupling matrix elements are given in the SI (Section 4.5.2). The QDs are known to be lens-shaped with a stronger confinement of the hole than of the electron. We describe this in the calculation with localization lengths for the electron (hole) in the growth direction, $a_{e/h,z}$, and larger localization lengths in the (x, y)-plane, $a_{e/h,r}$, taking parameters known from other experiments on QDs of this type (Section 4.5.2). Specifically, we take GaAs parameters (see SI Section 4.5.2) with $a_{e,z} = 1.5$ nm, $a_{e,r} = 5.7$ nm and $a_{h,z}/a_{e,z} = a_{h,r}/a_{e,r} = 0.77$. From the Hamiltonian (Section 4.5.2) we set up the equations of motion for the phonon-assisted density matrices, truncate the infinite hierarchy of equations using a fourth order correlation expansion, and then perform a numerical integration [Lüker et al., 2012; Reiter et al., 2014; Krügel et al., 2006]. This method is well established and has been shown to produce very reliable results [Lüker et al., 2012; Reiter et al., 2014].

4.4 Results

Fig. 4.4.1(a) shows the total X^{1-} RF signal as a function of the square-root of the excitation power for different chirp values. A Rabi rotation is observed for the smallest chirp: this data set is important to establish the power which corresponds to a pulse area of π. At much higher chirps we enter the RAP regime. We concentrate first on the positive chirps. For both values, $0.7\,\mathrm{ps}^2$ (red curve) and $0.33\,\mathrm{ps}^2$ (orange curve), the signal starts with a fast rise, saturates and stays nearly constant over the whole excitation power range at a count-rate of 125 kHz. It is possible to reach pulse areas of up to 11π on account of the excellent discrimination between reflected laser light and RF signal. This experimental data with positive chirp reflects RAP of a two-level system

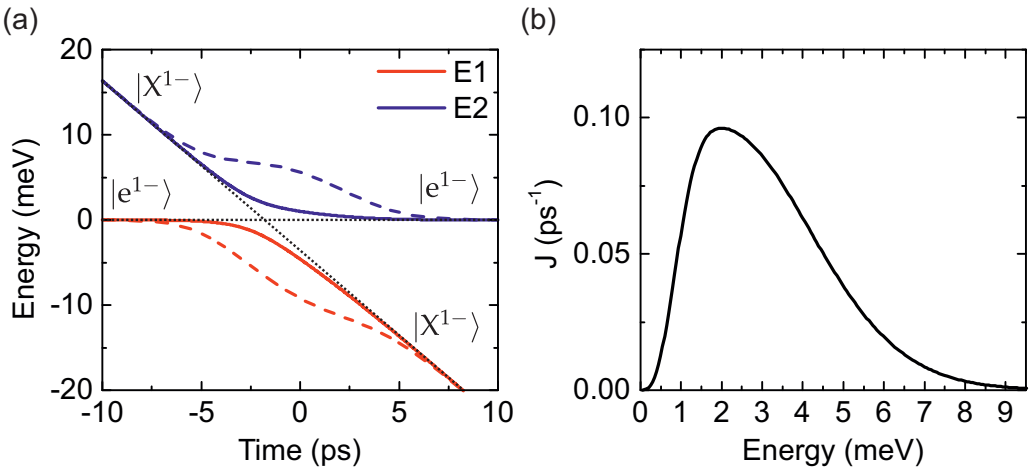

Figure 4.4.2: (a) Time evolution of the instantaneous eigenenergies of the coupled electronic-light system for a chirp of $\alpha = 0.3$ ps^2 and a pulse area $\Theta = 3\pi$ (solid lines) and $\Theta = 10\pi$ (dashed lines). The black dashed lines indicate the uncoupled energies. (b) Plot of the phonon spectral density.

as described by the detuning dependence of the eigenenergies of the dressed states, Fig. 4.4.2(a). Starting in the ground state $|e^{1-}\rangle$, the system evolves along the lower (red) branch and follows the avoided crossing induced by the interaction with the light field provided the pulse area is above the threshold for RAP. After the pulse, the system ends up in the excited state $|X^{1-}\rangle$.

The signal measured with negative chirp, Fig. 4.4.1(a), shows a quite different course. Initially, the signal rises, reaching 75% or 60% of saturation for a chirp coefficient α of $-0.31\,\text{ps}^2$ (cyan curve) or $-0.66\,\text{ps}^2$ (blue curve), respectively. Subsequently, the signal decays into a broad minimum, followed by a rise at much higher excitation powers of around $7\,\sqrt{\mu\text{W}}$. At the highest excitation powers, the signal even reaches the signal for a positive chirp.

We interpret these features as a consequence of the electron-phonon interaction. Phonons can interrupt the adiabatic transfer by causing a jump from one branch to the other one in Fig. 4.4.2(a) [Lüker et al., 2012]. For positive chirp, a phonon can be absorbed taking the system from the lower branch to the upper branch. However, at $T = 4.2\,\text{K}$, phonons with the required frequency for the transition between the two branches are largely frozen out and the probability for absorption is therefore small. Hence the process with positive chirp is barely influenced by phonons. For negative chirp, in terms of the eigenenergies, the time axis in Fig. 4.4.2(a) is effectively reversed: the system follows the upper (blue) branch from right to left as the pulse evolves. The system can emit a phonon and jump from the upper to the lower branch. This yields an asymmetry of the RAP with respect to the sign of the chirp [Lüker et al., 2012; Mathew et al., 2014; Glässl et al., 2013]. However, the recovery of the RAP signal in the case of negative chirp and large pulse areas suggests that phonon emission, strong for intermediate pulse areas, is suppressed.

The interpretation of the experimental RAP data in terms of phonon scattering is confirmed by theoretical calculations shown in Fig. 4.4.1(b). The theoretical results show close-to-ideal RAP for positive chirp, while for negative chirp a reduced RAP fidelity at intermediate pulse areas and a recovery of the RAP at the highest pulse areas, exactly as in the experiment, is obtained. The detailed correspondence with the experimental data shows that phonon scattering is the major factor in the experiment, and in particular, the claim that phonon scattering is suppressed at the highest pulse areas is given strong support by the theory.

In contrast to previous studies [Simon et al., 2011; Wu et al., 2011; Lüker et al., 2012; Glässl et al., 2013], for our pulse parameters, the phonons are most efficient at rather low pulse areas. This experimental result is in excellent agreement with the theoretical predictions in Fig. 4.4.1(b), which also show a minimum trion population at low pulse areas (around $\sim 2\pi$ for $\alpha = -0.31$ ps^2; around 3π for $\alpha = -0.66$ ps^2). This brings the reappearance regime within reach, achieved here

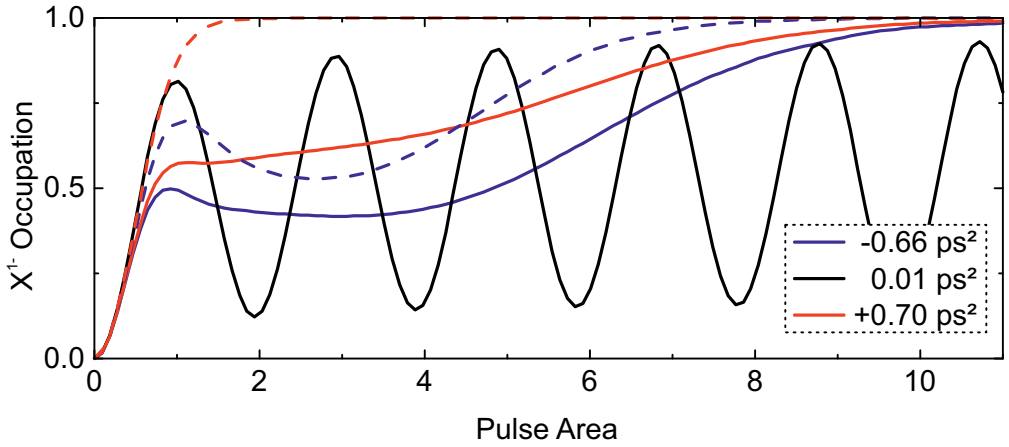

Figure 4.4.3: Calculation of the $|X^{1-}\rangle$ occupation for a temperature of $T = 100$ K (solid lines) as function of pulse area for different chirps as indicated. As a comparison the curves obtained by calculations for $T = 4$ K are displayed as dashed lines.

above pulse areas of $\sim 8\pi$.

To interpret our observations on the electron-phonon interaction, we consider the spectral density of the phonons as shown in Fig. 4.4.2(b). The phonon spectral density $J(\omega)$, a measure of the coupling strength between the electron and phonon system at a given frequency ω [Reiter et al., 2014; Wigger et al., 2014; Machnikowski and Jacak, 2004], is defined as $J(\omega) = \sum_{\mathbf{q}} |g_{\mathbf{q}}|^2 \delta(\omega - \omega_{\mathbf{q}})$ with $g_{\mathbf{q}}$ the exciton-phonon coupling matrix element (see SI, Section 4.5.2). The non-monotonic behavior found in Fig. 4.4.2(b) results from a combination of the momentum dependence of the bulk coupling matrix element, which results in a cubic rise of the spectral density, and the influence of the envelope wave functions of electron and hole, which decouple phonons with wavelengths much smaller than the QD size. The net result is that the phonon spectral density has a broad maximum at phonon energies around $2 - 3$ meV. Coming back to the dressed states shown in Fig. 4.4.2(a), the phonon emission rate from the upper to the lower branch is proportional to the spectral density at the given energy separation. On examining the dressed state energies we see that for a small pulse area of $\Theta = 3\pi$ (solid lines), the splitting between the states is of the order of a few meV and hence the phonons are effective. However, for a larger pulse area of 10π (dashed lines), the splitting between the states is always above 7 meV, and in this regime the phonon spectral density is almost zero. Accordingly, the phonons do not affect the RAP for high pulse areas. Indeed, the decoupling from the phonons seen in the theoretical curves above 8π is also observed in the experimental data, where the signals for positive and negative chirps merge.

Let us briefly compare our findings with the reappearance phenomena for Rabi rotations [Vagov et al., 2007]. For Rabi rotations, the reappearance only occurs at extremely high pulse areas for typically used pulses. The reason is that for resonant excitation, the dressed states are degenerate before and after the pulse and they split in the presence of the pulse. Therefore, even in the case of very high pulse areas, the dressed state energy splitting matches the energy at which the phonon spectral density has its maximum in the leading and the trailing edges of the pulse. This explains why the reappearance is more pronounced for hypothetical rectangular pulses [Glässl et al., 2011] than for the smooth pulses used exerimentally. The reappearance of Rabi rotations has not been clearly observed to date. In contrast, in RAP the dressed states are strongly separated before and after the pulse and, for high pulse areas, never enter the region of efficient phonon coupling. This allows us to enter a reappearance regime for RAP.

Finally, by extending our calculations to higher temperatures we estimate how our preparation scheme is affected by elevated temperatures. At higher temperatures, phonons can be both absorbed and emitted. For RAP, this weakens the asymmetry of the phonon influence regarding the sign of the chirp. At $T = 100$ K, phonon scattering limits the exciton population to about 0.55 for

parameters used in previous studies [Lüker et al., 2012]. Also for the Rabi rotations, a stronger dephasing with increasing temperature has been found experimentally [Ramsay et al., 2010b]. In the phonon-assisted state preparation scheme [Quilter et al., 2015], elevated temperatures are also detrimental for the high fidelity preparation. We show the effect of temperature on using the spectrally broad pulses in Fig. 4.4.3, where we calculated the occupation of the excited state at a temperature of $T = 100$ K. The dashed lines indicate the curves at $T = 4$ K. For the Rabi rotations, we see no influence of the temperature, which is due to the short pulse length τ_0 of less than 100 fs. For the excitation with positive chirp, the influence of phonons is clearly visible. Instead of immediately rising to an occupation of one, the occupation now goes up to about 0.5 and then increases gradually. Here, phonon absorption hinders the RAP process by inducing transitions from the lower to the upper branch. However, at high pulse areas above about 8π, we find that the occupation rises to one such that even at this elevated temperature the electron-phonon scattering is inefficient. The influence of temperature on the exciton occupation in the case of negative chirp is similar. While the damping of the exciton occupation for intermediate pulse areas is increased with respect to 4 K, for higher pulse areas also for negative chirps the occupation goes back to one. Hence, by entering the reappearance regime, we can achieve a state preparation scheme robust not only against fluctuations in excitation parameters such as chirp coefficient, detuning and pulse area, but also robust against elevated temperatures.

In conclusion, we have studied the influence of phonons on the RAP in the optical domain on a single quantum dot. By performing RAP with highly chirped, spectrally broad laser pulses combined with resonance fluorescence detection together with a full microscopic calculation, we showed that we were able to enter the reappearance regime in which exciton state preparation is minimally influenced by phonon scattering. The work predicts that state preparation in the reappearance regime is almost unaffected by elevated temperatures, a notable feature with respect to other preparation protocols where elevated temperatures lead to a lower fidelity. Our work opens up a new regime for coherent control of excitons in semiconductors with minimal influence from the phonons.

4.5 Supplementary Information

4.5.1 Methods

The quantum dot sample

We study in this work single self-assembled InGaAs quantum dots (QDs) embedded in a GaAs heterostructure, a diode grown by molecular beam epitaxy. The diode is formed by an n-i-p structure Prechtel et al. [2016], Fig. 4.5.1(a), where the top- and back-gates are epitaxial layers of GaAs doped with carbon and silicon, respectively. The n-i-p diode includes also a distributed Bragg reflector (DBR) which increases the photon collection efficiency. The complete layer sequence is given in Tab. 4.5.1.

The main advantage of the n-i-p diode over an n-i-Schottky diode is an enhanced photon collection by roughly one order of magnitude. On the one hand, this is achieved by the DBR which reflects downward emitted photons towards the objective. On the other hand, the absorption of photons in the top-gate is reduced by using an epitaxial gate instead of a metal gate.

The final layer of 44 nm undoped GaAs places the p-doped layer, the top-gate, around a node-position of the standing electromagnetic wave in the n-i-p diode. The n- and p-doped layers are contacted independently. Selective etching of the capping allows the buried p-layer to be contacted. Access to the n-layer is ensured by wet etching a mesa structure.

To increase the collection efficiency further we placed a zirconia (ZrO_2) hemispherical solid-immersion lens (SIL) on the semiconductor surface. The SIL has a refractive index of $n = 2.13$ at 940 nm.

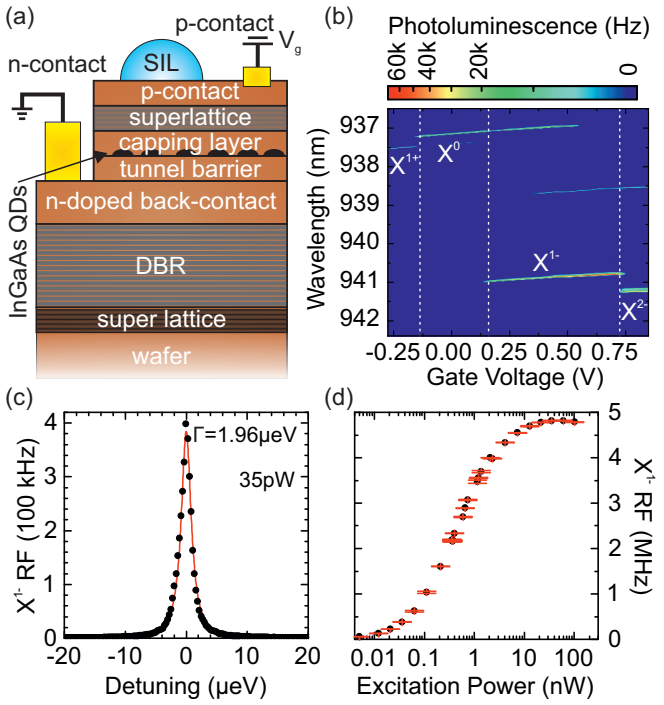

Figure 4.5.1: **Resonance fluorescence (RF) spectroscopy on a quantum dot (QD) with narrowband continuous wave excitation. (a)** the n-i-p layer structure. **(b)** Non-resonant photoluminescence of the QD as a function of the gate voltage V_g. **(c)** Narrowband, resonant excitation performance of the QD. An example spectrum showing the RF signal as function of laser detuning at an excitation power of 35 pW. A Lorentzian fit (red solid line) to the black data points shows a FWHM of 1.96 μeV. **(d)** RF signal with resonant continuous wave excitation as a function of the excitation power.

In the experiment the n-contact is grounded and a gate voltage V_g is applied to the p-contact. The gate voltage allows control over the charge: single electrons can be loaded into the QD; furthermore, excitonic resonances can be shifted by the DC Stark effect Warburton et al. [2000]; Dalgarno et al. [2008]; Warburton [2013]. Fig. 4.5.1(b) shows the photoluminescence from a single QD following non-resonant excitation at 830 nm (excitation into the wetting layer). Several charging plateaus are clearly visible in the photoluminescence. They correspond to optical transitions from an excited state to a ground state with different charge: $|X^{1+}\rangle \rightarrow |h^{1+}\rangle$, $|X^0\rangle \rightarrow |0\rangle$, $|X^{1-}\rangle \rightarrow |e^{1-}\rangle$ and $|X^{2-}\rangle \rightarrow |e^{2-}\rangle$, with $|h^{1+}\rangle$ and $|e^{1-}\rangle$ representing a single hole and single electron, respectively. The DC Stark shift is from red to blue with increasing V_g and can be seen clearly. We note that the X^0 plateau overlaps with the X^{1-} plateau only with non-resonant excitation. We attribute this overlap to the occasional decay of the $|X^{1-}\rangle$ via an Auger process Kurzmann et al. [2016].

Resonance fluorescence with continuous wave excitation

In resonance fluorescence (RF) spectroscopy we investigate the QD characteristics with a narrow band (linewidth in sub pm range) excitation laser. The scattering induced by resonant excitation is detected. Back-reflected laser light is suppressed with a dark-field technique leading to an extinction of 10^7:1 Kuhlmann et al. [2013b,a]. A typical X^{1-} spectrum from the QD at low excitation power is depicted in Fig. 4.5.1(c). The linewidth, measured here slowly, is around 2 μeV well below saturation, approximately 2.5 times larger than the transform limit Kuhlmann et al. [2013b]. A signal to background ratio of more than 1,000: is achieved with linearly polarized excitation. With increasing excitation power the linewidth broadens (power broadening) and the RF signal increases reaching a saturation count-rate of 5 MHz, Fig. 4.5.1(d). This signal is about 10 times more than from QDs in typical n-i-Schottky samples Kuhlmann et al. [2013b]. The signal is measured with

a single photon avalanche photodiode (SPAD) with an efficiency of 20% at these wavelengths. Throughout, the stated count-rates are the bare count rates and are not corrected for instance for the poor SPAD quantum efficiency. The photon extraction efficiency from single QDs in the n-i-p device is around 10%, a success resulting from several improvements in the sample design as discussed above: the n-i-p type features a DBR and a transparent epitaxial gate.

Function	Material	Thickness
wafer	GaAs	
buffer	GaAs	50 nm
superlattice, 18 periods	GaAs, AlAs	72 nm
DBR, 16 periods	GaAs, AlAs	2400 nm
spacer	GaAs	57.3 nm
electron reservoir, back contact	GaAs:Si	50 nm
tunnel barrier	GaAs	30 nm
InGaAs QDs	InAs	∼1.6 ML
capping layer	GaAs	153 nm
blocking barrier, 46 periods	AlAs, GaAs	184 nm
p-doped top contact	GaAs:Si	30.5 nm
undoped spacer	GaAs	1 nm
etch stop	AlAs	2 nm
top capping layer	GaAs	44 nm

Table 4.5.1: Layers of the n-i-p diode. QDs are formed by depositing 1.6 monolayers (ML) of InAs. The distributed Bragg reflector (DBR) increases the photon extraction efficiency.

Resonance fluorescence with pulsed excitation

With pulsed excitation, we use the full spectrum of 130 fs transform-limited "ultra-fast" pulses, again exciting the QD resonantly. The spectral full-width-at-half-maximum (FWHM) of the pulse is $\Delta\lambda = 10\,\text{nm}$. With this bandwidth we address the ground state transition for the particular charge state set by the gate voltage (but not higher energy transitions). The RF response of the QD is detected with a grating spectrometer.

A scheme of the complete set-up is shown in Fig. 4.5.2. The ultra-fast pulses from a mode-locked femtosecond laser are expanded and sent into a compact pulse-shaper. The pulse-shaper retains all the spectral components and controls the amount of chirp as described below. From here the pulses pass through power control and polarization optics and are then coupled into a single mode optical fiber. The fiber transports the pulses to a confocal microscope. In the microscope, the excitation pulses pass through a linear polarizer, two beam-splitters and are sent to the objective at cryogenic temperature (4.2 K). The objective, an aspherical lens with a numerical aperture of 0.68, focuses the light onto the sample. The sample is held on a stack of piezo-steppers which allows a particular QD to be placed within the focal spot of the microscope. This process is aided by the in situ diagnostics provided by a camera image of the focus. Light scattered by the QD is collected and coupled into the detection fiber. The back-reflected laser light is suppressed by a second linear polarizer whose axis is orthogonal to the axis of the polarizer in the excitation stage. The RF signal is detected directly with a SPAD (continuous wave excitation) or with a spectrometer-CCD camera (pulsed excitation).

Detecting RF with pulsed excitation also depends on suppressing the reflected laser light with the polarization-based dark-field technique. However, owing to the wavelength dependence of the polarization optics, the laser suppression of a broadband pulsed laser is less effective than with the narrowband continuous wave laser: we reach an extinction ratio of typically 10^5:1 with broadband excitation. We use in addition the spectral mismatch between the broadband laser and

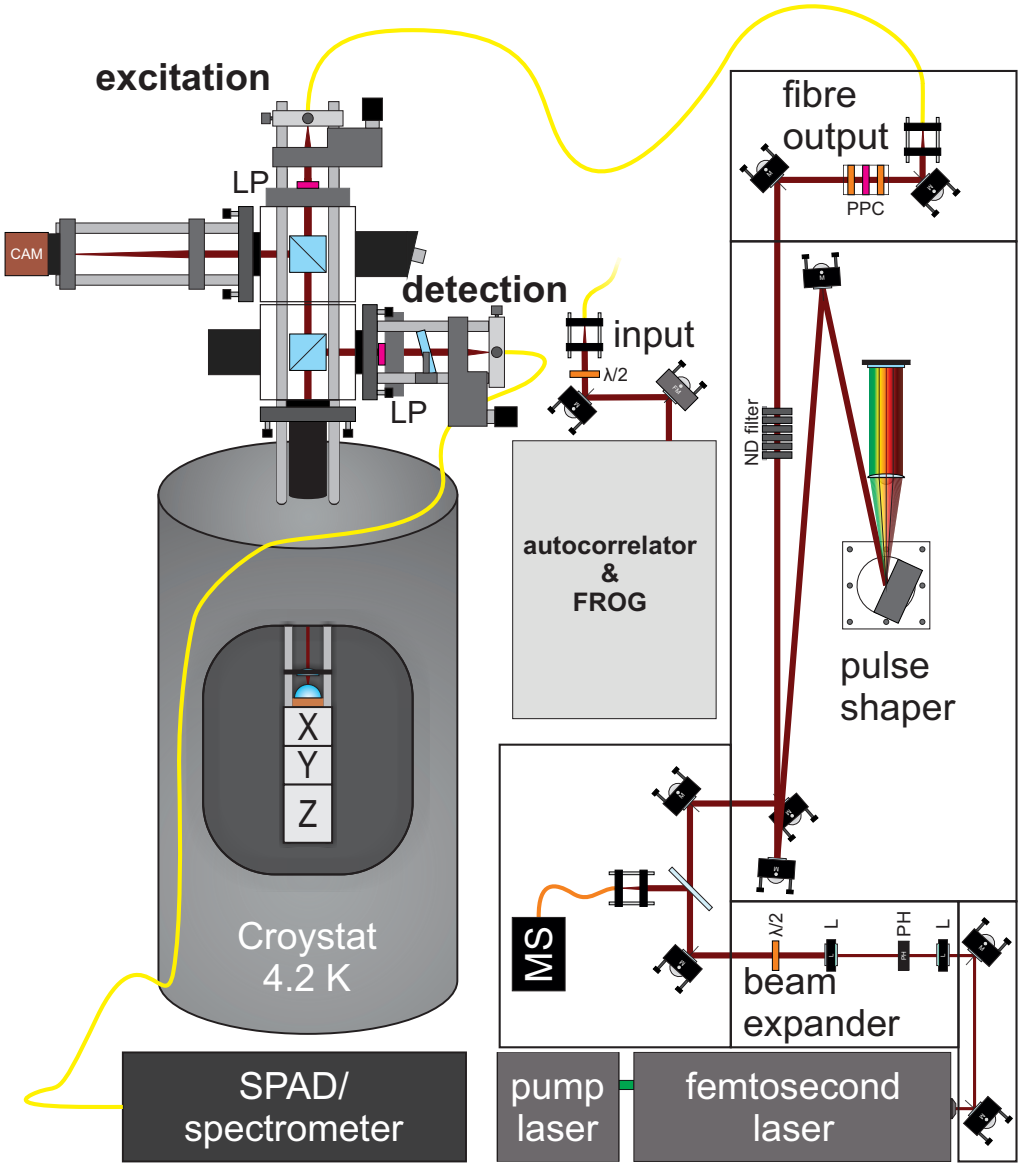

Figure 4.5.2: **Scheme of the complete set-up.** Ultra-short pulses were manipulated in a pulse-shaper, coupled into a single mode glass fiber and sent to a confocal microscope mounted on a bath cryostat. The pulses were characterized with a combination of autocorrelator and frequency-resolved-gating (FROG). The sample is held at a temperature of 4.2 K in the bath croystat on an xyz-positioner. A mini spectrometer (MS) measures the spectral profile of the pulses.

the narrowband RF to increase the extinction ratio, Fig. 4.5.3. The laser background falling on the CCD camera does not depend on the gate voltage, Fig. 4.5.3(a), such that we can use the gate voltage dependence of the QD emission to construct the laser background spectrum. The resulting residual laser background is shown in Fig. 4.5.3(b) in red. The spectral shape is explained by the Gaussian spectral shape of the excitation laser along with the quadratic function of laser suppression: the laser suppression is most effective at its alignment wavelength and then decays quadratically in wavelength superimposed by interference fringes. A typical spectrum measured at $V_g = -12\,\mathrm{mV}$ is shown in black. Sharp emission peaks from the exciton and biexciton appear on top of the laser background. The signal after background subtraction is shown in the lower plot in blue. Before background subtraction, the maximum signal to background ratio in a narrow spectral window around the emission line is 22:1.

The measurement of emission linewidths in RF with broadband excitation is limited by the

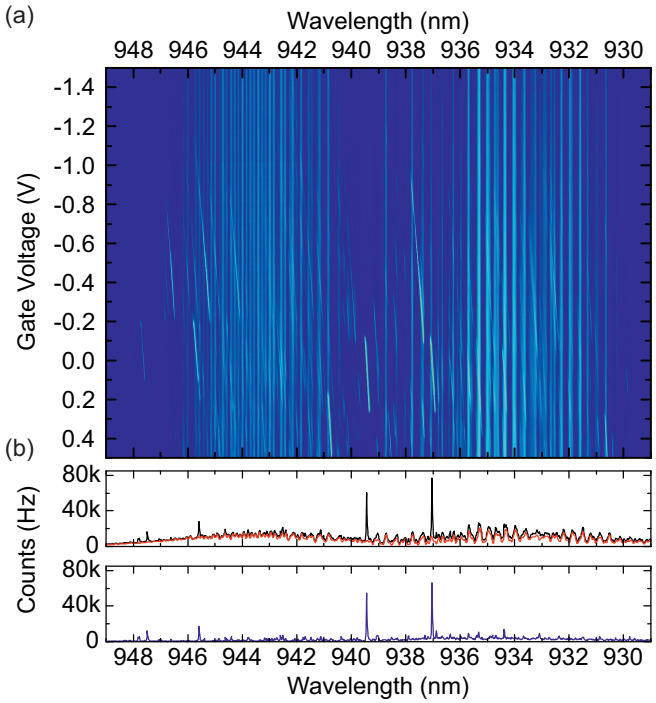

Figure 4.5.3: **Laser background subtraction in resonance fluorescence spectroscopy using broad-band, pulsed excitation. (a)** The RF signal as a function of gate voltage without background subtraction measured with an excitation power of ∼8 µW corresponding to a pulse area of around 3 π. **(b)** One spectrum from (a) at a gate voltage of −0.012 V is shown as the black curve in the upper panel. Distinct peaks from the exciton and trion are visible toegther with a broad laser background. The reconstructed laser background (from all spectra in (a)) is shown in red. The blue curve in the lower panel shows the difference between the black and the red curve, the resulting signal after background subtraction.

resolution of the spectrometer. Hence, we can only state that these linewidths are below 30 µeV, as depicted in the spectrum in Fig. 4.3.1(d) of the main paper.

Pulse shaping: introducing chirp

Chirp is introduced into the transform-limited laser pulses by a compact, folded $4f$ pulse-shaper Martinez [1987]; Weiner et al. [1992]. The scheme is depicted in Fig. 4.3.1(b) of the main paper. The unchirped pulse is diffracted by a high resolution, blazed grating (1,800 grooves per mm) and then focused by a lens onto a mirror positioned in the focal plane. From here the light travels back under a small angle with respect to the diffraction plane allowing a spatial separation of incoming and outgoing pulses. The distance between grating and lens controls the chirp Martinez [1987]. The lens and the mirror are mounted on a translation platform. Moving the platform with respect to the grating changes the chirp: if the distance matches the focal length of the lens the chirp is zero, a larger (smaller) distance leads to negative (positive) chirp. The temporal duration of the pulses exiting the laser is 130 fs (intensity FWHM); the temporal duration can be stretched up to 15 ps corresponding to a chirp in the range from $-0.7\,\mathrm{ps}^2$ to $0.7\,\mathrm{ps}^2$.

We characterized the chirp with a combination of a FROG and autocorrelator. This allows us to reveal the presence of any high-order phase terms and prevent them by an optimal adjustment of the pulse-shaper. The chirp is measured both in the free space mode and also after the optical single mode fiber in order to determine the sign of the chirp and to compensate for the chirp introduced by the fiber itself.

4.5.2 Theoretical Model

For the theoretical calculations we use the standard model of a two-level system coupled to longitudinal phonons. For clarity, we outline here the details of the model.

Hamiltonian

We can divide the Hamiltonian H of the system into four parts with

$$H = H_{\mathrm{c}} + H_{\text{c-l}} + H_{\mathrm{ph}} + H_{\text{c-ph}},$$

where H_{c} denotes the electronic structure, $H_{\text{c-l}}$ describes the carrier-light coupling and $H_{\mathrm{ph}} + H_{\text{c-ph}}$ the phonon part.

For the electronic structure we take a two-level system, which consists of the ground state $|\mathrm{e}^{1-}\rangle$ and the single exciton state $|\mathrm{X}^{1-}\rangle$ with the Hamiltonian

$$H_{\mathrm{c}} = \hbar\omega_{\mathrm{X}^{1-}} \left|\mathrm{X}^{1-}\right\rangle \left\langle\mathrm{X}^{1-}\right|,$$

where $\hbar\omega_{\mathrm{X}^{1-}}$ denotes the energy of the negative trion. The energy of the ground state has been set to zero.

The carrier-light interaction is modeled in the usual dipole and rotating wave approximation. For this two-level system we have

$$H_{\text{c-l}} = \frac{\hbar}{2}\left(\Omega(t)|\mathrm{X}^{1-}\rangle\langle\mathrm{e}^{1-}| + \Omega^*(t)|\mathrm{e}^{1-}\rangle\langle\mathrm{X}^{1-}|\right).$$

where $\hbar\Omega(t) = 2\mathbf{M}\cdot\mathbf{E}(t)$, with $\mathbf{E}(t)$ the positive frequency component of the electric field of the laser pulse; $\mathbf{M}$ denotes the dipole matrix element.

The main source of decoherence in QDs is caused by the coupling to longitudinal acoustic (LA) phonons which are treated as bulk-like due to the small acoustic mismatch between the QD area and the surrounding material Reiter et al. [2014]. The Hamiltonian of the free phonons reads

$$H_{\mathrm{ph}} = \hbar\sum_{\mathbf{q}} \omega_{\mathbf{q}} b_{\mathbf{q}}^\dagger b_{\mathbf{q}},$$

where $b_{\mathbf{q}}^\dagger$ ($b_{\mathbf{q}}$) is the creation (annihilation) operator of a phonon with wave vector $\mathbf{q}$ and frequency $\omega_{\mathbf{q}} = c_s|\mathbf{q}|$, c_s being the sound velocity.

The carrier-phonon interaction is modeled by a pure-dephasing Hamiltonian using the deformation potential coupling mechanism. The corresponding Hamiltonian is given by

$$H_{\text{c-ph}} = \hbar\sum_{\mathbf{q}} \left(g_{\mathbf{q}} b_{\mathbf{q}} + g_{\mathbf{q}}^* b_{\mathbf{q}}^\dagger\right) |\mathrm{X}^{1-}\rangle\langle\mathrm{X}^{1-}|.$$

The main coupling mechanism is the deformation potential coupling with the coupling matrix element for the electrons and holes

$$g_{\mathbf{q}}^{e/h} = \sqrt{\frac{q}{2V\rho\hbar c_s}} D_{e/h} F_{\mathbf{q}}^{e/h},$$

where V is the normalization volume, ρ the mass density of the crystal, and $D_{e/h}$ the deformation potential coupling constant for electrons/holes. As parameters we take the standard GaAs parameter listed in Tab. 4.5.2. The exciton coupling matrix element is obtained by $g_{\mathbf{q}} = g_{\mathbf{q}}^e - g_{\mathbf{q}}^h$.

The form factor $F_{\mathbf{q}}^{e/h}$ accounts for the bound states of the QD and, thus, for the geometry of the QD. We assume a harmonic confinement potential in a lens-shaped QD yielding the form factor

$$F_{\mathbf{q}}^{e/h} = \exp\left[-\frac{1}{4}\left(q_z^2 a_{e/h,z}^2 + q_r^2 a_{e/h,r}^2\right)\right].$$

Parameter		Value
density	ρ	$5370\,\mathrm{kg/m^3}$
sound velocity	c_s	$5.1\,\mathrm{nm/ps}$
electron deformation potential constant	D_e	7 eV
hole deformation potential constant	D_h	−3.5 eV

Table 4.5.2: Material parameters used in the calculation.

q_z is the wave vector in the z-direction; q_r is the in-plane wave vector. $a_{e/h,z}$ and $a_{e/h,r}$ are the electron/hole localization lengths in the z-direction and in the (x, y)-plane direction, respectively. We used $a_{e,z} = 1.5$ nm and $a_{e,z} = 5.7$ nm, thereby modelling a flat QD. The ratio between electron and hole localization lengths is taken to be $a_h/a_e = 0.77$ for both directions Warburton et al. [2002].

Using this Hamiltonian we set up the equations of motion in the density matrix formalism which leads to an infinite hierarchy of phonon-assisted variables. We truncate this hierarchy using a fourth-order correlation expansion, which yields reliable results for the carrier-dynamics in a QD Reiter et al. [2014]; Lüker et al. [2012]; Glässl et al. [2011]. The equations of motion of the two-level model can be found, e.g., in Ref. Krügel et al. [2006].

5 Geometric Biexciton Generation

Adapted from:
"**Coherent and robust high-fidelity generation of a biexciton in a quantum dot by rapid adiabatic passage**"

Timo Kaldewey[1], Sebastian Lüker[2], Andreas V. Kuhlmann[1,3], Sascha R. Valentin[4], Arne Ludwig[4], Andreas D. Wieck[4], Doris E. Reiter[2], Tilmann Kuhn[2], and Richard J. Warburton[1]

[1]Department of Physics, University of Basel, Klingelbergstrasse 82,
CH-4056 Basel, Switzerland

[2]Institut für Festkörpertheorie, Universität Münster, Wilhelm-Klemm-Strasse 10,
D-48149 Münster, Germany

[3]IBM Research-Zurich, Säumerstrasse 4,
CH-8803 Rüschlikon, Switzerland

[4]Lehrstuhl für Angewandte Festkörperphysik, Ruhr-Universität Bochum,
D-44780 Bochum, Germany

Submitted to: *Physical Review Letters*, November 2016

5.1 Abstract

A biexciton in a semiconductor quantum dot is a source of polarization-entangled photons with high potential for implementation in scalable systems. Several approaches for non-resonant, resonant and quasi-resonant biexciton preparation exist, but all have their own disadvantages, for instance low fidelity, timing jitter, incoherence or sensitivity to experimental parameters. We demonstrate a coherent and robust technique to generate a biexciton in an InGaAs quantum dot with a fidelity close to one. The main concept is the application of rapid adiabatic passage to the ground state-exciton-biexciton system. We reinforce our experimental results with simulations which include a microscopic coupling to phonons.

5.2 Introduction

Entangled photon pairs are a powerful resource, especially for quantum teleportation and quantum key distribution protocols. Spontaneous parametric down-conversion in non-linear optics is a source of entangled photon pairs [Kwiat et al., 1995], but success is not guaranteed – the emission is a probabilistic process – and the error rate is high. In contrast, semiconductor quantum dots (QDs) are bright, on-demand sources of both single photons [He et al., 2013] and entangled photon pairs and hence have enormous potential in quantum computing and quantum cryptography [Gisin et al., 2002].

A biexciton in a QD is the starting point for a two photon cascade: when perfectly prepared, biexciton decay leads to the subsequent emission of two photons, Fig. 5.2.1(f). In a QD without a

significant fine structure splitting (FSS), the two photons are polarization-entangled [Müller et al., 2014]. The majority of InGaAs QDs show a FSS due to a reduced symmetry [Gammon et al., 1996; Li et al., 2000a; Juska et al., 2013]. However, sophisticated techniques were developed to compensate for the FSS with strain [Trotta et al., 2014], electric [Kowalik et al., 2005] or magnetic fields [Bayer et al., 2002; Stevenson et al., 2006] and with special growth conditions [Juska et al., 2013].

Several approaches for biexciton preparation have been proposed [Glässl et al., 2013; Debnath et al., 2013; Gawarecki et al., 2012; Hui and Liu, 2008] and demonstrated [Brunner et al., 1994; Stufler et al., 2006b; Jayakumar et al., 2013; Müller et al., 2014; Gotoh et al., 2013; Bounouar et al., 2015]. Resonant two-photon schemes involving Rabi rotations [Stufler et al., 2006b; Jayakumar et al., 2013; Müller et al., 2014] are sensitive to fluctuations in both laser power and QD optical frequency. They are likely to suffer from an imperfect biexciton preparation resulting in undesired exciton photons unrelated to the cascade process. A more robust scheme using phonon-assisted excitation was reported by several groups recently [Ardelt et al., 2014; Gotoh et al., 2013; Quilter et al., 2015; Bounouar et al., 2015; Jayakumar et al., 2013]. An impressively high biexciton occupation of up to 95% was demonstrated using this quasi-resonant scheme [Bounouar et al., 2015]. But the strength here is also a weakness. The scheme relies on the coupling to the phonon bath in the semiconductor environment: it is an inherently incoherent process.

We present here a coherent technique to create a biexciton with high probability, low jitter and weak dependence on the excitation and system parameters. The technique is based on rapid adiabatic passage (RAP). RAP allows the robust creation of an exciton [Simon et al., 2011; Wu et al., 2011; Mathew et al., 2014] via a process requiring two-levels. RAP is applied here to the ground state-exciton-biexciton system, $|0\rangle - |\mathrm{X}^0\rangle - |2\mathrm{X}^0\rangle$, a three-level system [Hui and Liu, 2008; Glässl et al., 2013], and allows biexciton creation without significant exciton creation. In the implementation, we use the full bandwidth of ultra-short 130 fs pulses allowing us to access spectrally both the ground state-exciton and exciton-biexction transitions within one laser pulse. We describe this process theoretically and demonstrate excellent agreement with the experimental results. Moreover, we analyze the influence of phonons on the preparation protocol. For RAP-based exciton creation, the influence of phonons depends sensitively on the sign of the chirp [Lüker et al., 2012; Mathew et al., 2014; Glässl et al., 2011]. We find also in RAP-based biexciton creation that we can choose the chirp such that the phonons are unimportant at low temperature.

5.3 Methods

We study self-assembled InGaAs QDs at a temperature of 4.2 K. The QDs are grown by molecular beam epitaxy and embedded in an n-i-p or n-i-Schottky structure, Fig. 5.2.1(a) (with more details in the supplementary information (SI), Section 5.5.1). The bias voltage allows control over the QD charge via Coulomb blockade; and within a charging plateau, control over the optical resonance frequency via the DC Stark shift, Fig. 5.2.1(d). The biexciton binding energy is positive and in the order of a few meV, a typical feature for InGaAs QDs. On driving the optical resonance with a narrowband continuous wave laser and detecting the resonance fluorescence (RF), we find that QDs in both samples have linewidths below 2 µeV, Fig. 5.2.1(c), close to the transform limit [Kuhlmann et al., 2013b]. Above saturation on a QD in the n-i-p sample, Fig. 5.2.1(a), we detect a RF single photon count-rate of 5 MHz, Fig. 5.2.1(b). In the RAP experiments, we excite single QDs with the full bandwidth of 130 fs pulses with a center wavelength of around 940 nm and linear polarization. The spectral full-width-at-half-maximum (FWHM) of the pulses is $\Delta\lambda = 10$ nm. This allows us to address the exciton and biexciton optical transitions (but not the transitions involving higher shells in the QD) with just one laser pulse. The transform-limited pulses (repetition rate of 76 MHz) from a passively mode-locked laser were manipulated in a folded $4f$ pulse-shaper [Martinez, 1987], Fig. 5.2.1(e), in order to introduce chirp (Section 5.5.1). We control precisely the sign and magnitude of the chirp (Section 5.5.1). The FWHM of the pulse duration in intensity is stretched up to

$\Delta t = 15\,\mathrm{ps}$ covering chirp coefficients up to $|\alpha| = 0.70\,\mathrm{ps}^2$ For more details about the set-up, we refer to the SI (Section 5.5.1).

For s-shell excitations, the QD system can be described by four states, namely the ground state $|0\rangle$, the two bright exciton states $|\mathrm{X}^0_{H/V}\rangle$ and the biexciton $|2\mathrm{X}^0\rangle$, Fig. 5.4.1(a). Considering only one linear polarization, H or V, and assuming that the laser pulses are much faster than the fine structure-induced quantum beat, a three-level system with only one exciton state, $|\mathrm{X}^0\rangle$, is sufficient. The exciton and biexciton state are coupled to longitudinal acoustic (LA) phonons in the pure dephasing regime via the deformation potential (Section 5.5.2). We use standard GaAs parameters and take the excitation parameters from the experiment leaving the QD size as the only fitting parameter. This model has been successfully used to describe the phonon influence on Rabi rotations [Reiter et al., 2014] and on the population inversion via RAP [Lüker et al., 2012; Glässl et al., 2013]. For the occupations of the exciton and biexciton states as well as for the coherences between all involved states a set of equations of motion is derived within a well-established fourth-order correlation expansion method [Krügel et al., 2005]. The equations are then solved numerically.

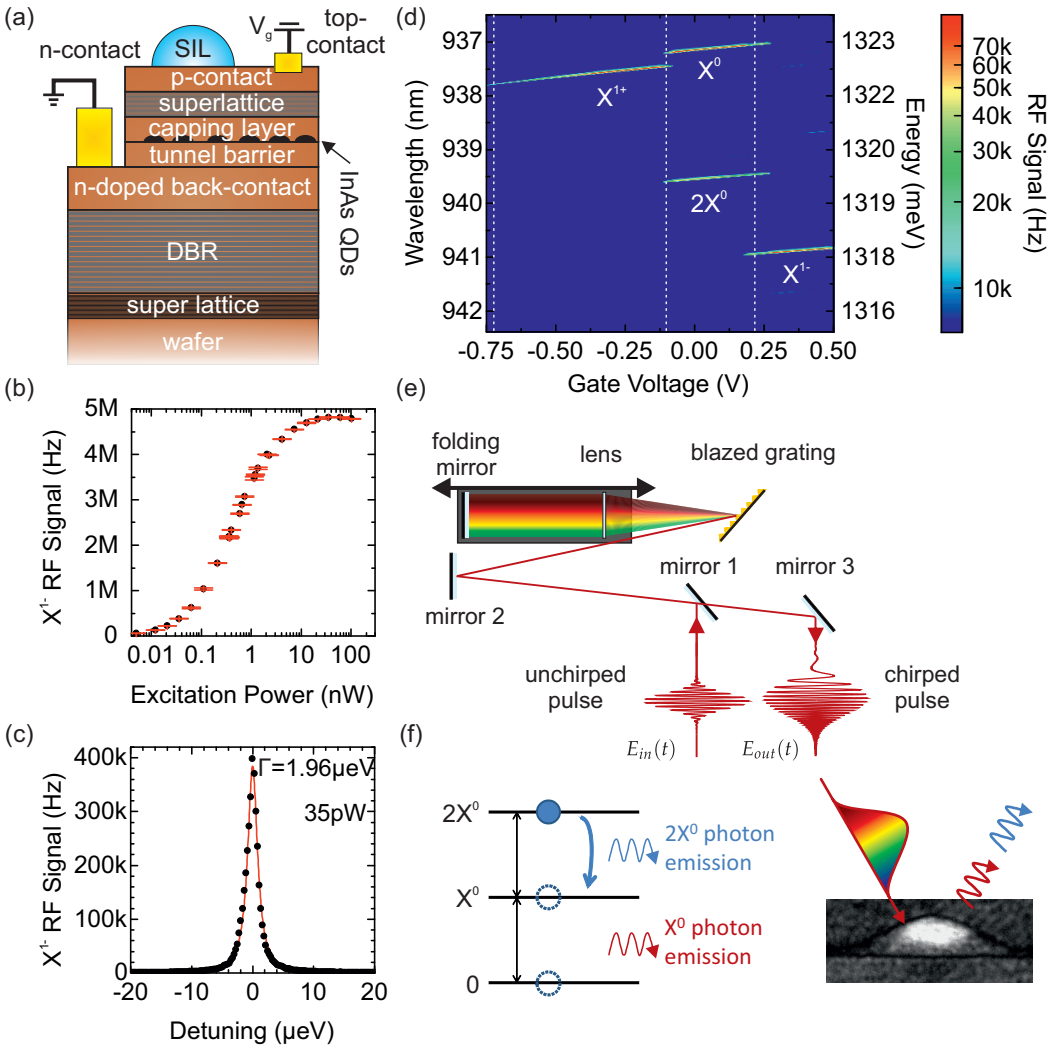

Figure 5.2.1: **Resonance fluorescence (RF) on a single quantum dot excited with a narrowband continuous wave laser and with broadband laser pulses. (a)** Structure of the n-i-p diode with epitaxial gate. **(b)-(c)** RF with narrowband excitation. **(b)** X^{1-} RF signal versus excitation power. **(c)** RF versus laser detuning at an excitation power of 35 pW (points). A Lorentzian fit (red solid line) determined the FWHM linewidth, 1.96 μeV. **(d)** RF with broadband pulsed excitation as a function of gate voltage. The laser polarization was linear, the chirp positive and the center frequency resonant with the neutral exciton X^0. **(e)** Scheme of a folded $4f$ pulse-shaper controlling the chirp introduced into an ultra-short, transform-limited laser pulse. **(f)** Generation of a biexciton with broadband, chirped excitation. Scheme of the two-photon cascade (left) after chirped excitation of a QD (right).

5.4 Results

The goal of our work is high fidelity biexciton generation using RAP. Ideally, a vanishing intermediate occupation of the exciton is required. Less critical is a residual occupation of the ground state: this reduces only the rate of entangled photon emission but not the entanglement. A figure of merit is the ratio of biexciton photons to exciton photons. The ideal case is a ratio of one where every exciton photon is part of the two photon cascade on biexciton decay, Fig. 5.2.1(f).

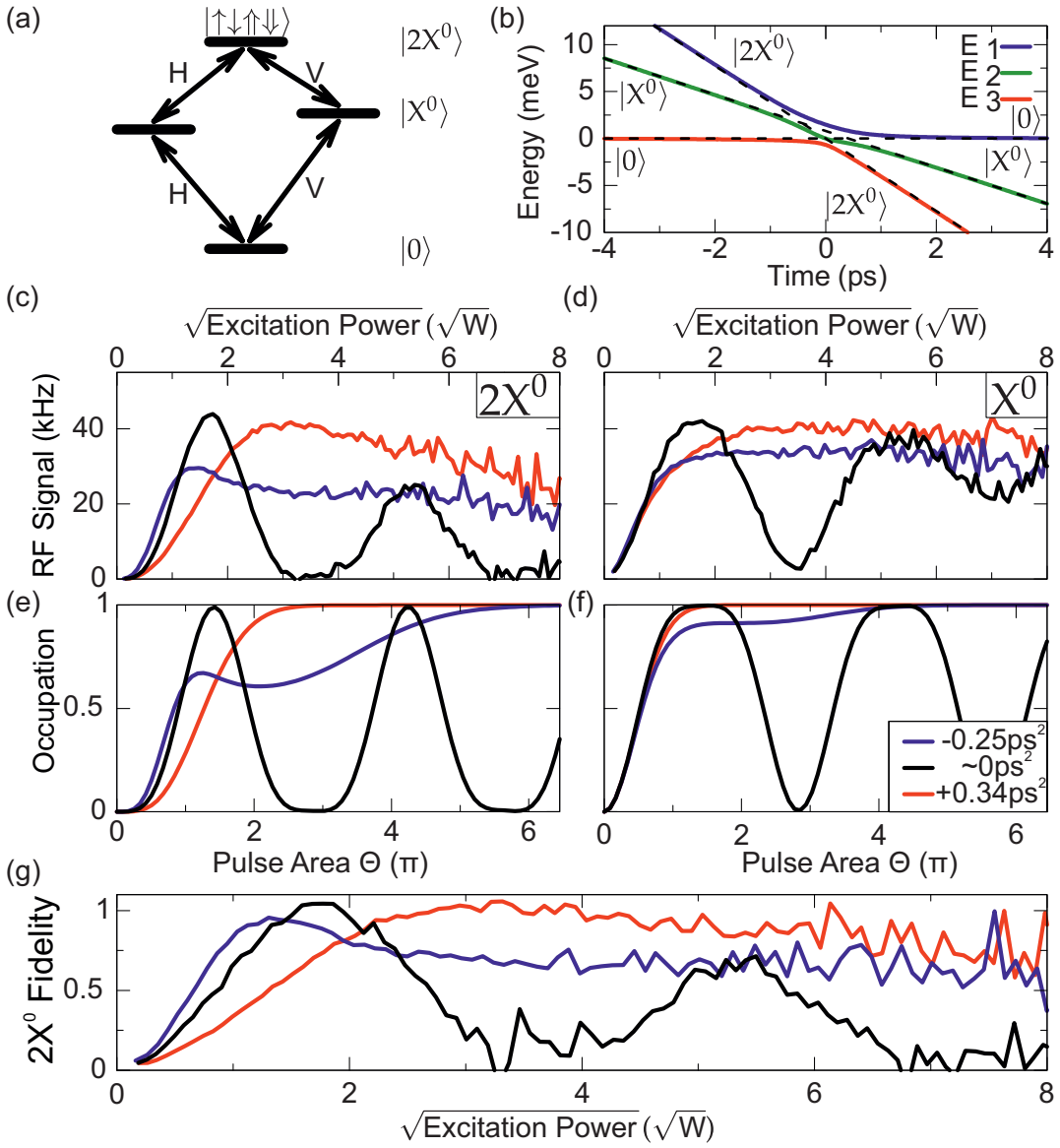

Figure 5.4.1: **Biexciton generation on QD1. (a)** Energy level scheme. **(b)** Instantaneous eigenenergies, the dressed states. **(c)** $2X^0$ emission and **(d)** X^0 emission as a function of the time-averaged square-root excitation power for different chirp parameters. **(e)** and **(f)** Simulation of the biexciton occupation and the sum of exciton and biexciton occupations as a function of the pulse area. **(g)** Ratio of the experimental data: $2X^0/X^0$.

Fig. 5.4.1 shows data from a single QD in the n-i-Schottky device. The laser pulses are centered at the two-photon biexciton resonance at 944.3 nm. The $2X^0$ and X^0 emission intensities and their ratio are shown as a function of the square-root of the excitation power in Fig. 5.4.1(c), (d) and (g), respectively. For close-to-zero chirp (black curves in Fig. 5.4.1), Rabi rotations are observed. At the first maximum, the X^0 and $2X^0$ emission intensities are equal to within an error of 5%, then both curves go down nearly to zero. At the second maximum, the $2X^0$ emission reduces to 75% of the $2X^0$ emission. For higher excitation power, we observe mainly X^0 emission with little emission from the $2X^0$. At the first maximum it is clear that ultrafast pulses with close-to-zero chirp enable high fidelity preparation of the biexciton by a Rabi rotation. However, this π-pulse excitation is very sensitive to variations in the detuning or excitation power. We turn to RAP which potentially offers a more robust scheme.

To create the biexciton using RAP, we first concentrate on positive chirp. Introducing a chirp of $+0.34\,\mathrm{ps}^2$ stretches the pulse to an intensity FWHM of 8 ps. In the experiment, the $2X^0$ emission rises more slowly with pulse power than in the Rabi rotation experiment (red curve in Fig. 5.4.1) but then reaches a very broad maximum. Both $2X^0$ and X^0 signals reach a common maximum where the signals correspond closely to the maximum achieved in the Rabi rotation experiment. These are the main signatures of RAP. In terms of $2X^0$ preparation, the ratio of $2X^0$ to X^0 emission reaches the ideal case of 100% with an error of 5%, proving that we can achieve a high fidelity biexciton preparation with RAP, robust against power and detuning fluctuations.

We now focus on the response of the system to a negative chirp of $-0.25\,\mathrm{ps}^2$ (pulse duration of 6 ps, blue curves in Fig. 5.4.1). In this case the $2X^0$ signal rises at smaller pulse areas than for positive chirp and in fact at even smaller pulse areas than the Rabi rotations. The maximum of the $2X^0$ signal is considerably less than the signal following a π Rabi pulse. The maximum X^0 signal is likewise reduced. The highest $2X^0$ to X^0 ratio is 94% decreasing rapidly at high pulse areas. A negative chirp works less well at $2X^0$ creation than a positive chirp. However, at higher excitation powers the difference between positive and negative chirp becomes less and less pronounced.

An analysis of the calculated instantaneous eigenenergies, the dressed states Fig. 5.4.1(b), allows a qualitative understanding of the physics. Starting in the ground state $|0\rangle$, the system evolves along the lower (red) branch for positive chirp. Provided that the pulse area is above the RAP threshold, the system remains in the lower branch at the $|0\rangle$ and $|2X^0\rangle$ avoided crossing such that the system ends up in the biexciton state $|2X^0\rangle$. Although there is no direct coupling between the $|0\rangle$ and $|2X^0\rangle$ states, the avoided crossing arises as $|0\rangle$ and $|2X^0\rangle$ have a common coupling to the $|X^0\rangle$ state. Phonons can interrupt the adiabatic transfer by causing a jump from one branch to the other one [Glässl et al., 2013]. For positive chirp, the system starts in the lowest energy dressed state and only phonon absorption is possible. At 4.2 K however, phonons at the relevant energy scale are frozen out and the probability for absorption is small. Hence the process with positive chirp is barely affected by phonons at low temperature. Conversely, for negative chirp the system starts out in the upper-most branch (blue curve in Fig. 5.4.1(b) with time running from "right" to "left"); the system can now jump to lower branches by phonon emission, a process which is possible even at low temperature. This leads to a significant probability of exciton and ground state population, reducing the fidelity of the RAP process. All these observations correspond well to the experimental data.

The theory provides a quantitative account of three-level RAP in the presence of phonon coupling. We calculate the $2X^0$ and X^0 occupations as a function of the pulse area: the $2X^0$ signal is proportional to the $2X^0$ occupation; the X^0 signal is proportional to the sum of the $2X^0$ and X^0 occupations. The simulation results are also shown in Fig. 5.4.1 and reproduce the main features of the experimental data extremely well, notably the exact form of the Rabi oscillations for close-to-zero chirp (a broad minimum at pulse area $\sim 3\pi$ in the $2X^0$ signal, a broad maximum at $\sim 1.5\pi$ in the X^0 signal); the "delayed" ("accelerated") rise of the $2X^0$ signal for positive (negative) chirp; the relative signal strengths; and the better RAP performance for positive chirp. In the theory, the Rabi rotations are not influenced significantly by phonons because the Rabi dynamics

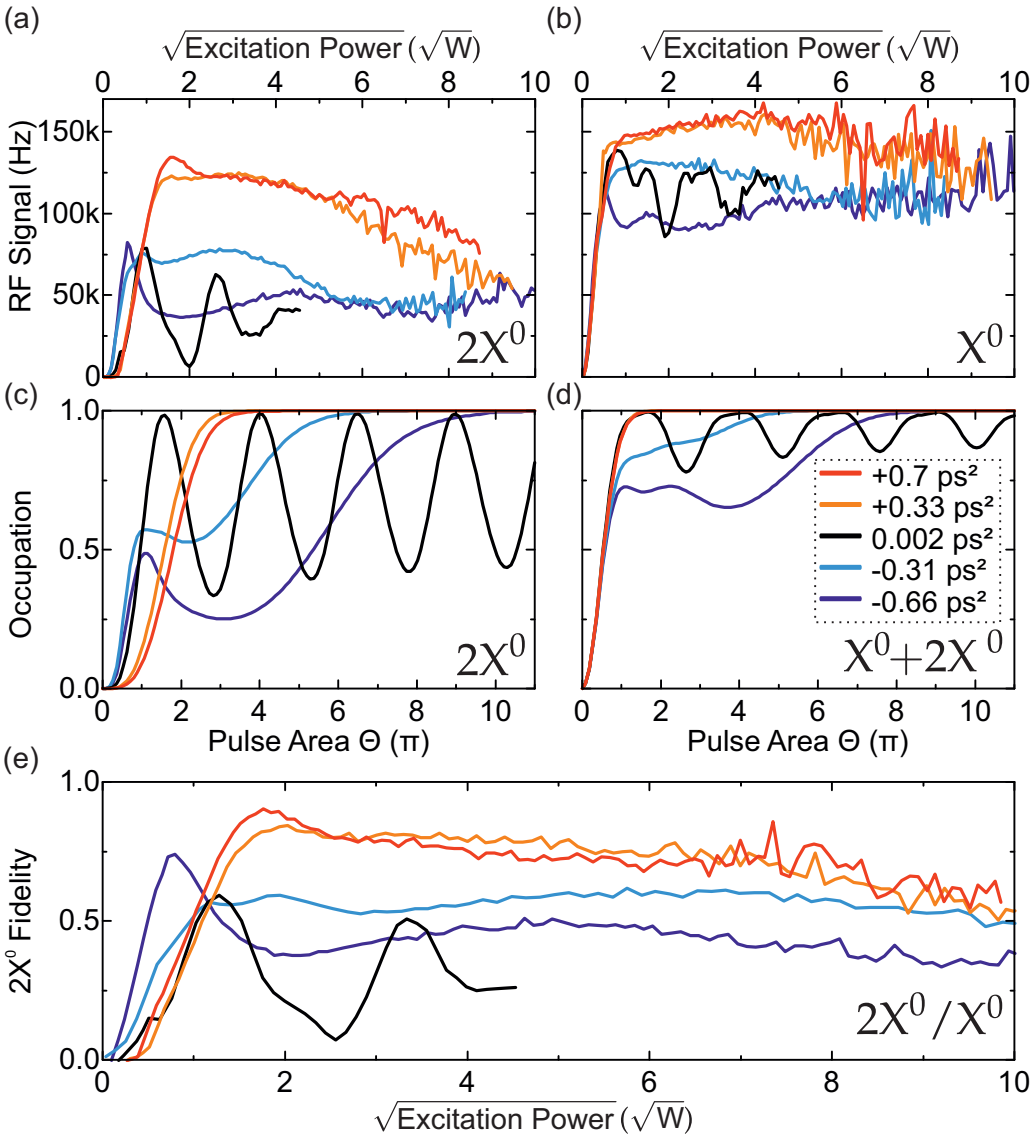

Figure 5.4.2: **Biexciton generation on QD2.** **(a)** $2X^0$ emission and **(b)** X^0 emission as a function of the time-averaged square-root excitation power for different chirp parameters. **(c)** and **(d)** Simulation of the biexciton occupation and the sum of exciton and biexciton occupations as a function of the pulse area. **(e)** Ratio of the experimental data: $2X^0/X^0$.

are too fast for the phonons to follow. The theoretical results show clearly that $2X^0$ generation with RAP is strongly (weakly) influenced by phonons for negative (positive) chirp for small to modest pulse areas. At the highest pulse areas, however, the theory predicts essentially perfect RAP independent of the sign of the chirp. The interpretation is that the splittings between the branches at the avoided crossings are energetically so large that they lie well above the energy range of the phonons which are efficiently coupled to the exciton system [Reiter et al., 2014]. In other words, the wavelength of the phonons required for scattering between the dressed states becomes much smaller than the size of the QD at high pulse area. There is evidence that this reduction of the phonon efficiency is also seen in the experiment: the RAP signals for positive and negative chirp approach each other at the largest pulse areas. However, in addition the experimental signals exhibit a decay at high pulse areas which cannot be explained by the phonon coupling model. Instead, we tentatively attribute this decay to an occupation of higher energy levels by multi-photon absorption [Patton et al., 2005].

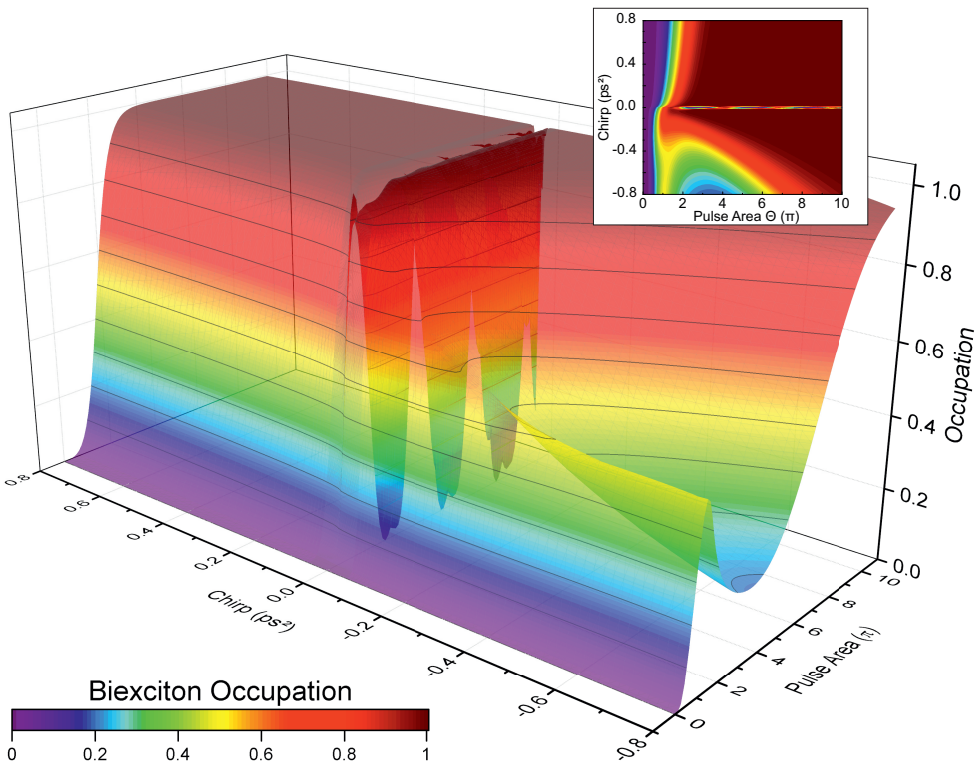

Figure 5.4.3: **Calculated biexciton generation on QD2.** Simulation of the biexciton occupation as a function of the chirp parameter and the pulse area. The inset shows the top-view with the same color-scale.

To stress-test biexciton generation with RAP, we probe a second QD with much larger biexciton binding energy. RAP is more difficult in this case: the pulse area required for efficient $2X^0$ generation increases, potentially entering the regime in which the additional decay process is active. The second QD, embedded in the n-i-p sample Fig. 5.2.1(a), with biexciton resonance at wavelength 938.2 nm, has a biexciton binding energy of 3.4 meV (the first QD has a binding energy of 1.5 meV). The $2X^0$ emission intensity of the RAP experiment is shown in Fig. 5.4.2. Despite the large biexciton binding energy, the ratio of the $2X^0$ to X^0 signals reaches 90%, Fig. 5.4.2(e). The general behavior is the same as for the first QD: a Rabi rotation-like behavior for minimal chirp and a distinct difference between positive and negative chirp. Again, apart from the decay at high pulse areas, the theory accounts extremely well for the experimental data. Notably, we find that for stronger negative chirp values, the phonons also become more effective resulting in a broader and deeper minimum of biexciton occupation which shifts to higher pulse areas, Fig. 5.4.3. Further, the RAP onset occurs at smaller pulse areas for negative chirp than for positive chirp, Fig. 5.4.3, a feature of the experimental data in Fig. 5.4.2(a).

In conclusion, we have demonstrated the coherent generation of a biexciton in a semiconductor quantum dot using a single chirped laser pulse. The state preparation has a very high fidelity over a broad range of excitation powers. The sign of the chirp is important: the scheme is robust with respect to phonon scattering at low temperature for positive chirp. A negative chirp results in damping due to phonon scattering. Theoretical calculations including a microscopic coupling to phonons reproduce all the experimental features apart from a damping in the experiment at high pulse areas.

5.5 Supplementary Information

5.5.1 Experimental Methods

The quantum dot samples

We studied in this work self-assembled InGaAs quantum dots (QD) in two different heterostructures. In both cases the QDs are embedded in a GaAs diode grown by molecular beam epitaxy. One diode is an n-i-Schottky structure [Warburton et al., 2000; Drexler et al., 1994], the other an n-i-p structure [Prechtel et al., 2016], Fig. 5.5.1(a) and (b), respectively. The n-i-Schottky diode uses an n-doped back-contact and a semi-transparent metallic top-contact (Ti/Au 3 nm/7 nm). The n-i-p sample on the other hand has an epitaxial top gate made from carbon-doped GaAs. In addition, the n-i-p diode features a distributed Bragg reflector (DBR). The layer structures are given in Table 5.5.1 and Table 5.5.2 for the n-i-Schottky and n-i-p diode, respectively. In the n-i-p diode, the

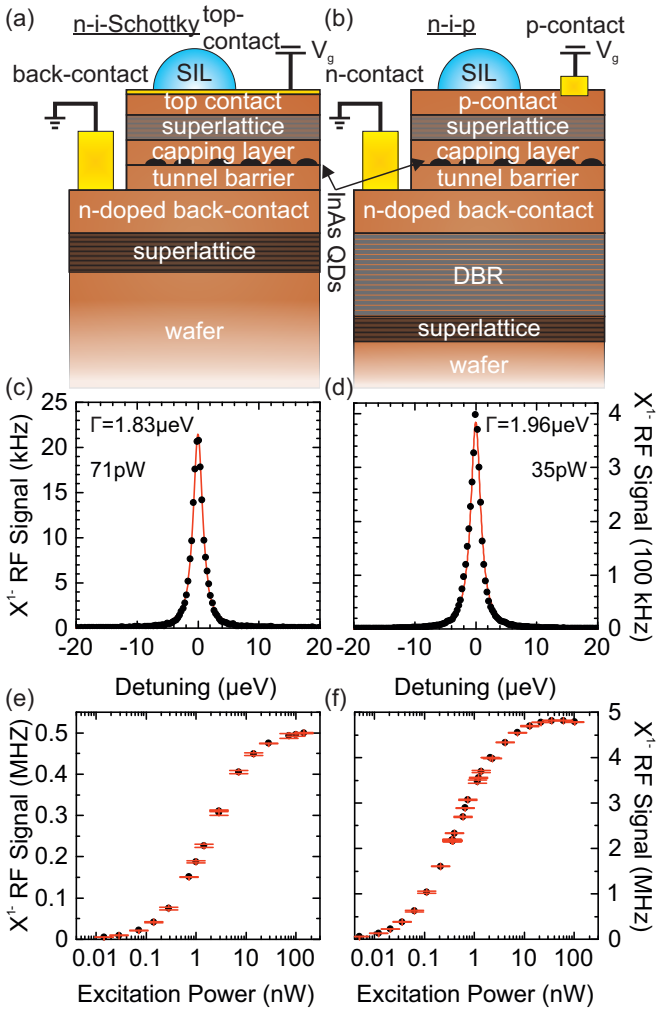

Figure 5.5.1: **Resonance fluorescence (RF) spectroscopy on a quantum dot (QD) with narrowband continuous wave excitation. (a)** n-i-Schottky, and **(b)** n-i-p layer structure. **(c)-(f)** Comparison of the RF performance with narrowband continuous wave excitation of a single QD in the n-i-Schottky (left) and n-i-p structure (right). **(c)-(d)** Example spectra showing the RF signal as function of laser detuning at an excitation power of 71 pW (c), 35 pW (d). A Lorentzian fit (red solid line) to the black data points shows a FWHM of 1.83 μeV (c), 1.96 μeV (d). The linewidths are similar in both devices. **(e)-(f)** RF signal as a function of excitation power for the n-i-Schottky device (e), and n-i-p device (f). The saturation count rate is a factor of ten higher in the n-i-p sample.

final layer, 44 nm undoped GaAs, places the p-doped layer around a node-position of the standing electromagnetic wave in the n-i-p diode.

In the experiment, the n- and p-doped layers are contacted independently. Selective etching of the capping allows the buried p-layer to be contacted. Access to the n-layer is provided by wet etching of a mesa structure. In both devices the n-contact is grounded and a gate voltage V_g is applied to the top gate. The gate voltage allows control over the QD charge via Coulomb blockade and excitonic resonances can be shifted by the DC Stark effect [Warburton et al., 2000; Dalgarno et al., 2008; Warburton, 2013]. The performance of single quantum dots (QDs) in both diode structures is quite similar. The main advantage of the n-i-p diode over the n-i-Schottky device is a strongly enhanced photon extraction. This is achieved on the one hand by the DBR and on the other hand by the low-loss epitaxial gate.

Resonance fluorescence with continuous wave excitation

In resonance fluorescence (RF) spectroscopy we investigated the quantum dot characteristics with a narrow band (linewidth in sub pm range) excitation laser. The scattering induced by resonant excitation is detected. Back-reflected laser light is suppressed with a dark-field technique leading to an extinction ratio of 10^7:1 [Kuhlmann et al., 2013b,a]. Typical X^{1-} spectra at low excitation power from single QDs in the two samples are depicted in Fig. 5.5.1(c) and (d). The linewidths are very similar, around 2 µeV, approximately 2.5 times larger than the transform limit [Kuhlmann et al., 2013b]. A signal:background ratio of more than 1,000:1 is achieved with linearly polarized excitation. A more distinct difference between QDs in the two devices appears in the saturation behaviour, Fig. 5.5.1(e) and (f): we detected single photons with a count-rate of 5 MHz from the n-i-p sample, about 10 times more than from the n-i-Schottky sample. The high photon extraction efficiency of the n-i-p device, around 10%, results from two improvements in the sample design as discussed above: the n-i-p type features a DBR and also a transparent epitaxial gate.

Resonance fluorescence with pulsed excitation

With pulsed excitation, we use the full spectrum of 130 fs transform-limited "ultra-fast" pulses, again exciting the QD resonantly. The spectral full-width-at-half-maximum (FWHM) of the pulse is $\Delta\lambda = 10$ nm. With this bandwidth we address the ground state transition for the particular charge state set by the gate voltage (but not higher energy transitions). The RF response of the QD is detected with a grating spectrometer.

A scheme of the complete set-up is shown in Fig. 5.5.2. The ultra-fast pulses from a mode-locked femtosecond laser are expanded and sent into a compact pulse-shaper. The pulse-shaper retains all the spectral components and controls the amount of chirp as described below. From here the

Function	Material	Thickness
wafer	GaAs	
buffer	GaAs	50 nm
superlattice, 30 periods	AlAs, GaAs	120 nm
spacer	GaAs	50 nm
electron reservoir (back contact)	GaAs:Si	50 nm
tunnel barrier	GaAs	25 nm
InGaAs QDs	InAs	∼1.6 ML
capping layer	GaAs	150 nm
blocking barrier, 68 periods	AlAs, GaAs	272 nm
capping layer	GaAs	10 nm

Table 5.5.1: Layers of the heterostructure, n-i-Schottky diode. The quantum dots (QD) are formed by depositing 1.6 monolayer (ML) of InAs.

Function	Material	Thickness
wafer	GaAs	
buffer	GaAs	50 nm
superlattice, 18 periods	GaAs, AlAs a 2 nm	72 nm
DBR, 16 periods	GaAs, AlAs	2400 nm
spacer	GaAs	57.3 nm
electron reservoir (back contact)	GaAs:Si	50 nm
tunnel barrier	GaAs	30 nm
InGaAs QDs	InAs	∼1.6 ML
capping layer	GaAs	153 nm
blocking barrier, 46 periods	AlAs, GaAs	184 nm
p-doped top contact	GaAs:Si	30.5 nm
undoped spacer	GaAs	1 nm
etch stop	AlAs	2 nm
capping layer	GaAs	44 nm

Table 5.5.2: Layers of the heterostructure, n-i-p diode.

pulses pass through power control and polarization optics and are then coupled into a single mode optical fiber. The fiber transports the pulses to a confocal microscope. In the microscope, the excitation pulses pass through a linear polarizer, two beam-splitters and are sent to the objective at cryogenic temperature (4.2 K). The objective, an aspherical lens with a numerical aperture of 0.68, focuses the light onto the sample. The sample is held on a stack of piezo-steppers which allows a particular QD to be placed within the focal spot of the microscope. This process is aided by the in situ diagnostics provided by a camera image of the focus. Light scattered by the QD is collected and coupled into the detection fiber. The back-reflected laser light is suppressed by a second linear polarizer whose axis is orthogonal to the axis of the polarizer in the excitation stage. The RF signal is detected directly with a SPAD (continuous wave excitation) or with a spectrometer-CCD camera (pulsed excitation).

Detecting RF with pulsed excitation also depends on suppressing the reflected laser light with the polarization-based dark-field technique. However, owing to the wavelength dependence of the polarization optics, the laser suppression of a broadband pulsed laser is less effective than with the narrowband continuous wave laser: we reach an extinction ratio of typically 10^5:1 with broadband excitation. We use in addition the spectral mismatch between the broadband laser and the narrowband RF to increase the extinction ratio, Fig. 5.5.3. The laser background falling on the CCD camera does not depend on the gate voltage, Fig. 5.5.3(a), such that we can use the gate voltage dependence of the QD emission to construct the laser background spectrum. The resulting residual laser background is shown in Fig. 5.5.3(b) in red. The spectral shape is explained by the Gaussian spectral shape of the excitation laser along with the quadratic function of laser suppression: the laser suppression is most effective at its alignment wavelength and then decays quadratically in wavelength superimposed by interference fringes. A typical spectrum measured at $V_g = -12\,\mathrm{mV}$ is shown in black. Sharp emission peaks from the exciton and biexciton appear on top of the laser background. The signal after background subtraction is shown in the lower plot in blue. Before background subtraction, the maximum signal to background ratio in a narrow spectral window around the emission line is 22:1.

Pulse shaping: introducing chirp

Chirp is introduced into the transform-limited laser pulses by a compact, folded $4f$ pulse-shaper [Martinez, 1987; Weiner et al., 1992]. The scheme is depicted in the main paper in Fig. 5.2.1(e). The unchirped pulse is diffracted by a high resolution, blazed grating (1800 grooves per mm) and

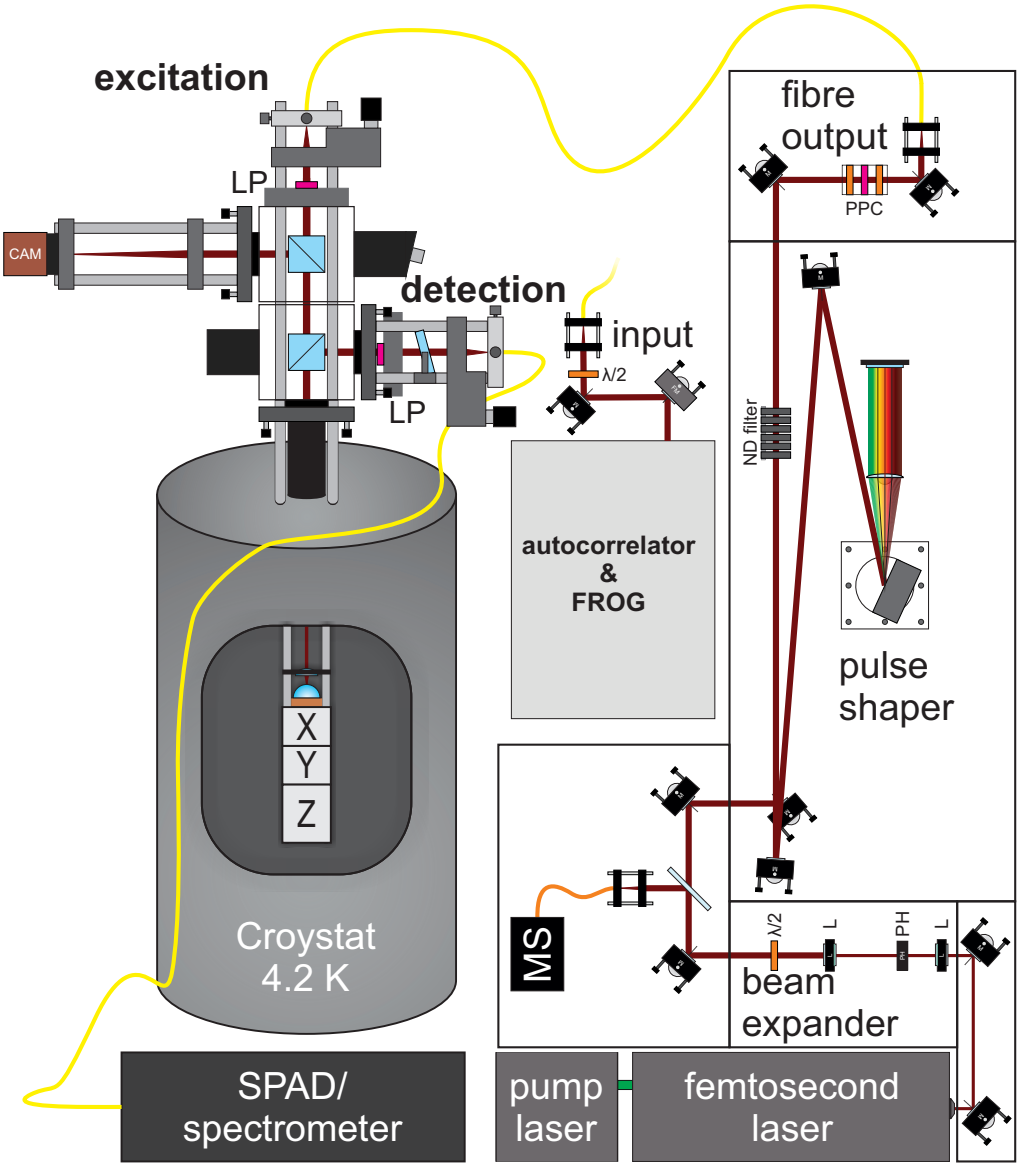

Figure 5.5.2: **Scheme of the complete set-up.** Ultra-short pulses were manipulated in a pulse-shaper, coupled into a single mode glass fiber and sent to a confocal microscope mounted on a bath cryostat. The pulses were characterized with a combination of autocorrelator and frequency-resolved-gating (FROG). The sample is held at a temperature of 4.2 K in the bath croystat on an xyz-positioner. A mini spectrometer (MS) measures the spectral profile of the pulses.

then focused by a lens onto a mirror positioned in the focal plane. From here the light travels back under a small angle with respect to the diffraction plane allowing a spatial separation of incoming and outgoing pulses. The distance between grating and lens controls the chirp [Martinez, 1987]. The lens and the mirror are mounted on a translation platform. Moving the platform with respect to the grating changes the chirp: if the distance matches the focal length of the lens the chirp is zero, a larger (smaller) distance leads to negative (positive) chirp. The temporal duration of the pulses exiting the laser is 130 fs (intensity FWHM); the temporal duration can be stretched up to 15 ps corresponding to a chirp in the range from $-0.7\,\mathrm{ps}^2$ to $0.7\,\mathrm{ps}^2$.

We characterized the chirp with a combination of a FROG and autocorrelator. This allows us to reveal the presence of any high-order phase terms and prevent them by an optimal adjustment of the pulse-shaper. The chirp is measured both in the free space mode and also after the optical single mode fiber in order to determine the sign of the chirp and to compensate for the chirp

introduced by the fiber itself.

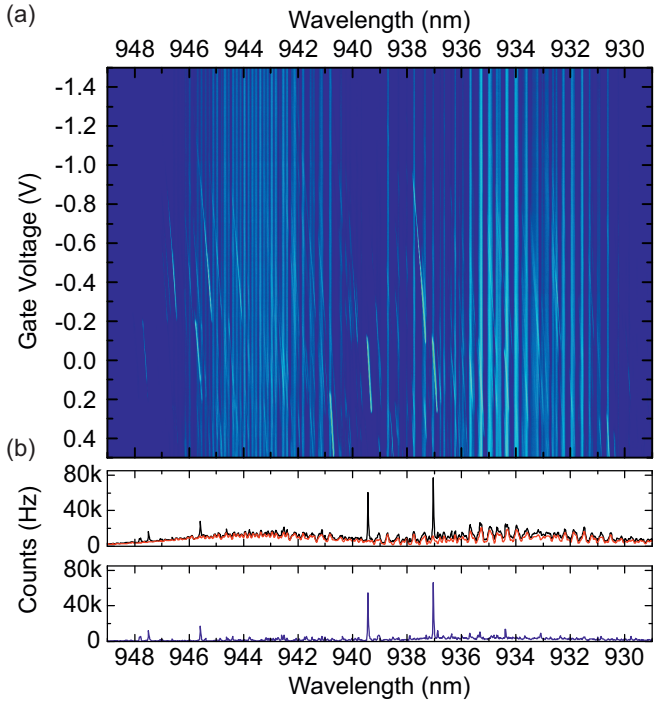

Figure 5.5.3: **Laser background subtraction resonance fluorescence spectroscopy using broadband, pulsed excitation. (a)** The RF signal as a function of gate voltage without background subtraction measured with an excitation power of $\sim 8\,\mu W$ corresponding to a pulse area of around $3\,\pi$. **(b)** One spectrum from (a) at a gate voltage of $-0.012\,V$ is shown as black curve in the upper panel. Distinct peaks from the exciton and trion are visible toegther with a broad laser background. The reconstructed laser background (from all spectra in (a)) is shown in red. The blue curve in the lower panel shows the difference of the black and the red curve, the resulting signal after background subtraction.

5.5.2 Theoretical Model

Hamiltonian

The Hamiltonian is composed of four parts

$$H = H_{\mathrm{c}} + H_{\text{c-l}} + H_{\mathrm{ph}} + H_{\text{c-ph}},$$

with H_{c} denoting the electronic structure, $H_{\text{c-l}}$ the carrier-light coupling, H_{ph} the free phonons and $H_{\text{c-ph}}$ the carrier-phonon coupling.

We consider a three-level system consisting of the ground state $|0\rangle$, the single exciton state $|\mathrm{X}^0\rangle$ and the biexciton state $|2\mathrm{X}^0\rangle$ yielding the Hamiltonian for the electronic system

$$H_{\mathrm{c}} = \hbar\omega_{\mathrm{X}^0}|\mathrm{X}^0\rangle\langle\mathrm{X}^0| + \hbar\omega_{2\mathrm{X}^0}|2\mathrm{X}^0\rangle\langle 2\mathrm{X}^0|.$$

Here, $\hbar\omega_{\mathrm{X}^0}$ is the energy of the neutral exciton and $\hbar\omega_{2\mathrm{X}^0} = 2\hbar\omega_{\mathrm{X}^0} - \Delta_B$ is the energy of the biexciton accounting for the biexciton binding energy Δ_B; the ground state energy has been set to zero. For the binding energy we take the experimentally determined values (corrected for the polaron shift) $\Delta_B = 1.4$ meV for QD1 and $\Delta_B = 3.2$ meV for QD2.

We model the carrier-light interaction in the usual dipole and rotating wave approximation resulting in the following Hamiltonian for the three-level system:

$$H_{\text{c-l}} = \frac{1}{2}\hbar\Omega(t)\left(|\mathrm{X}^0\rangle\langle 0| + |2\mathrm{X}^0\rangle\langle\mathrm{X}^0|\right) + \text{h.c.},$$

h.c. denoting the Hermitian conjugate. Here the instantaneous Rabi frequency $\Omega(t)$ with $\hbar\Omega(t) = 2\mathbf{M}\cdot\mathbf{E}(t)$ enters, given by the positive frequency component of the electric field $\mathbf{E}(t)$ and the dipole matrix element $\mathbf{M}$.

For the carrier-phonon interaction, we account for the deformation potential coupling to longitudinal acoustic (LA) phonons which has been shown to be the main source of decoherence in most typical QDs [Reiter et al., 2014]. The Hamiltonian of the free phonons is given by

$$H_{\mathrm{ph}} = \hbar\sum_{\mathbf{q}}\omega_{\mathbf{q}}b_{\mathbf{q}}^{\dagger}b_{\mathbf{q}},$$

with the creation (annihilation) operators $b_{\mathbf{q}}^{\dagger}$ ($b_{\mathbf{q}}$) of a phonon with wave vector $\mathbf{q}$ and frequency $\omega_{\mathbf{q}} = c_{\mathrm{LA}}|\mathbf{q}|$, c_{LA} being the longitudinal sound velocity.

The carrier-phonon interaction is described by the standard pure-dephasing Hamiltonian. Assuming for the biexciton wave function a product of exciton wave functions, the Hamiltonian reads

$$H_{\text{c-ph}} = \hbar\sum_{\mathbf{q},\nu} n_\nu|\nu\rangle\langle\nu|\left(g_{\mathbf{q}}b_{\mathbf{q}} + g_{\mathbf{q}}^{*}b_{\mathbf{q}}^{\dagger}\right),$$

where the factor n_ν counts the number of the excitons which are present in the state $|\nu\rangle$, i.e., $n_\nu = 0$ for $|\nu\rangle = |0\rangle$, $n_\nu = 1$ for $|\nu\rangle = |\mathrm{X}^0\rangle$, and $n_\nu = 2$ for $|\nu\rangle = |2\mathrm{X}^0\rangle$.

The corresponding matrix elements for deformation potential coupling to electrons and holes are

$$g_{\mathbf{q}}^{e/h} = \sqrt{\frac{q}{2V\rho\hbar c_{\mathrm{LA}}}}D_{e/h}F_{\mathbf{q}}^{e/h},$$

with V the normalization volume, ρ the mass density of the crystal, and $D_{e/h}$ the deformation potential coupling constants for electrons/holes. We take GaAs parameters as listed in Table 5.5.3. The exciton coupling matrix element is obtained from the electron and hole coupling matrix elements by $g_{\mathbf{q}} = g_{\mathbf{q}}^{e} - g_{\mathbf{q}}^{h}$.

Parameter		Value
density	ρ	$5370\,\mathrm{kg/m^3}$
sound velocity	c_{LA}	$5.1\,\mathrm{nm/ps}$
electron deformation potential constant	D_e	7 eV
hole deformation potential constant	D_h	−3.5 eV

Table 5.5.3: Parameters used in the calculations.

The influence of the QD geometry is described in terms of the form factor $F_{\mathbf{q}}^{e/h}$. We assume a spherical QD modeled by a harmonic confinement potential yielding the form factors

$$F_{\mathbf{q}}^{e/h} = \exp\left(-q^2 a_{e/h}^2/4\right),$$

where $a_{e/h}$ are the electron/hole localization lengths. To fit the experimental data we used $a_e = 5$ nm and $a_h = 2$ nm. We note that similar values have been used in the theoretical modeling of phonon-assisted state preparation schemes [Quilter et al., 2015].

For the theoretical modeling of the light-induced dynamics we use the density matrix formalism. The infinite hierarchy of phonon-assisted variables appearing in the equations of motion is truncated using a fourth-order correlation expansion. It has been shown that this method gives very reliable results in a two-level system [Reiter et al., 2014; Lüker et al., 2012; Glässl et al., 2011]. Here we have extended this approach to the three-level model. This extension is straightforward, however the numerical complexity increases considerably. Based on this formalism, we calculate the occupations of the biexciton $\langle|2\mathrm{X}^0\rangle\langle 2\mathrm{X}^0|\rangle$ and the neutral exciton $\langle|\mathrm{X}^0\rangle\langle\mathrm{X}^0|\rangle$ states. Note that also all coherences between these states as well as one- and two-phonon assisted density matrices are fully included in the calculation.

Chirped laser pulses

To model the optical excitation, we consider an electric field which describes a linearly chirped Gaussian laser pulse. Such a chirped pulse is generated from a transform-limited Gaussian laser pulse of the form

$$\Omega_0(t) = \frac{\Theta}{\sqrt{2\pi}\tau_0} \exp\left(\frac{t^2}{2\tau_0^2}\right) \exp\left(-i\omega_L t\right)$$

with pulse duration τ_0, central laser frequency ω_L, and pulse area Θ. After application of a chirp with coefficient α the laser pulse is transformed to

$$\Omega(t) = \frac{\Theta}{\sqrt{2\pi\tau_0\tau}} \exp\left(\frac{t^2}{2\tau^2}\right) \exp\left(-i\omega_L t - \frac{1}{2}at^2\right).$$

As a result of the chirp the pulse duration is increased to $\tau = \sqrt{\frac{\alpha^2}{\tau_0^2} + \tau_0^2}$, while the central frequency of the laser pulse changes with time according to the frequency chirp rate $a = \frac{\alpha}{\alpha^2+\tau_0^4}$. The central laser frequency at the pulse maximum is set to the arithmetic mean of the ground state-to-exciton and exciton-to-biexciton transition frequencies, such that a two-photon process with this frequency resonantly drives the biexciton.

6 Coherent Control Nano-Imaging of Two-Level Systems

Adapted from:
"**Optical nanoscopy via quantum control"**
A scheme for nanoscopic imaging of a coherent quantum mechanical system, a two-level atom, using a far-field optical probe.

Timo Kaldewey[1], Andreas V. Kuhlmann[1,2], Sascha R. Valentin[3], Arne Ludwig[3], Andreas D. Wieck[3], and Richard J. Warburton[1]

[1]Department of Physics, University of Basel, Klingelbergstrasse 82,
CH-4056 Basel, Switzerland

[2]IBM Research-Zurich, Säumerstrasse 4,
CH-8803 Rüschlikon, Switzerland

[3]Lehrstuhl für Angewandte Festkörperphysik, Ruhr-Universität Bochum,
D-44780 Bochum, Germany

Submitted to: *Sciences Advances*, October 2016

6.1 Abstract

We present a scheme for nanoscopic imaging of a quantum mechanical two-level system using an optical probe in the far-field. Existing super-resolution schemes require more than two-levels and depend on an incoherent response to the lasers. Here, quantum control of the two states proceeds via rapid adiabatic passage. We implement this scheme on an array of semiconductor self-assembled quantum dots. Each quantum dot results in a bright spot in the image with extents down to 30 nm ($\lambda/31$). Rapid adiabatic passage is established as a versatile tool in the super-resolution toolbox.

6.2 Introduction

The diffraction limit prevents a conventional optical microscope from imaging at the nano-scale. Significantly however, diffraction-unlimited imaging of individual molecules is possible by creating an intensity-dependent molecular switch [Betzig et al., 2006; Hell, 2009]. For instance, molecular fluorescence can be turned on with green laser light (absorption of a green photon followed by relaxation), and subsequently turned off with red laser light (stimulated depletion). Fluorescence is only allowed when the power of the red laser is below threshold: the red laser acts as an on-off switch. This switching capability is translated into a microscopy scheme called STED (stimulated emission depletion microscopy) through a "doughnut" intensity profile of the red beam [Hell and Wichmann, 1994; Klar et al., 2000; Willig et al., 2007; Rittweger et al., 2009]. Practical considerations and not diffraction per se limit the resolving power of such an imaging scheme. A number of variants on this basic scheme exist [Hell, 2007, 2009; Weisenburger and Sandoghdar, 2015]. However, all these schemes use more than two quantum states – the STED protocol for example uses at least four quantum states (two separate vibronic transitions) – and all the schemes exploit an incoherent response to the lasers. Missing is a protocol for diffraction-unlimited imaging of a coherent two-level system (TLS).

The coherent response of a TLS to a pulse of resonant laser light is a Rabi oscillation, a rotation of the quantum state around the Bloch sphere. For instance, the system is driven from its ground state $|0\rangle$ to the excited state $|1\rangle$ and then back to $|0\rangle$ and so on, Fig. 6.2.1(B). In terms of fluorescence, Rabi oscillations

represent an off-on-off-on... behavior as a function of pulse area. If the TLS is illuminated with a high intensity pulse with Gaussian spatial profile then a series of rings in the optical response results [Gerhardt et al., 2010]. In other words, Rabi oscillations do not represent a simple on-off switch and are not well suited to imaging. We propose instead that rapid adiabatic passage (RAP) is an excellent technique for imaging a TLS. In RAP, the laser frequency is swept through the resonance of the TLS during the pulse. RAP transfers the population from one state to the other but without the oscillations at large pulse energies, Fig. 6.2.1(B). Applied to an ideal TLS initially in state $|0\rangle$, a weak RAP pulse leaves the system in state $|0\rangle$ whereas a strong RAP pulse transfers the system to state $|1\rangle$; and vice versa for the system initially in state $|1\rangle$. The clear threshold of RAP on a TLS represents an ideal on-off switch with immediate applications in imaging.

Our scheme is shown in Fig. 6.2.1. The TLS is initially in the ground state $|0\rangle$. A pulse with positive chirp and above-threshold pulse area is applied. This inverts the TLS provided it is located somewhere within the diffraction-limited spot: it turns the system on. Subsequently, a pulse with negative chirp and above-threshold pulse area is applied. This pulse inverts the system a second time, leading to re-occupation of state $|0\rangle$: it turns the system off. However, when the first pulse has a Gaussian intensity distribution (Fig. 6.2.1(C)) and the second pulse a doughnut intensity distribution (Fig. 6.2.1(D)), the second pulse is inactive at the center of the doughnut. Under these conditions, the system is left in the upper "on" state $|1\rangle$ only when it is located close to the center of the doughnut. The system is then left to decay by spontaneous emission and the photon is detected. In this way, a fluorescence bright spot results at the center

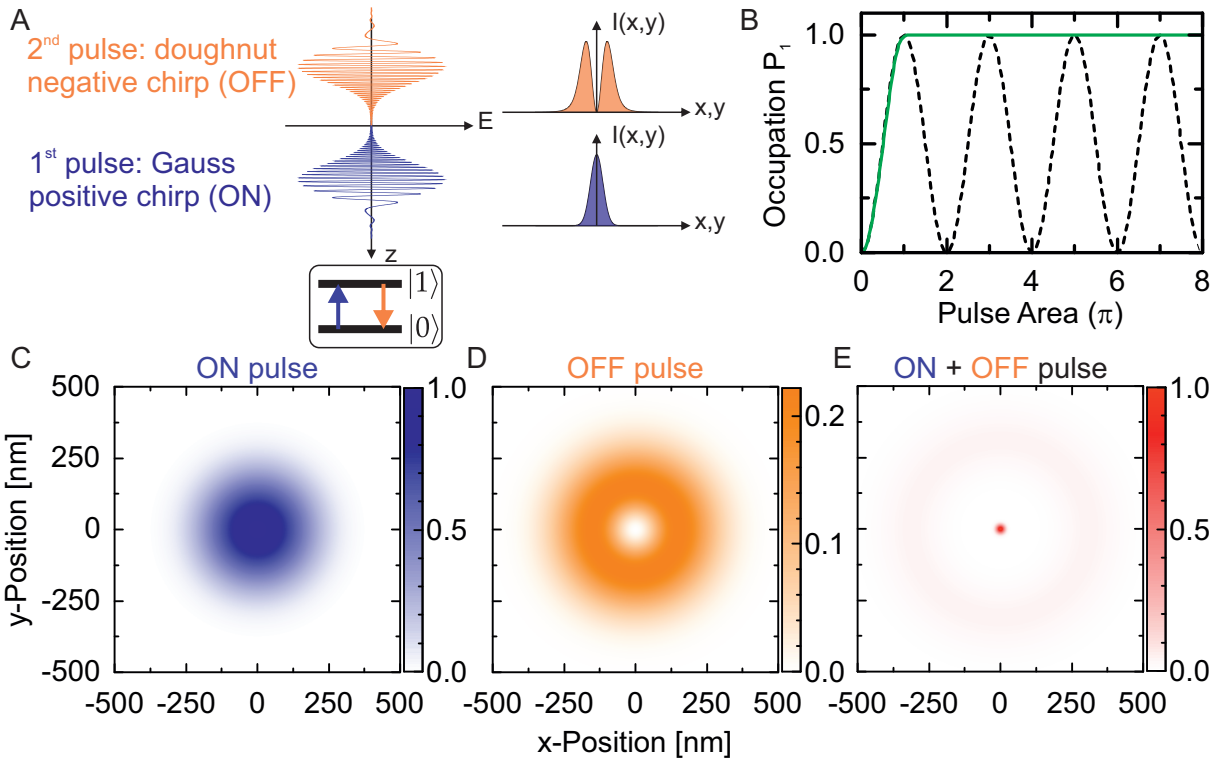

Figure 6.2.1: **Concept of nanoscopic imaging of a quantum mechanical two-level system. (A)** Temporal waveform and spatial intensity profile of the two optical pulses: excitation (positive chirp, Gaussian profile) and de-excitation (negative chirp, doughnut profile) pulse. **(B)** Response of an ideal two-level system to a single laser pulse. The system is initially in the ground state $|0\rangle$; plotted is the occupation of the excited state $|1\rangle$, P_1, as a function of pulse area. A resonant, unchirped pulse drives a Rabi oscillation (dashed black line). A chirped pulse (green solid line) transfers the system from state $|0\rangle$ to $|1\rangle$ for pulse areas above π by means of rapid adiabatic passage. **(C) - (E)** Simulation of the imaging experiment: P_1 as a function of sample (x, y)-position. (C) Gauss-pulse only with $I_G^0 = 1I_T$; (D) doughnut-pulse only with $I_D^0 = 1I_T$; (E) Gauss-pulse $I_G^0 = 3I_T$ followed by doughnut-pulse $I_D^0 = 205I_T$ resulting in a 15 times smaller spot size. Our model for the simulation is described in the supplementary material (see section 6.6). Here we used the following parameters: wavelength 940 nm, refractive index solid immersion lens $n_{\mathrm{SIL}} = 2.13$, beam diameter before the objective $\Delta X_{I,\mathrm{FWHM}} = 2.0\,\mathrm{mm}$, focal length $f = 3.7\,\mathrm{mm}$, detection efficiency $\beta = 1$, chirp $\alpha_{\mathrm{G}} = -\alpha_{\mathrm{D}} = 3.24\,\mathrm{ps}^{-2}$.

of the doughnut. The resolution in the image is determined by the spatial location at which the doughnut intensity crosses the RAP threshold, a "physics-based diffraction-unlimited" resolution [Hell, 2009]. This imaging scheme can be described analytically in a very simple way (Gaussian optics for the two beams, the Landau-Zener formalism [Shevchenko et al., 2010] for RAP): Fig. 6.2.1(E) shows how a bright spot emerges at the doughnut center. The full model is described in the supplementary material (see section 6.6).

Establishing an imaging protocol based on RAP strikes us as important. First, it opens up a way to image on the nano-scale coherent quantum optical systems such as cold atoms and trapped ions, also their solid-state counterparts, semiconductor quantum dots and color centers. Second, in a multi-level system, RAP avoids the excitation of molecular vibrations (phonons in a solid-state context). In STED microscopy, close to an eV of energy is dumped into the molecule per cycle, leading to blinking and bleaching. This heating can be avoided in RAP (by choosing positive chirp for the $|0\rangle \rightarrow |1\rangle$ process, negative chirp for the $|1\rangle \rightarrow |0\rangle$ process [Lüker et al., 2012; Wei et al., 2014]). Third, the chirped laser pulses are spectrally broadband yet the fluorescence is narrowband. This combination allows an inhomogeneous distribution of emitters (distribution in space or in time) to be addressed with the same laser pulses. Any spectral fingerprint in the emitters is retained by spectrally resolving the fluorescence, for instance with a spectrometer and array detector. Finally, our test system, a semiconductor quantum dot, is an extended emitter, with lateral extent ~ 5 nm. Although a quantum dot mimics a real atom it has a much larger size. Our scheme opens the perspective of imaging an electron wave function with a far-field, optical microscope.

6.3 Results

We use a single quantum dot to implement the RAP-based imaging scheme. At low temperature with resonant optical driving, an InGaAs quantum dot embedded in GaAs mimics closely a two-level atom with radiative lifetime 800 ps and emission wavelength 950 nm [Muller et al., 2007; Nguyen et al., 2011; Matthiesen et al., 2012; Kuhlmann et al., 2013a]. Here, state $|0\rangle$ is the crystal ground state (empty quantum dot), state $|1\rangle$ is an electron-hole pair (the neutral exciton, X^0), the result of promoting the highest energy valence electron across the fundamental gap to the lowest energy conduction state, Fig. 6.3.1(A). There are two optically-allowed excitons with spin ± 1 which can be created with $\sigma^{\pm}$ polarisation (σ represents circular polarisation), Fig. 6.3.1(A). We detect the spontaneous emission (technically, the "resonance fluorescence") as the exciton decays to the ground state. We reject back-reflected laser light with a polarisation-based dark-field concept [Vamivakas et al., 2009; Yilmaz et al., 2010; Kuhlmann et al., 2013a,b]: we excite with σ^+ and detect with σ^-, Fig. 6.3.1(B). (We note that the ± 1 states are coupled together by some symmetry breaking leading to a quantum beat [Tartakovskii et al., 2004] between $|+1\rangle$ and $|-1\rangle$ with period ~ 100 ps, Fig. 6.3.1(A). This coupling allows us to detect the decay of excitons with both spins.) The chirped laser pulses are created from transform-limited pulses from a mode-locked laser by introducing wavelength-dependent phase shifts. Unusually for quantum dot experiments [Simon et al., 2011; Wu et al., 2011; Wei et al., 2014], we use the full bandwidth of a 100 fs laser pulse: this allows us to address almost all the quantum dots in the sample with the same laser pulse despite the large inhomogeneous broadening. Fig. 6.3.1(C) plots the resonance fluorescence as a function of pulse area on a single quantum dot following excitation with a single laser pulse. The signal rises initially and is then roughly constant above a pulse area of π. The signal follows closely the Landau-Zener result for a TLS. Only difficulties in rejecting the back-reflected laser pulse at large laser power limit the maximum pulse area to 11π.

The RAP-based imaging proceeds by implementing the two-pulse scheme, creating an image by sample scanning. We consider initially imaging a single quantum dot by collecting the resonance fluorescence only at its X^0 emission wavelength, Fig. 6.3.2(A)-(C). The Gauss-pulse alone (pulse area π) gives a Gaussian spatial response with mean full-width-at-half-maximum (FWHM) 575 nm, slightly larger than the confocal diffraction-limited spot size on account of the non-linear response of RAP. Similarly, the response to the doughnut-pulse alone gives a doughnut-profile, with a width, as for the Gauss-pulse, determined largely by diffraction. Applying both pulses sequentially breaks the diffraction limit: a bright spot emerges with FWHM 56 nm in this particular experiment. The signal and the signal-to-background ratio at the central bright spot are almost the same as for the Gauss-pulse alone. This is a significant point: RAP-imaging simply concentrates the available signal to a smaller region in the image.

The FWHM of the central image decreases with increasing doughnut-pulse intensity, Fig. 6.3.2(F). This is the signature of "physics-based diffraction-unlimited" performance: it is the control of the on-off switching which determines the resolution, not the diffraction-limited focusing of the laser beams. The FWHM Δx follows the same functional form as for STED microscopy [Harke et al., 2008], $\Delta x(I_D) = \Delta x^o / \sqrt{1 + I_D/I_T}$ where Δx^o is the conventional diffraction limit, I_D is the dougnut intensity, and I_T the off-on threshold

intensity (see section 6.6). Here, we can anticipate $\Delta x(I_D)$ based only on the characterization of the microscope performance (resonance fluorescence from Gauss beam at intensities well below saturation) and RAP characterization on the quantum dot. The result describes the experimentally determined FWHM extremely well, Fig. 6.3.2(F).

A key application of super-resolution microscopy is to garner an image with detail which is obscured in a diffraction-limited microscopy. We demonstrate this by imaging a region of the sample containing a number of quantum dots separated laterally by distances smaller than or comparable to the diffraction limit of the microscope. An image with the Gauss-pulse alone, equivalently the doughnut-pulse alone, shows structure but it is difficult to determine the number and location of individual emitters, Fig. 6.3.2(G),(H). With the RAP-based imaging, the number and location of the point-like emitters is clearly visible, Fig. 6.3.2(I). The RAP-based imaging in the present experiment is limited only by the technical difficulty of distinguishing the resonance fluorescence signal from the reflected laser light at the highest doughnut-pulse peak areas.

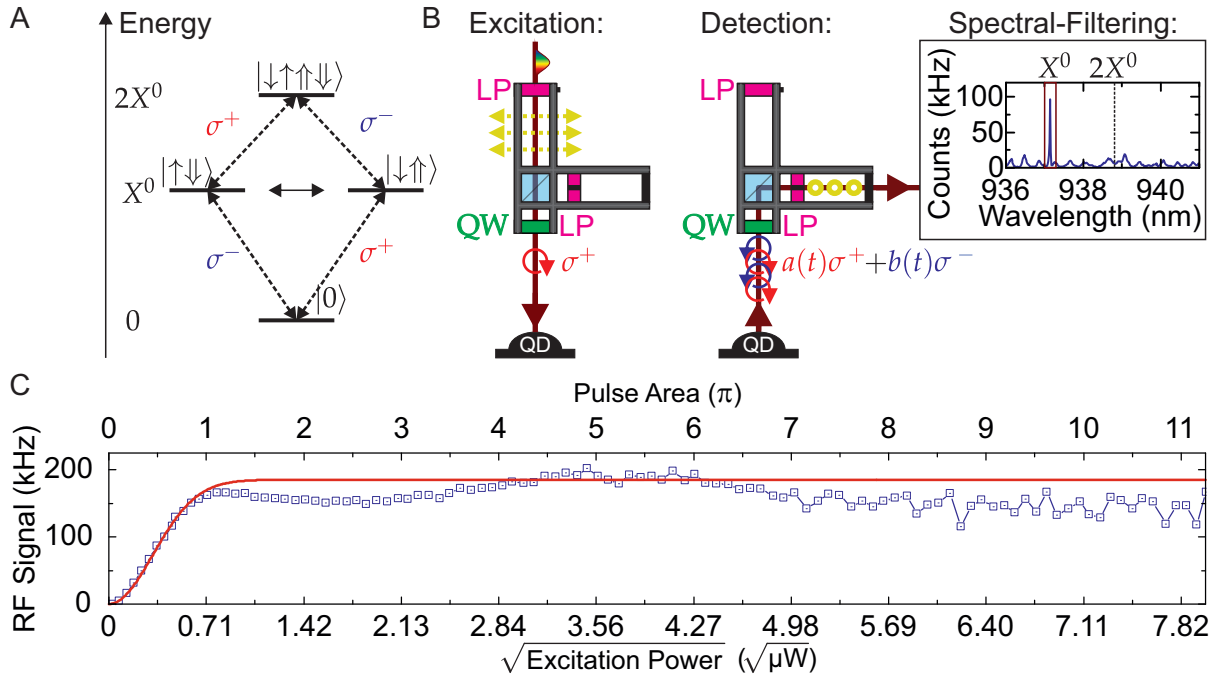

Figure 6.3.1: **Rapid adiabatic passage on a single self-assembled quantum dot. (A)** Energy level scheme of the quantum dot (QD): $|0\rangle$ represents the empty QD; $|1\rangle$ the spin-up exciton, $|1\rangle \equiv |\downarrow\Uparrow\rangle$. ($\uparrow$ ($\downarrow$) is a spin-up (spin-down) electron, $\Uparrow$ ($\Downarrow$) a spin-up (spin-down) hole) The transition $|0\rangle \leftrightarrow |\downarrow\Uparrow\rangle$ is driven with right-handed circularly polarised light (σ^+). The two exciton states, $|\downarrow\Uparrow\rangle$ and $|\uparrow\Downarrow\rangle$, are coupled via the fine structure which leads to a quantum beat $|\downarrow\Uparrow\rangle \leftrightarrow |\uparrow\Downarrow\rangle$. On creating $|\downarrow\Uparrow\rangle$ with a σ^+ polarised pulse results hence in both σ^+- and σ^- polarised emission. The biexciton state, $2X^0$, exists at higher energies but is not populated here. **(B)** Polarisation control in the dark-field microscope: the QD is excited with σ^+ polarised light; σ^- is detected. LP refers to a linear polariser, QW to a quarter-wave plate. The detected signal is spectrally filtered. This increases the signal to background ratio. **(C)** Resonance fluorescence versus pulse area (and square root of averaged excitation power P_{avg}) on a single, empty quantum dot. Plotted is the detected emission from the $|X^0\rangle \rightarrow |0\rangle$ transition following circularly polarised excitation pulses (blue squares). The originally transform limited pulses ($\tau = 80\,\text{fs}$) were positively chirped ($\phi_2 = 0.33\,\text{ps}^2$) to a pulse duration of 4 ps. The data are fitted to the Landau-Zener result (red line) with $A(1 - \exp(-c^2\tau\sqrt{\tau^4 + \phi_2^2}/\phi_2 * P_{\text{avg}})$ and reveal $c\sqrt{\tau} = 4.4 \pm 0.2\,\mu\text{W}^{-1/2}$ in agreement with independently estimated values from Rabi oscillations ($4.4 \pm 0.4\,\mu\text{W}^{-1/2}$). The parameter c includes the dipole transition moment and when multiplied with $\sqrt{\tau P_{\text{avg}}}$ gives the pulse area.

6.4 Discussion

Working with a two-level emitter depends on distinguishing the resonance fluorescence of the emitter from the laser light used to create it. Unlike fluorescence-based imaging there is a spectral overlap between signal and source. The techniques used here (crossed polarisation and spectral analysis) can be supplemented with more effective spectral filtering for individual emitters or a collection of close-to-identical emitters (the source is broadband, resonance fluorescence from an individual emitter is narrowband). Time-gating the detector could also be used to suppress the background laser signal: in this experiment the pulses are gone in ~ 50 ps yet the radiative lifetime is much larger, ~ 800 ps. With these improvements we believe that the technique can become a versatile one.

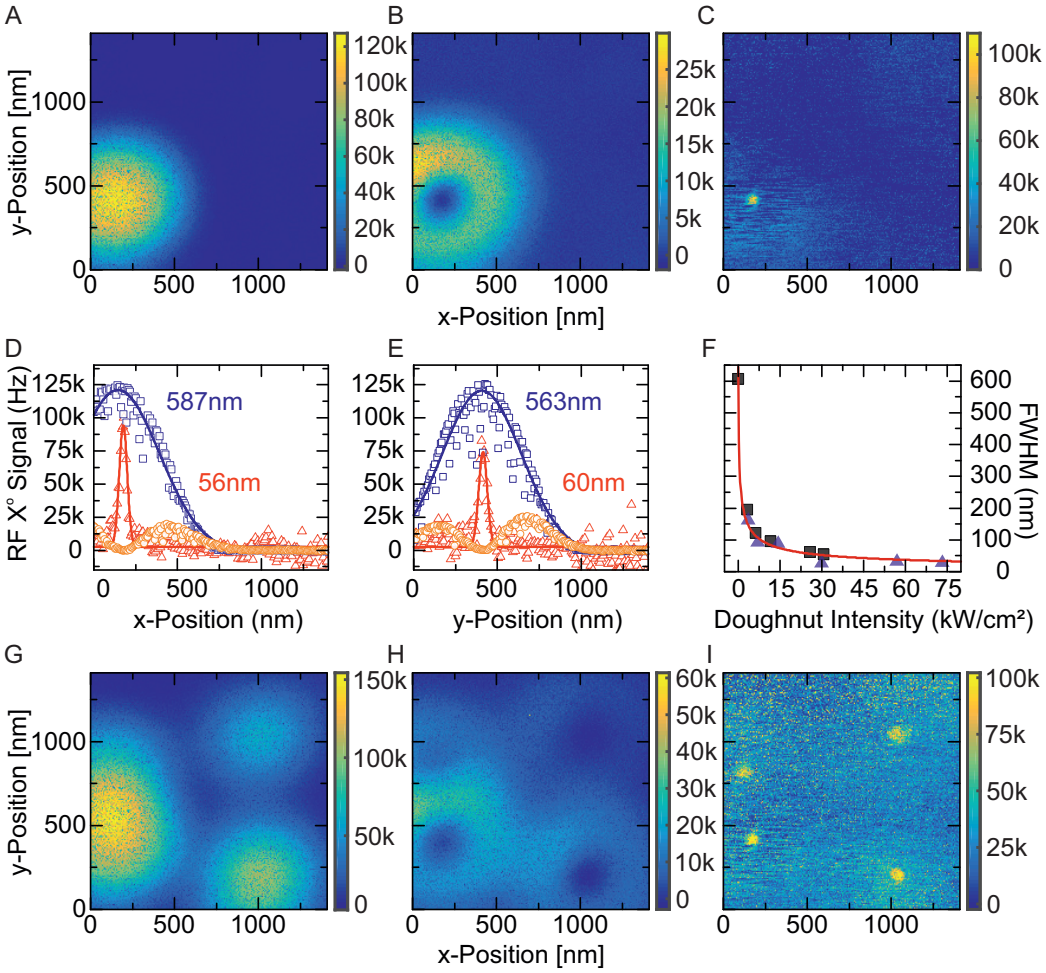

Figure 6.3.2: **Imaging an ensemble of quantum dots (QDs) with the RAP-based protocol. (A)-(C)** Resonance fluorescence as a function of sample position. The excitation intensities are stated in units of the threshold intensity $I_T = 0.28\,\mathrm{kW/cm^2}$. (A) Gauss-pulse only, intensity $I_G^0 = 1.2I_T$; (B) doughnut-pulse only, intensity $I_D^0 = 1.2I_T$; (C) Gauss-pulse $I_G^0 = 2.8I_T$ followed by doughnut-pulse $I_D^0 = 205I_T = 57\,\mathrm{kW/cm^2}$. Shown is the signal in a spectral window (wavelength bandwidth 0.05 nm) around the X^0 emission of one single QD. **(D)** and **(E)** show x and y line-cuts through the data in (A)-(C) in blue, orange and red, respectively. Solid lines are Gaussian fits to the blue and red data points. **(F)** Extracted full-width-at-half-maximum (FWHM) of the central image of a single QD as a function of the doughnut-pulse intensity I_D. Thereby, $I_G = 1.2I_T$ blue triangles, and $I_G = 2.8I_T$ black squares. The smallest FWHM achieved here is 30 nm. **(G)-(I)** Images, as (A)-(C), but adding the signal from four integration windows (each with a width in wavelength of 0.05 nm) demonstrating the multiplexing capability of the imaging scheme. The color scale in (I) is slightly over-saturated to increase the contrast for less bright QDs.

6.5 Materials and Methods

The InGaAs quantum dots are embedded in a GaAs n-i-p diode [25] and emit around 950 nm wavelength. The heterostructure is grown by molecular beam epitaxy. The collection efficiency is increased by incorporating a semiconductor Bragg mirror below the quantum dots in the heterostructure growth and by placing a solid immersion lens on the sample surface. Resonance fluorescence is distinguished from back-scattered laser light by a polarisation-based dark-field microscope [Kuhlmann et al., 2013a,b] and by spectrally-sensitive detection. The laser is a mode-locked Ti:sapphire laser and produces close-to-transform-limited pulses with a duration of ∼100 fs. The laser output is split into two beams, and two separate pulse-shapers introduce a controlled amount of chirp into the beams. One beam is delayed with respect to the other and then each beam is coupled into an optical fiber. The two optical fibers transport the beams to the two input ports of the microscope. Following collimation in the microscope, one of the beams passes through a 2π vortex phase plate. The two beams are then combined at a beam-splitter. The microscope objective, sample and nano-positioners are held at 4.2 K in a helium bath cryostat. On focussing, the beam with the phase-manipulated wavefront acquires a doughnut intensity profile. The doughnut maximum:minimum intensity ratio $> 1000:1$. The microscope objective has numerical aperture 0.68 and operates close to the diffraction limit. Images are recorded by sample scanning.

6.6 Supplementary Materials

6.6.1 The semiconductor sample

The heterostructure

The InGaAs quantum dots (QDs) are embedded in a GaAs n-i-p diode grown by molecular beam epitaxy [Prechtel et al., 2016]. The layer structure is shown in Fig. 6.6.1(A). Initially, a superlattice (18 periods of a 2 nm GaAs, 2 nm AlAs unit) is grown on top of a GaAs wafer in order to smooth the wafer surface. Following this, a distributed Bragg reflector (DBR) consisting of 16 periods of 68.6 nm GaAs and 81.4 nm AlAs is grown in order to increase the photon collection efficiency from the top side. The back contact is provided by a layer of n-doped GaAs. An intrinsic region, 30 nm of GaAs, acts as tunnel barrier for the InGaAs QDs. The QDs are capped by 153 nm GaAs. A subsequent barrier (a superlattice consisting of 46 periods of a 3 nm AlAs, 1 nm GaAs unit) hinders current flow in the strong vertical electric field. The penultimate layer is p-doped GaAs forming the top contact of the diode. Compared to a Schottky diode structure the absorption of photons in the top gate is reduced. The final layer, 44 nm undoped GaAs, places the p-doped layer around a node-position of the standing electromagnetic wave. The n- and p-doped layers are contacted independently. Selective etching of the capping allows contacting of the buried p-layer. Access to the n-layer is provided by wet etching of a mesa structure around the solid immersion lens (SIL). The n-contact is grounded; a voltage V_g is applied to the p-contact.

Quantum dot charging

The sample is probed at liquid helium temperature, 4.2 K, in a bath cryostat. At these temperatures, there is a pronounced Coulomb blockade: the number of electrons in the quantum dot changes step-wise as a function of V_g [Warburton et al., 2000; Dalgarno et al., 2008; Warburton, 2013]. Fig. 6.6.1(B) shows the photoluminescence (PL) of a single QD as function of V_g. There are plateaus with emission from the neutral exciton, X^0, from the negatively charged trion (two-electron, one-hole complex), X^{1-}, and from the X^{2-}. There is also a much weaker PL signal from the positively charged trion, X^{1+}, at the most negative V_g. The X^0 is used in the imaging experiments. We note that the V_g-overlap of the X^0-X^{1-} plateau is not a feature once the QD is driven with resonant excitation [Kurzmann et al., 2016].

Resonance fluorescence detection: CW excitation

Resonance fluorescence (RF), the scattering induced by resonant excitation, is shown in Fig. 6.6.1(C) on the X^0 transition. The laser excitation and the detection are orthogonally polarised in order to suppress reflected laser light in the detection channel: this is a polarisation-based dark-field technique [Kuhlmann et al., 2013b,a]. With our RF multi-purpose microscope, described in sec. 6.6.2, CW excitation, and a zirconia SIL on the sample surface, we reach a driving laser extinction ratio of 10^7:1 and a collection efficiency of approximately $5-10\%$. The net result is that the signal:background ratio is 250:1, e.g. Fig. 6.6.1(C). The X^0 transition is split into two, Fig. 6.6.1(C), as a consequence of the fine structure splitting, FSS (see Fig.

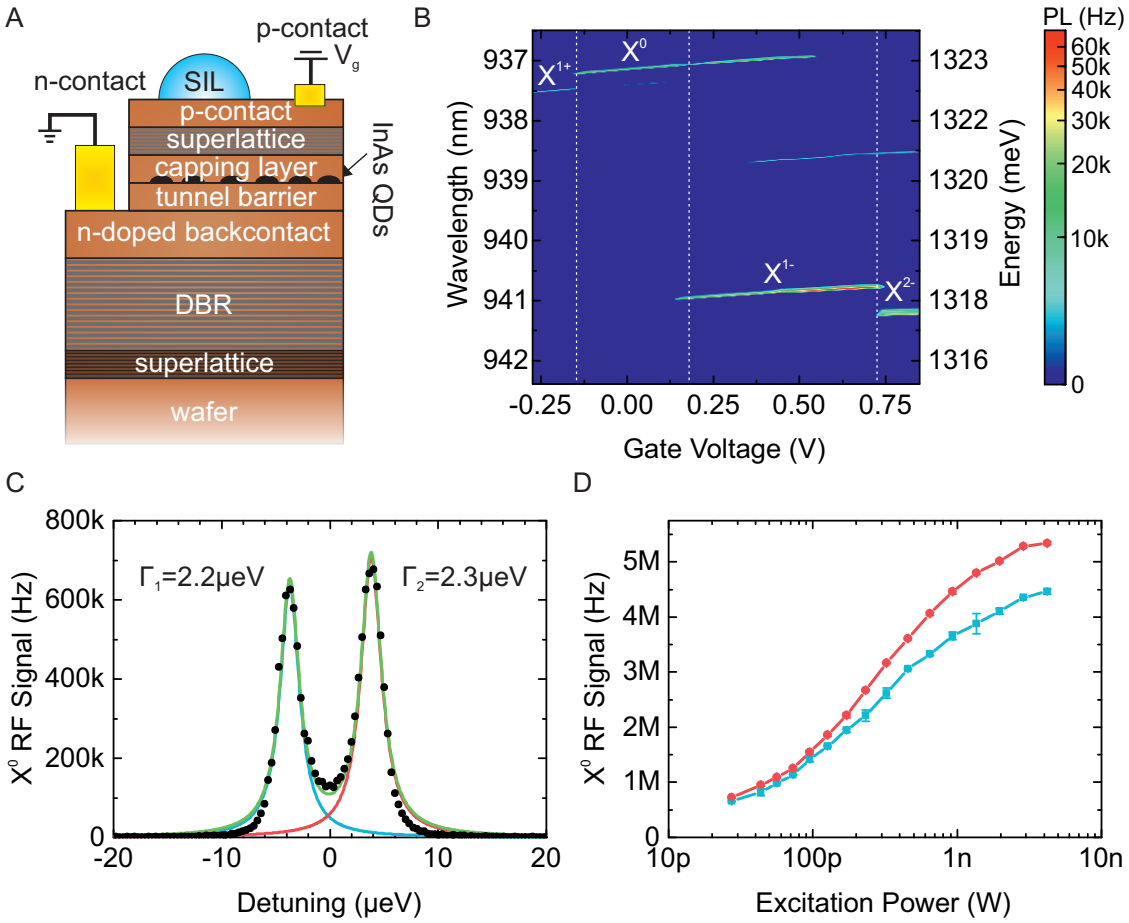

Figure 6.6.1: **Resonance fluorescence on a single quantum dot (QD): CW excitation. (A)** The heterostructure: InGaAs QDs in an n-i-p diode with weak cavity structure. In the growth direction: GaAs wafer, GaAs/AlAs superlattice (18 periods), distributed Bragg reflector (DBR) consisting of 16 GaAs/AlAs pairs, Si doped GaAs back contact, GaAs tunnel barrier, InGaAs QDs, capping layer, blocking barrier consisting of AlAs/GaAs superlattice, C-doped GaAs as top contact. A ZrO_2 solid immersion lens (SIL) is placed on the sample surface to increase the photon extraction efficiency. **(B)** Photoluminescence of a single QD, QD01, as a function of applied gate voltage and emission wavelength. The QD was excited non-resonantly at 830 nm with a power of 17 µW. **(C)** Resonance fluorescence spectrum of QD01 X^0 with resonant, circularly polarised excitation of 27 pW. The data (black circles) were fitted with a sum of two Lorentzian functions (green, individual functions shown in red and blue). The individual linewidths are 2.2 µeV and 2.3 µeV. The photons were detected with a silicon single photon avalanche diode with an integration time of 5 ms. The laser frequency was 319.778 62 THz (wavelength 937.530 nm). **(D)** Fitted amplitudes of resonance fluorescence as a function of excitation power for the two X^0 transitions.

6.3.1(A) of the main article). The linewidths are around 2 μeV, approximately 2.5 times larger than the transform limit [Kuhlmann et al., 2013b]. Above saturation, the RF is more than 5 MHz corresponding to a single photon flux of 25 MHz. The detector, a silicon single photon avalanche diode (SPAD), has a quantum efficiency of 20% at a wavelength of 950 nm.

6.6.2 The experiment

The imaging experiment consists of a laser system and a cryogenic optical microscope, Fig. 6.6.2. The laser is a tunable, mode-locked Ti:sapphire which creates close-to-transform-limited pulses with a pulse duration of ∼100 fs. The pulse train is expanded with a beam expander and split into two. The individual pulse trains are directed into compact pulse shaper units (PS1, PS2) which introduce chirp by introducing a wavelength dependent phase shift. Subsequently, one pulse is delayed with respect to the other in a 300 mm delay line,

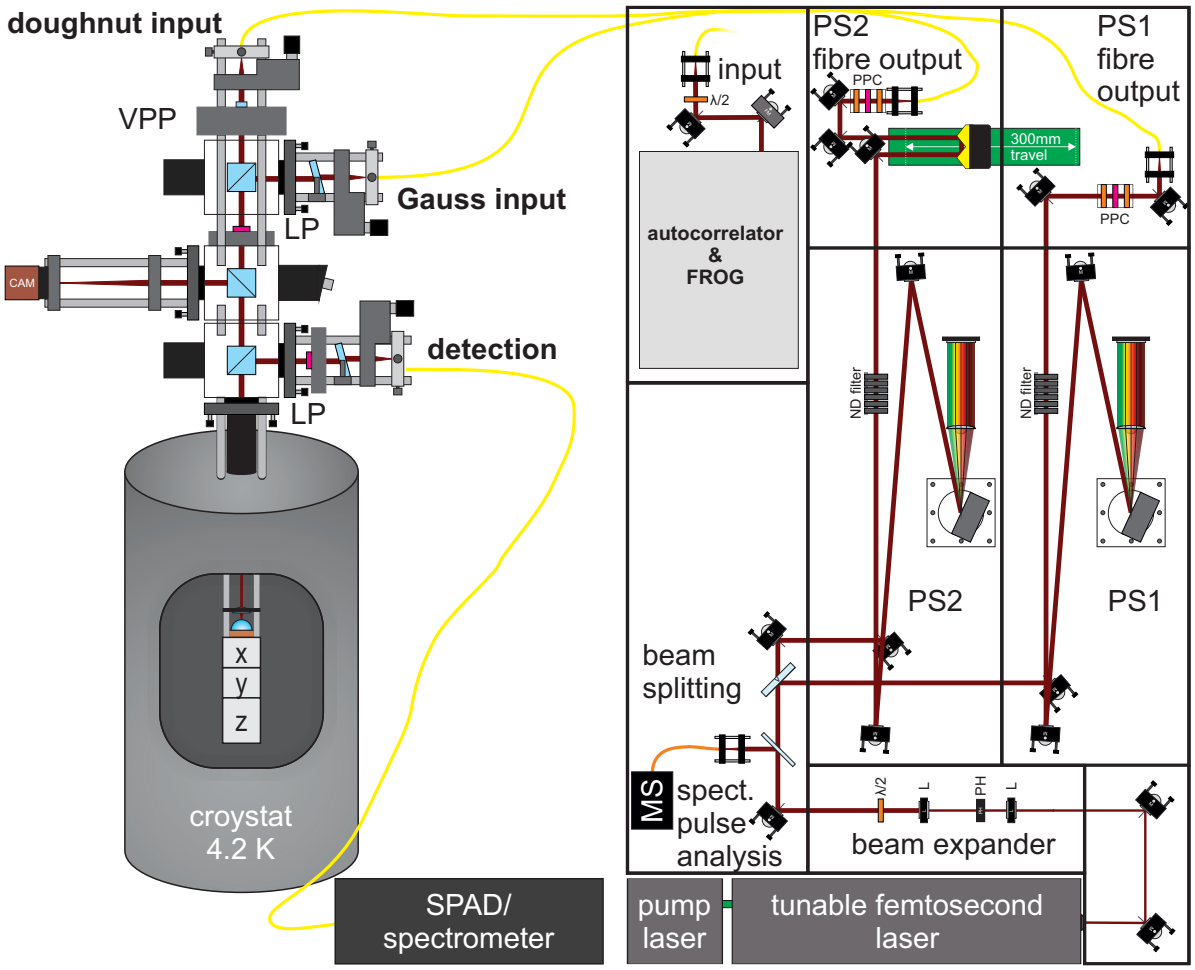

Figure 6.6.2: **Scheme of the whole experiment.** L lens, $\lambda/2$ half-wave plate, PH pin-hole, MS mini-spectrometer, PS pulse shaper, ND neutral density filter, PPC power-polarisation-control, FROG frequency-resolved-optical-gating, VPP vortex phase-plate, LP linear polariser, SPAD single photon avalanche diode. The autocorrelator-FROG combination is used to characterise the pulses before the microscope.

leading to a delay of up to 2 ns, and then power and polarisation are controlled (neutral density filters for coarse power control; a half-wave plate, polariser, half-wave plate combination for fine power control and control of the linear polarisation axis). Finally, the two pulse trains are coupled into separate single-mode optical fibers.

The microscope consists of the "head" at room temperature and an objective lens plus nano-positioners at low temperature, Fig. 6.6.2. The nano-positioners allow the sample to be positioned at the focus of the microscope, and images to be recorded by sample scanning. The head converts one pulse train into a collimated beam with a Gaussian intensity profile, the other into a collimated beam with a Gaussian intensity profile and azimuthal phase dependence. The two pulse trains are focused by the objective onto the sample with close to diffraction-limited performance, resulting in a Gauss-shaped focus and a doughnut-shaped focus. Resonance fluorescence is collected by the same objective and coupled in the microscope head into a third fiber which transports the signal to the detector, either a spectrometer-CCD camera system or a SPAD.

Creation and characterization of chirped pulses

A controlled chirp is introduced into the laser pulses using a compact, folded $4f$-pulse shaper [Weiner et al., 1992], Fig. 6.6.3(B). Our scheme retains all the frequency components of the femto-second laser. Introducing chirp inevitably results in an increased pulse duration.

An unchirped pulse is directed onto a grating and its first order diffraction is then focused by a cylindrical lens onto a mirror. The lens and mirror are mounted together on a platform which can be moved with respect

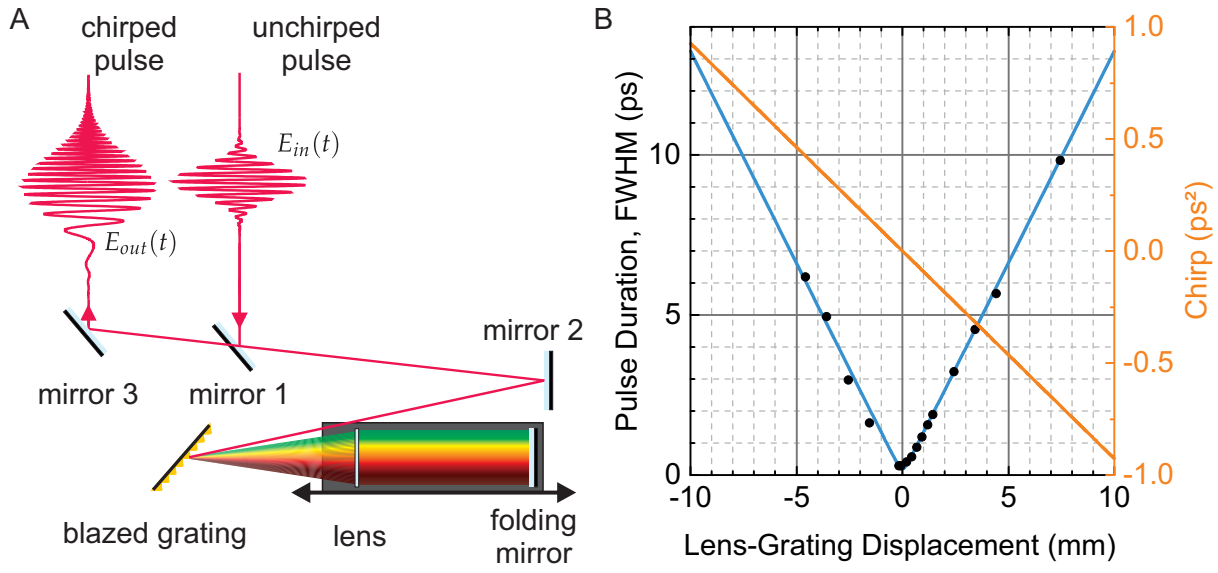

Figure 6.6.3: **Compact pulse shaper: concept and performance. (A)** The incident beam is directed with mirrors 1 and 2 onto a blazed grating (1,800 lines/mm), diffracted and then focused by a cylindrical lens (focal length 150 mm) onto a mirror placed in the focal plane of the lens. The lens and the folding mirror are mounted on a moving platform. A displacement (up to ±10 mm) between grating and lens–mirror assembly introduces chirp. Note that the beam is reflected slightly upwards by the mirror in the pulse shaper such that it overshoots mirror 1 on the return path. **(B)** Pulse duration $\Delta t^I_{\mathrm{FWHM}}$ as a function of the lens–grating displacement. The pulse duration was measured with a FROG autocorrelator. The measured data points (black circles) are fitted (blue solid line) using the result for quadratic phase, eq. 6.6.2b. The sweep rate α calculated from the pulse duration is shown on the right axis.

to the grating with a micrometer linear stage, Fig. 6.6.3(B). This allows a variation of the lens–grating separation while keeping the mirror in the focal plane of the lens. A lens–grating separation larger than the focal length (positive displacement) introduces a negative chirp, a separation smaller than the focal length (negative displacement) results in a positive chirp [Martinez, 1987]. We demonstrate in Fig. 6.6.3(B) a stretching of the original, transform-limited 130 fs pulses to a duration of more than 10 ps, an increase by a factor of 100.

The pulse duration is linked to the chirp. The electric field of the unchirped pulse can be described with a Gaussian envelope in the time domain:

$$\begin{aligned} E(t) =& E_0 \exp\left(\frac{-t^2}{2\tau_0^2} - i\omega_0 t\right) \\ \Delta t^I_{0,\mathrm{FWHM}} =& 2\sqrt{\ln 2}\,\tau_0 \end{aligned}$$

where $\Delta t^I_{0,\mathrm{FWHM}}$ is the full-width-at-half-maximum (FWHM) of the pulse intensity. $\Delta t^I_{0,\mathrm{FWHM}} = 130\,\mathrm{fs}$ here. Equivalently, the unchirped pulse can be described in the frequency domain:

$$\begin{aligned} E(\omega) =& E_0 \tau^2 \exp\left[-\frac{\tau_0^2}{2}(\omega-\omega_0)^2\right] \\ \Delta\omega^I_{0,\mathrm{FWHM}} =& \frac{2\sqrt{\ln 2}}{\tau_0}. \end{aligned}$$

The role of the pulse shaper is to add a phase for each frequency component:

$$\phi(\omega) = \phi_0 + \phi_1(\omega-\omega_0) + \frac{\phi_2}{2}(\omega-\omega_0)^2. \tag{6.6.1}$$

The linear phase term shifts the entire pulse in time and is irrelevant here; the quadratic term represents a chirp. In practice, ϕ_2 is directly proportional to the displacement of the pulse shaper [Weiner, 2009]. The

link between ϕ_2 and the new pulse duration τ is:

$$\tau = \sqrt{\tau_0^2 + \left(\frac{\phi_2}{\tau_0}\right)^2} \tag{6.6.2a}$$

$$\Delta t^I_{\mathrm{FWHM}} = \sqrt{\left(\Delta t^I_{0,\mathrm{FWHM}}\right)^2 + \left(\frac{\phi_2\ 4\ln 2}{\Delta t^I_{0,\mathrm{FWHM}}}\right)^2}. \tag{6.6.2b}$$

A key parameter for adiabatic passage is the sweep rate α. It is related to ϕ_2 by

$$\frac{\mathrm{d}}{\mathrm{d}t}\omega(t) = \alpha = \frac{\phi_2}{\tau_0^4 + \phi_2^2}. \tag{6.6.3}$$

We work here in the regime $\phi_2 \gg \tau_0^2$ such that $\tau \simeq \phi_0/\tau_0$ and $\alpha \simeq 1/\phi_2$.

The measured pulse duration as a function of displacement is shown in Fig. 6.6.3(B). The results can be described perfectly with a quadratic phase dependence, eq. 6.6.1, allowing us to determine the sweep rate from eq. 6.6.3. Our pulse shaper is capable of generating ϕ_2 up to a few ps^2 with both signs. With a transform limited pulse duration of 130 fs and a chirp range $0\,\mathrm{ps}^2$ to $1\,\mathrm{ps}^2$ we can reach sweep rates from $1\,\mathrm{ps}^{-2}$ to $80\,\mathrm{ps}^{-2}$. We note that the 8 m long single mode fibers used to transport the laser pulses to the microscope in our experiment, Fig. 6.6.2, introduce a positive chirp of $0.3 \pm 0.1\,\mathrm{ps}^2$: this is compensated with our pulse shaper.

Microscope design

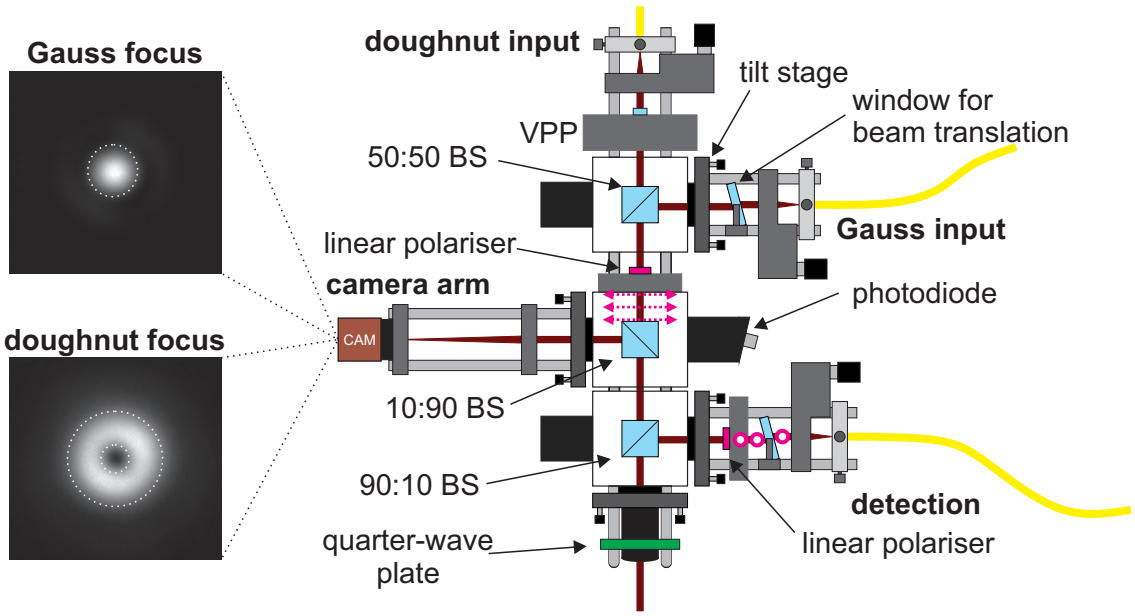

Figure 6.6.4: **Microscope optics.** CAM camera, BS beam-splitter.

The microscope is based on a former version of an RF confocal microscope [Kuhlmann et al., 2013a]. The "head", Fig. 6.6.4, accepts two fiber inputs. In each input, the exact propagation axis is controlled (by rotating a laser window and a tilt stage) and a linear polarisation state created (by a high quality polariser) after the two beams are combined by a beam-splitter and sent to the objective at low temperature. One input passes through a 2π vortex phase-plate (VPP). The VPP introduces a phase shift to the wavefront: the phase shift is equal to the in-plane radial angle. On focusing, a doughnut intensity profile results. The fiber output collects the back-scattered signal. A camera provides an in situ image: it assists in positioning the sample surface with respect to the focus, and in co-aligning the three beams (two inputs, one output). The objective is a single element aspheric lens with numerical aperture $\mathrm{NA_O} = 0.68$ which, with CW laser input, can operate at close to the diffraction limit at these wavelengths.

Reflected laser light is suppressed by exciting and detecting in orthogonal polarisations, either in a linear polarisation basis as in previous experiments [Kuhlmann et al., 2013b,a], or, as a new feature here, in a

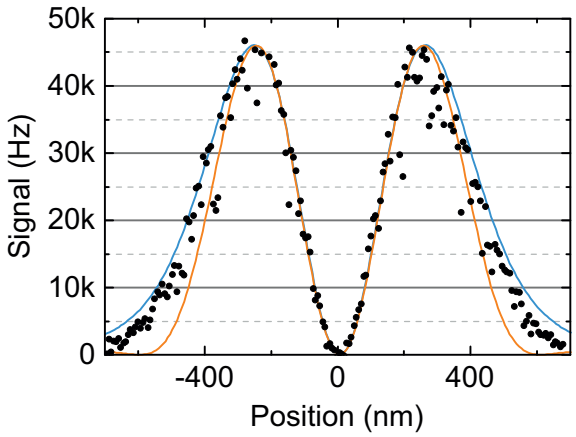

Figure 6.6.5: **Quality of the doughnut focus.** The doughnut-shaped focus was measured with a quantum dot and left circularly polarised excitation, data points (black circles) are taken from the white dashed line in Fig. 6.6.10. Also shown are calculated foci for a Gaussian (blue solid line) and plane wave (orange solid line) incident on the objective, $|E_{\mathrm{D}}|^2$ with E_{D} from eq. 6.6.4b. Parameters for the calculation are $\lambda = 940\,\mathrm{nm}$, $n_{\mathrm{SIL}} = 2.13$, $\Delta X_{I,\mathrm{FWHM}} = 2.0\,\mathrm{mm}$ ($\sigma = 1.2\,\mathrm{mm}$), $f = 5.9\,\mathrm{mm}$.

circular basis. We can make this choice by choosing the angle of a quarter wave-plate through which all beams pass, inserted as the final component in the microscope head. The extinction factor for the reflected laser light depends strongly on the quality of the focal spot. On a bare piece of GaAs we typically reach extinction ratios of 10^8:1; under a SIL on GaAs with CW excitation we reached in this experiment 10^7:1; and with excitation pulses, the single element aspheric lens, and a SIL on GaAs the ratio decreases to 10^5:1. The performance worsens with pulsed excitation because of the spectral bandwidth of the laser pulses: the aspheric lens introduces a slight chromatic aberration.

The quality of the microscope's focus is tested by imaging a chrome grid with confocal detection in reflection. With femto-second laser pulses with center wavelength $\lambda = 940\,\mathrm{nm}$, we measured in this test experiment $\Delta x = 388 \pm 3\,\mathrm{nm}$ which is close to the diffraction limit.

The quality of the doughnut-shaped focus is crucial for the imaging experiment: a low quality reduces the intensity of the central bright spot. We define quality here as the intensity ratio of the doughnut's maximum to its minimum: it quantifies the relative residual intensity in the center, Fig. 6.6.5. Measured on a QD with left circularly polarised excitation we reached values of 1200:1, a factor of about five higher than in right circularly polarised excitation. The dependence of the quality on the helicity of the polarisation (with respect to the VPP) is in agreement with vector-field calculations [Hao et al., 2010] and reported experimental results on fluorescent nanoparticles [Neupane et al., 2013]. With the correct choice of the helicity the residual intensity at the center is very small in this experiment [Neupane et al., 2013; Bokor et al., 2005].

The microscope is simple to operate and robust: once aligned it remains aligned over several days.

Resonance fluorescence detection: pulsed excitation

The femto-second pulses are spectrally broad: they contain the frequencies to excite not just the neutral exciton, X^0, but also the biexciton, $2X^0$ and the trions, X^{1-} and X^{1+}, should the ultra-short laser pulses disrupt the Coulomb blockade. These concerns turn out to be unfounded. With a circularly polarised pulsed excitation, the RF from a single quantum dot lies almost entirely at the X^0 emission frequency, Fig. 6.6.6. The shift in emission frequency as a function of V_g reflects the dc Stark effect.

For chirped excitation with sufficient intensity to invert the system, equivalently for a π pulse with unchirped excitation, the RF:background ratio is $11:1$. At higher laser power, the background rises but the signal does not and the background signal dominates. We deal with this in two ways. First, the laser background is spectrally broad, the RF spectrally narrow, 5,000-times narrower in fact. We therefore collect the signal in a small spectral "window", typically a sub-nanometer wavelength extent. We do this simply by reading out the appropriate pixels on the CCD camera. In this way, only the laser background in a narrow bandwidth adds to the signal. Secondly, we measure the remaining laser background by recording the signal when the quantum dot is turned off. We implement this by recording a signal at two different values of

V_g: V_g^{on} and V_g^{off}. This is a simple modulation technique and is robust with respect to any changes in the performance of the microscope. The only complication in this procedure is a slight shift of V_g^{on} as a function of excitation power: this arises because a small amount of space charge is trapped in the device and shifts the X^0 resonance. Since the excitation power is constant during a scan in the imaging experiment, here the simple modulation technique is sufficient. Other experiments (main paper, Fig. 6.3.1(C)) are performed as a function of pulse area. We therefore record here the signal-plus-background in a small gate voltage range around the X^0 resonance. The signal is then extracted from a path following the slight shift of the resonance, the background is determined from the same dataset and the same path but shifted in V_g with respect to the resonance, Fig. 6.6.6(C). This procedure enables us to determine the RF signal even at very large laser powers, corresponding to a pulse area up to 11π. The laser background contributes additional shot noise to the noise in the RF signal; there is also a systematic error which we estimate to be 20% of the signal at the highest laser powers, arising from weak interference effects of the two pulses in the imaging experiment and from a slight dependence in the choice of X^0 spectral bandwidth.

6.6.3 Imaging of two-level system with adiabatic passage: model

We construct a simple model of nanoscopic imaging of a quantum mechanical two-level system. The aim is to capture the essential features and to generate analytical results.

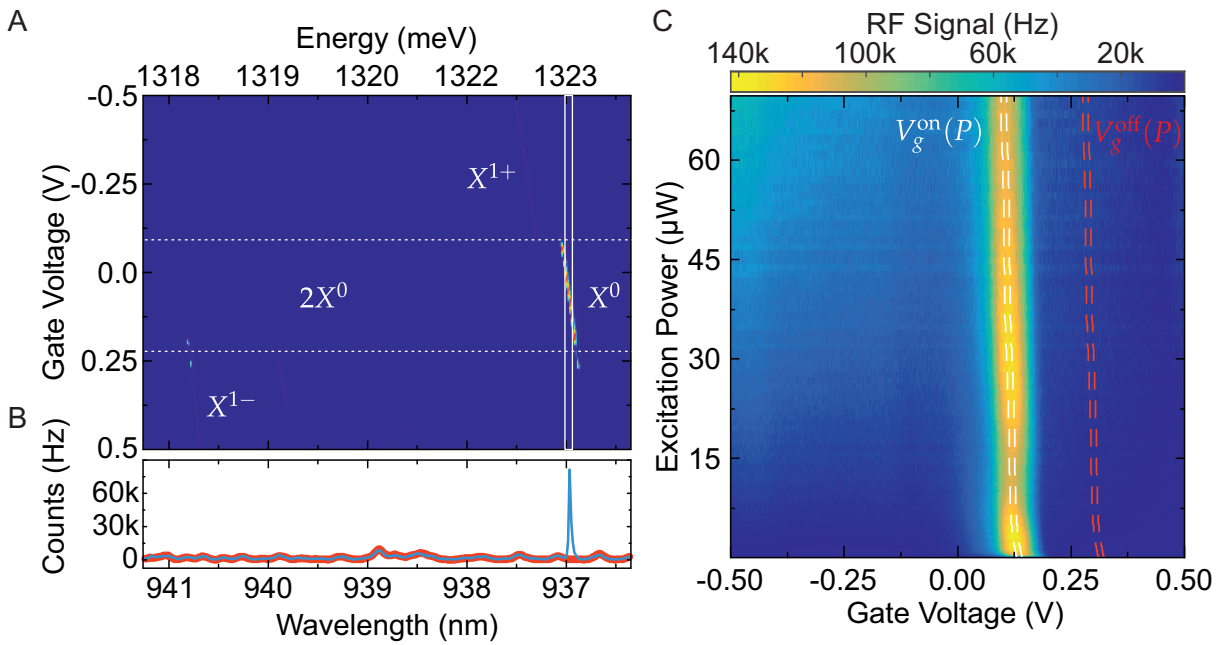

Figure 6.6.6: **Resonance fluorescence (RF) on a single quantum dot: pulsed excitation.** RF with positively chirped excitation pulses of a spectral and temporal width of $\Delta\lambda^I_{\text{FWHM}} = 9.70 \pm 0.30\,\text{nm}$ and $\Delta t^I_{\text{FWHM}} = 7.0 \pm 0.3\,\text{ps}$, respectively. The polarisation was right circular, the integration time per spectrum 25 ms. **(A)** Signal following background subtraction (see (B)) as a function of applied gate voltage V_g and detection wavelength for an excitation power of 0.36 µW. The detection of RF from X^{1-}, X^{1+} and $2X^0$ after circularly polarised excitation is weak due to the cross polarised dark-field technique and the selection rules. **(B)** Signal versus wavelength: raw data at $V_g = 120\,\text{mV}$ (blue line). The laser background is determined from the whole dataset in (A): for every wavelength the V_g with the smallest count rate is determined and this count rate is used to construct the laser background spectrum (red curve). Note that the laser suppression function is a quadratic function of wavelength about the alignment wavelength, superimposed with interference fringes. **(C)** Spectrally integrated RF from the white solid rectangle in (A) as a function of excitation power P and gate voltage. The final signal is the difference between the signal on the white dashed path, $V_g^{\text{on}}(P)$, and the remaining background on the red dashed path, $V_g^{\text{off}}(P)$.

The optical fields: scalar theory

We calculate the field distribution in the focal plane using scalar diffraction theory applied to Gaussian beams. Strictly speaking, at high numerical apertures a full vector theory is required; additionally the beams are truncated Gaussians, truncated by the aperture of the objective lens. Extending the calculation to arbitrary input beams with a full vector theory is not difficult. The present approach has the virtue of simplicity.

In scalar theory, the electric field in the focal plane has the same polarisation as the input polarisation. The spatial distribution of the electric field in the focal plane is proportional to the Fourier transform of the (normalized) aperture function, $A(R,\phi)$, where (R,ϕ) are the radial coordinates in the plane of the aperture. For the Gaussian and doughnut beams

$$\begin{aligned} A_{\mathrm{G}}(R,\phi) =& \frac{1}{2\pi\sigma^2}\exp\left(-\frac{R^2}{2\sigma^2}\right) \\ A_{\mathrm{D}}(R,\phi) =& A_{\mathrm{G}}(R,\phi)\, e^{i\phi} \end{aligned}$$

where σ describes the spatial extent of the beams before the focusing, $\Delta X_{I,\mathrm{FWHM}} = 2\sqrt{\ln 2}\,\sigma$. The fields in the focal plane (x,y) are given by

$$\begin{aligned} E_{\mathrm{G}}(r) &= E_{\mathrm{G}}^0 \int_{R=0}^{\infty}\int_{\phi=0}^{2\pi} A_{\mathrm{G}} \exp\left(-ik\frac{r}{f}R\cos\phi\right) R\,\mathrm{d}R\,\mathrm{d}\phi \\ E_{\mathrm{D}}(r) &= E_{\mathrm{D}}^0 \int_{R=0}^{\infty}\int_{\phi=0}^{2\pi} A_{\mathrm{D}} \exp\left(-ik\frac{r}{f}R\cos\phi\right) R\,\mathrm{d}R\,\mathrm{d}\phi \end{aligned}$$

where $r = \sqrt{x^2+y^2}$ is the radial coordinate in the focal plane, $k = 2\pi/(\lambda/n_{\mathrm{SIL}})$, f is the focal length of the lens, and E_{G}^0 (E_{D}^0) is the amplitude of the Gauss (doughnut) beam.

$$E_{\mathrm{G}}(r) = E_{\mathrm{G}}^0 \exp\left(-\frac{k^2\sigma^2 r^2}{2f^2}\right) \tag{6.6.4a}$$

$$\begin{aligned} E_{\mathrm{D}}(r) = E_{\mathrm{D}}^0 i\frac{\sqrt{\pi}}{2\sqrt{2}}\frac{k\sigma r}{f}\exp\left(-\frac{k^2\sigma^2 r^2}{4f^2}\right) \\ \cdot\left[I_0\left(\frac{k^2 r^2\sigma^2}{4f^2}\right) - I_1\left(\frac{k^2 r^2\sigma^2}{4f^2}\right)\right]. \end{aligned} \tag{6.6.4b}$$

I_0 and I_1 are Bessel functions of the first kind with order 0 and 1, respectively. $E_{\mathrm{G}}(x,y)$ and $E_{\mathrm{D}}(x,y)$ are functions of (x,y) and have a Gaussian and a doughnut shape, respectively. The corresponding intensity distributions are depicted in Fig. 6.6.7. The FWHM of the Gaussian intensity distribution is $\Delta x_{I,\mathrm{FWHM}} = 2\sqrt{\ln 2}\; f/(k\sigma)$. $E_{\mathrm{D}}(r)$ is zero at $r = 0$.

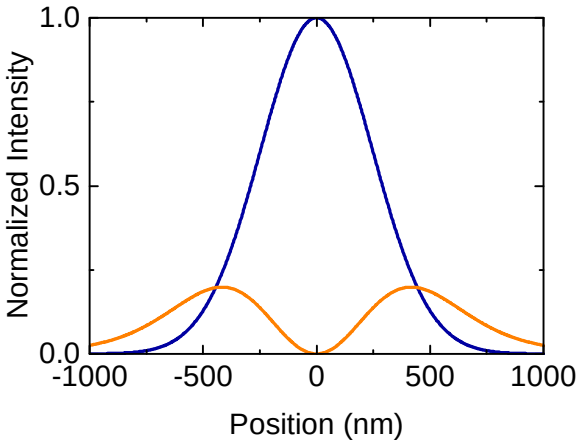

Figure 6.6.7: **Gauss and doughnut intensity distribution.** $|E_{\mathrm{G}}(x,y=0)|^2$ and $|E_{\mathrm{D}}(x,y=0)|^2$ in eq. 6.6.4 are plotted with $E_{\mathrm{G}}^0 = E_{\mathrm{D}}^0 = 1$ in blue and orange, respectively. Parameters for the calculation are $\lambda = 940\,\mathrm{nm}$, $n_{\mathrm{SIL}} = 2.13$, $\Delta X_{I,\mathrm{FWHM}} = 2.0\,\mathrm{mm}$ ($\sigma = 1.2\,\mathrm{mm}$), $f = 5.9\,\mathrm{mm}$.

Adiabatic passage: the Landau–Zener model

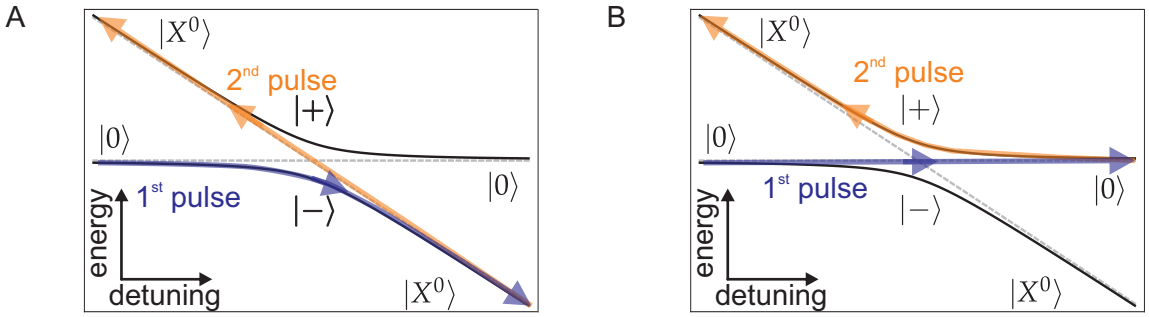

Figure 6.6.8: **Two-pulse adiabatic passage on a two-level system.** The eigenenergies are plotted as a function of detuning. Two possible paths, (A) and (B), show the two routes by which the system starts in the lower state $|0\rangle$ and ends up in the upper state $|1\rangle$ after a two pulse sequence. **(A)** Adiabatic passage followed by tunnelling; **(B)** tunnelling followed by adiabatic passage.

The case of a driven two-level system with time-dependent detuning was considered a long time ago by Landau [Landau, 1932] and by Zener [Zener, 1932]. Initially, the system is in one of the basis states, $|0\rangle$ or $|1\rangle$, and the detuning of the drive is large and negative. The detuning is then increased at a fixed rate passing through zero until it is large and positive. As a function of detuning, there is an avoided crossing in the eigenvalues, Fig. 6.6.8. The probability that the system makes a transition from one basis state to the other is given by the Landau–Zener factor, p_{LZ}:

$$p_{\mathrm{LZ}}(\Omega,\alpha) = \exp\left(-\frac{\pi\Omega^2}{2\,|\alpha|}\right)$$

where Ω is the angular Rabi frequency, α the sweep rate (rate of change of the angular frequency). Here, the coupling arises from the interaction of the optical dipole μ_{01} with the electric field of the light wave, $\hbar\Omega = \mu_{01}E$. In the "sudden" regime when $p_{\mathrm{LZ}} \simeq 1$, the system "tunnels" through the avoided crossing and $|0\rangle \to |0\rangle$, $|1\rangle \to |1\rangle$. Alternatively, in the limit when $p_{\mathrm{LZ}} \ll 1$, the states are swapped $|0\rangle \to |1\rangle$, $|1\rangle \to |0\rangle$: this is adiabatic passage, Fig. 6.6.8. The imaging protocol exploits the exponential dependence of $p_{\mathrm{LZ}}(\Omega,\alpha)$ on Ω for fixed α: there is a fast transition from the sudden regime to the adiabatic passage regime as Ω increases.

In our case here, the excitation is not just chirped but also pulsed. In other words, Ω is a function of time which is not a feature of the Landau–Zener model. However, the Landau–Zener model captures the essential physics. The Rabi energies are at most a few meV in these experiments yet the spectral bandwidth of the pulse is ~ 15 meV. The peak of the laser spectrum is chosen to lie close to the X^0 transition. This means that in the region of the avoided crossing, the Rabi frequency is approximately constant in time, such that the Landau–Zener model is a reasonable one to describe the experiment. Of course, it is possible to integrate the Schrödinger equation over the pulse [Simon et al., 2011]. The advantage of the Landau–Zener model is that there is a simple analytical result.

The imaging experiment depends on the response to two pulses, the Gauss-pulse (Rabi coupling Ω_{G}, chirp α_{G}) and the doughnut-pulse (Rabi coupling Ω_{D}, chirp α_{D}). Ω_{G} and Ω_{D} depend on the lateral coordinates (x,y) in the focal plane: this enables imaging. In practice, $\alpha_{\mathrm{G}} > 0$, $\alpha_{\mathrm{D}} = -\alpha_{\mathrm{G}}$. The system is initially in the ground state, $|0\rangle$. There are two possible routes for the system to end up in the excited state, $|1\rangle$, Fig. 6.6.8. (In practice in the experiment, $|1\rangle \equiv |X^0\rangle$.) Adding together the probabilities, the probability of occupying state $|1\rangle$ with the two-pulse combination is

$$\begin{aligned} P_1(\Omega_{\mathrm{G}},\alpha_{\mathrm{G}},\Omega_{\mathrm{D}},\alpha_{\mathrm{D}}) = \quad & p_{\mathrm{LZ}}(\Omega_{\mathrm{G}},\alpha_{\mathrm{G}}) + p_{\mathrm{LZ}}(\Omega_{\mathrm{D}},\alpha_{\mathrm{D}}) \\ & -2p_{\mathrm{LZ}}(\Omega_{\mathrm{G}},\alpha_{\mathrm{G}})\,p_{\mathrm{LZ}}(\Omega_{\mathrm{D}},\alpha_{\mathrm{D}}). \end{aligned}$$

The probability that the two-level system emits a photon following the two-pulse combination is P_1. The probability that the photon is detected is the point-spread-function of the detection channel, a Gaussian function centerd at $(x,y) = (0,0)$ (the square of eq. 6.6.4a), multiplied by a constant factor β, the efficiency

of the entire microscope–detector system. We arrive at an analytical result for the imaging signal:

$$\begin{aligned} \mathrm{RF}(x,y) =& \beta\, P_1(\Omega_\mathrm{G}, \alpha_\mathrm{G}, \Omega_\mathrm{D}, \alpha_\mathrm{D}) \\ & \cdot \exp\left(-\frac{k^2\sigma^2(x^2+y^2)}{f^2}\right) \end{aligned} \tag{6.6.5}$$

The RF function is plotted in Fig. 6.6.9 as a function of (x, y) for three different values of Ω_G^0 and three different values of Ω_D^0. For large Ω_G^0, a bright spot appears at $(x, y) = (0, 0)$ whose width decreases as Ω_D^0 increases: this describes the main modus operandi of the imaging scheme. At intermediate Ω_G^0, a ring appears surrounding the central maximum. The ring appears at locations where the Gauss beam leaves part of the population in state $|0\rangle$, and the doughnut beam transfers part of this population into state $|1\rangle$, resulting in a weak residual signal. As Ω_G^0 increases the ring moves to larger radii in the focal plane and it weakens: it can be suppressed in practice simply by choosing a large enough Gauss beam intensity.

In the limit of large Ω_G^0 and Ω_D^0, it is possible to derive a result for the FWHM of the central maximum, Δx_FWHM. We assume that Ω_G^0 is large enough such that $p_\mathrm{LZ}(\Omega_\mathrm{G}) \simeq 1$ over the central bright spot. Expanding the doughnut field $E_\mathrm{D}(x, y)$ as a Taylor series in (x, y) and retaining only the linear term, we find

$$\Delta x_\mathrm{FWHM} = \frac{\Delta x^0_{I,\mathrm{FWHM}}}{\sqrt{1+\pi^2(\Omega_\mathrm{D}^0)^2/16\alpha}}$$

This has the same dependence on the doughnut beam intensity as the STED protocol [Harke et al., 2008].

As a final point, we note that the response to the doughnut beam alone can exhibit a radial asymmetry, Fig. 6.6.10. This arises as a consequence of a small displacement of the doughnut zero with respect to the collection point-spread-function. By introducing a small displacement in the model, we can reproduce the experimental results convincingly, Fig. 6.6.10. Likewise, the ring in the calculated $\mathrm{RF}(x, y)$ function for intermediate Ω_G^0 also becomes radially asymmetric in the presence of this displacement. However, in the main imaging regime, the central bright spot lies at the central zero of the doughnut beam and is only very weakly influenced by a lateral displacement of the Gauss beam, equivalently the collection point-spread-function. The main experimental requirement is therefore to create a high quality doughnut beam.

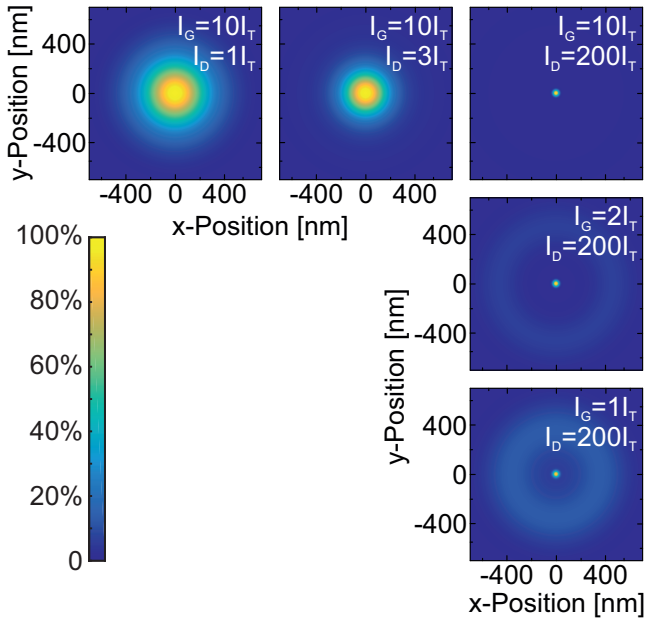

Figure 6.6.9: **Calculated images.** The function $\mathrm{RF}(x, y)$, eq. 6.6.5, is plotted for $\lambda = 940\,\mathrm{nm}$, $n_\mathrm{SIL} = 2.13$, $\Delta X_{I,\mathrm{FWHM}} = 2.0\,\mathrm{mm}$ ($\sigma = 1.2\,\mathrm{mm}$), $f = 5.9\,\mathrm{mm}$, $\alpha_\mathrm{G} = -\alpha_\mathrm{D} = 3.24\,\mathrm{ps}^{-2}$. For large Gauss beam intensity, the central spot decreases in size retaining the maximum signal as the doughnut beam intensity increases. For large doughnut beam intensity, a ring surrounds the central spot at small Gauss beam intensity. The ring weakens and moves to larger radii as the Gauss beam intensity increases.

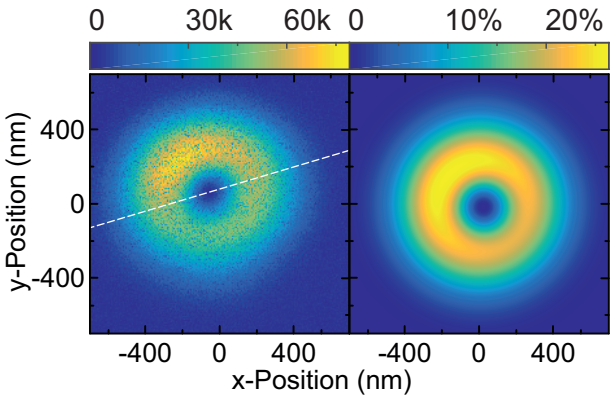

Figure 6.6.10: **Doughnut beam displacement.** Left: Resonance fluorescence from quantum dot QD01 measured with the doughnut-shaped pulse alone and left circularly polarised excitation. The excitation intensity was $I_D^0 = 1.2 I_T$. A cut along the white dashed line is plotted in Fig. 6.6.5. Right: corresponding simulation with $I_D^0 = 1.2 I_T$, parameters as stated in Fig. 6.6.9 and a displacement of $\Delta x_D = 20\,\mathrm{nm}$ and $\Delta y_D = -20\,\mathrm{nm}$.

Bibliography

L. C. Allen, J. H. Eberly, and L. Allen. *Optical Resonance and Two-Level Atoms (Dover Books on Physics)*. Dover Publications, new edition, 12 1988. ISBN 9780486655338.

P. L. Ardelt, L. Hanschke, K. A. Fischer, K. Müller, A. Kleinkauf, M. Koller, A. Bechtold, T. Simmet, J. Wierzbowski, H. Riedl, G. Abstreiter, and J. J. Finley. Dissipative preparation of the exciton and biexciton in self-assembled quantum dots on picosecond time scales. *Phys. Rev. B*, 90(24):241404, 2014.

M. Bayer, A. Kuther, A. Forchel, A. Gorbunov, V. B. Timofeev, F. Schäfer, J. P. Reithmaier, T. L. Reinecke, and S. N. Walck. Electron and Hole g Factors and Exchange Interaction from Studies of the Exciton Fine Structure in $In_{0.60}Ga_{0.40}As$ Quantum Dots. *Phys. Rev. Lett.*, 82:1748–1751, Feb 1999. doi:10.1103/PhysRevLett.82.1748.

M. Bayer, G. Ortner, O. Stern, A. Kuther, A. A. Gorbunov, A. Forchel, P. Hawrylak, S. Fafard, K. Hinzer, T. L. Reinecke, S. N. Walck, J. P. Reithmaier, F. Klopf, and F. Schäfer. Fine structure of neutral and charged excitons in self-assembled In(Ga)As/(Al)GaAs quantum dots. *Phys. Rev. B*, 65(19):195315, may 2002. ISSN 0163-1829. doi:10.1103/PhysRevB.65.195315.

E. Betzig, G. H. Patterson, R. Sougrat, O. W. Lindwasser, S. Olenych, J. S. Bonifacino, M. W. Davidson, J. Lippincott-Schwartz, and H. F. Hess. Imaging Intracellular Fluorescent Proteins at Nanometer Resolution. *Science*, 313(5793):1642–1645, sep 2006. ISSN 0036-8075. doi:10.1126/science.1127344.

N. Bokor, Y. Iketaki, T. Watanabe, and M. Fujii. Investigation of polarization effects for high-numerical-aperture first-order Laguerre-Gaussian beams by 2D scanning with a single fluorescent microbead. *Opt. Express*, 13(26):10440, 2005. ISSN 1094-4087. doi:10.1364/OPEX.13.010440.

S. Bounouar, M. Müller, A. M. Barth, M. Glässl, V. M. Axt, and P. Michler. Phonon-assisted robust and deterministic two-photon biexciton preparation in a quantum dot. *Phys. Rev. B*, 91(16):161302, 2015. ISSN 1550235X. doi:10.1103/PhysRevB.91.161302.

S. Bretschneider, C. Eggeling, and S. W. Hell. Breaking the diffraction barrier in fluorescence microscopy by optical shelving. *Phys. Rev. Lett.*, 98(21):1–4, 2007. ISSN 00319007. doi:10.1103/PhysRevLett.98.218103.

K. Brunner, G. Abstreiter, G. Böhm, G. Tränkle, and G. Weimann. Sharp-Line Photoluminescence and Two-Photon Absorption of Zero-Dimensional Biexcitons in a GaAs/AlGaAs Structure. *Phys. Rev. Lett.*, 73(8):1138–1141, aug 1994. ISSN 0031-9007. doi:10.1103/PhysRevLett.73.1138.

Coherent. *Operator's Manual The Coherent Mira 900-F Laser*. Coherent, Sanata Clara, CA, 2004.

P. A. Dalgarno, J. M. Smith, J. McFarlane, B. D. Gerardot, K. Karrai, A. Badolato, P. M. Petroff, and R. J. Warburton. Coulomb interactions in single charged self-assembled quantum dots: Radiative lifetime and recombination energy. *Phys. Rev. B*, 77(24):245311, 2008. ISSN 1098-0121. doi:10.1103/PhysRevB.77.245311.

A. Debnath, C. Meier, B. Chatel, and T. Amand. Chirped laser excitation of quantum dot excitons coupled to a phonon bath. *Phys. Rev. B*, 86:161304, 2012.

A. Debnath, C. Meier, B. Chatel, and T. Amand. High-fidelity biexciton generation in quantum dots by chirped laser pulses. *Phys. Rev. B*, 88(20):201305, nov 2013. ISSN 1098-0121. doi:10.1103/PhysRevB.88.201305. URL `http://link.aps.org/doi/10.1103/PhysRevB.88.201305`.

H. Drexler, D. Leonard, W. Hansen, J. P. Kotthaus, and P. M. Petroff. Spectroscopy of quantum levels in charge-tunable InGaAs quantum dots. *Phys. Rev. Lett.*, 73(16):2252–2255, 1994. ISSN 00319007. doi:10.1103/PhysRevLett.73.2252.

M. Ediger, P. A. Dalgarno, J. M. Smith, B. D. Gerardot, R. J. Warburton, K. Karrai, and P. M. Petroff. Controlled generation of neutral, negatively-charged and positively-charged excitons in the same single quantum dot. *Appl. Phys. Lett.*, 86(21):211909, 2005. doi:10.1063/1.1937996.

M. Fox. *Quantum optics: an introduction*. Oxford University Press, Oxford New York, 2006. ISBN 9780198566731.

M. Fox. *Optical properties of solids*. Oxford University Press, Oxford New York, 2010. ISBN 0199573379.

D. Gammon, E. S. Snow, B. V. Shanabrook, D. S. Katzer, and D. Park. Fine Structure Splitting in the Optical Spectra of Single GaAs Quantum Dots. *Phys. Rev. Lett.*, 76(16):3005–3008, apr 1996. ISSN 0031-9007. doi:10.1103/PhysRevLett.76.3005.

K. Gawarecki, S. Lüker, D. E. Reiter, T. Kuhn, M. Glässl, V. M. Axt, A. Grodecka-Grad, and P. Machnikowski. Dephasing in the adiabatic rapid passage in quantum dots: Role of phonon-assisted biexciton generation. *Phys. Rev. B*, 86(23):235301, dec 2012. ISSN 1098-0121. doi:10.1103/PhysRevB.86.235301.

I. Gerhardt, G. Wrigge, J. Hwang, G. Zumofen, and V. Sandoghdar. Coherent nonlinear single-molecule microscopy. *Phys. Rev. A*, 82(6):063823, dec 2010. ISSN 1050-2947. doi:10.1103/PhysRevA.82.063823.

C. C. Gerry and P. L. Knight. *Introductory Quantum Optics*. Cambridge University Press, Cambridge, 2005.

N. Gisin, G. Ribordy, W. Tittel, and H. Zbinden. Quantum cryptography. *Rev. Mod. Phys.*, 74(1):145–195, mar 2002. ISSN 0034-6861. doi:10.1103/RevModPhys.74.145.

M. Glässl, M. D. Croitoru, A. Vagov, V. M. Axt, and T. Kuhn. Influence of the pulse shape and the dot size on the decay and reappearance of Rabi rotations in laser driven quantum dots. *Phys. Rev. B*, 84(12): 125304, 2011.

M. Glässl, A. Vagov, S. Lüker, D. E. Reiter, M. D. Croitoru, P. Machnikowski, V. M. Axt, and T. Kuhn. Long-time dynamics and stationary nonequilibrium of an optically driven strongly confined quantum dot coupled to phonons. *Phys. Rev. B*, 84:195311, Nov 2011. doi:10.1103/PhysRevB.84.195311.

M. Glässl, A. M. Barth, and V. M. Axt. Proposed robust and high-fidelity preparation of excitons and biexcitons in semiconductor quantum dots making active use of phonons. *Phys. Rev. Lett.*, 110(14):147401, 2013.

M. Glässl, A. M. Barth, K. Gawarecki, P. Machnikowski, M. D. Croitoru, S. Lüker, D. E. Reiter, T. Kuhn, and V. M. Axt. Biexciton state preparation in a quantum dot via adiabatic rapid passage: Comparison between two control protocols and impact of phonon-induced dephasing. *Phys. Rev. B*, 87(8):085303, 2013. ISSN 10980121. doi:10.1103/PhysRevB.87.085303.

L. Goldstein, F. Glas, J. Y. Marzin, M. N. Charasse, and G. L. Roux. Growth by molecular beam epitaxy and characterization of InAs/GaAs strained-layer superlattices. *Applied Physics Letters*, 47(10):1099–1101, 1985. doi:10.1063/1.96342.

H. Gotoh, H. Sanada, H. Yamaguchi, and T. Sogawa. Direct Biexciton Creation with Two-Photon Excitation for Ideal Entangled Photon Pair Emissions in Optically Active Quantum Dots. *Jpn. J. Appl. Phys.*, 52 (12R):120202, dec 2013. ISSN 0021-4922. doi:10.7567/JJAP.52.120202.

R. Groß. *Festkörperphysik*. Oldenbourg, München, 2012. ISBN 3486712942.

X. Hao, C. Kuang, T. Wang, and X. Liu. Effects of polarization on the de-excitation dark focal spot in STED microscopy. *J. Opt.*, 12(11):115707, nov 2010. ISSN 2040-8978. doi:10.1088/2040-8978/12/11/115707.

B. Harke, J. Keller, C. K. Ullal, V. Westphal, A. Schönle, and S. W. Hell. Resolution scaling in STED microscopy. *Opt. Express*, 16(6):4154, mar 2008. ISSN 1094-4087. doi:10.1364/OE.16.004154.

Y.-M. He, Y. He, Y.-J. Wei, D. Wu, M. Atatüre, C. Schneider, S. Höfling, M. Kamp, C.-Y. Lu, and J.-W. Pan. On-demand semiconductor single-photon source with near-unity indistinguishability. *Nat. Nanotechnol.*, 8 (3):213–217, feb 2013. ISSN 1748-3387. doi:10.1038/nnano.2012.262.

S. W. Hell. Toward fluorescence nanoscopy. *Nat. Biotechnol.*, 21(11):1347–55, 2003. ISSN 1087-0156. doi:10.1038/nbt895.

S. W. Hell. Far-Field Optical Nanoscopy. *Science*, 316(5828):1153–1158, may 2007. ISSN 0036-8075. doi:10.1126/science.1137395.

S. W. Hell. Microscopy and its focal switch. *Nat. Methods*, 6(1):24–32, jan 2009. ISSN 1548-7091. doi:10.1038/nmeth.1291.

S. W. Hell and J. Wichmann. Breaking the diffraction resolution limit by stimulated emission: stimulated-emission-depletion fluorescence microscopy. *Opt. Lett.*, 19(11):780, jun 1994. ISSN 0146-9592. doi:10.1364/OL.19.000780.

J. Houel, A. V. Kuhlmann, L. Greuter, F. Xue, M. Poggio, R. J. Warburton, B. D. Gerardot, P. A. Dalgarno, A. Badolato, P. M. Petroff, A. Ludwig, D. Reuter, and A. D. Wieck. Probing single-charge fluctuations at a GaAs/AlAs interface using laser spectroscopy on a nearby InGaAs quantum dot. *Phys. Rev. Lett.*, 108 (10):1–5, 2012. ISSN 00319007. doi:10.1103/PhysRevLett.108.107401.

H. Y. Hui and R. B. Liu. Proposal for geometric generation of a biexciton in a quantum dot using a chirped pulse. *Phys. Rev. B*, 78:155315, Oct 2008. doi:10.1103/PhysRevB.78.155315.

H. Jayakumar, A. Predojević, T. Huber, T. Kauten, G. S. Solomon, and G. Weihs. Deterministic Photon Pairs and Coherent Optical Control of a Single Quantum Dot. *Phys. Rev. Lett.*, 110(13):135505, mar 2013. ISSN 0031-9007. doi:10.1103/PhysRevLett.110.135505.

V. Jovanov, T. Eissfeller, S. Kapfinger, E. C. Clark, F. Klotz, M. Bichler, J. G. Keizer, P. M. Koenraad, M. S. Brandt, G. Abstreiter, and J. J. Finley. Highly nonlinear excitonic zeeman spin splitting in composition-engineered artificial atoms. *Phys. Rev. B*, 85:165433, Apr 2012. doi:10.1103/PhysRevB.85.165433.

G. Juska, V. Dimastrodonato, L. O. Mereni, A. Gocalinska, and E. Pelucchi. Towards quantum-dot arrays of entangled photon emitters. *Nat. Photonics*, 7(7):527–531, may 2013. ISSN 1749-4885. doi:10.1038/nphoton.2013.128.

T. Kaldewey. *Diploma Thesis - Probing Ultrafast Charge and Spin Dynamics in a Single Self-Assembled Quantum Dot*. Technical University Munich, 2012.

T. A. Klar and S. W. Hell. Subdiffraction resolution in far-field fluorescence microscopy. *Opt. Lett.*, 24(14): 954–956, jul 1999. doi:10.1364/OL.24.000954.

T. A. Klar, S. Jakobs, M. Dyba, A. Egner, and S. W. Hell. Fluorescence microscopy with diffraction resolution barrier broken by stimulated emission. *Proceedings of the National Academy of Sciences*, 97 (15):8206–8210, 2000. ISSN 0027-8424. doi:10.1073/pnas.97.15.8206.

K. Kowalik, O. Krebs, A. Lemaître, S. Laurent, P. Senellart, P. Voisin, and J. A. Gaj. Influence of an in-plane electric field on exciton fine structure in InAs-GaAs self-assembled quantum dots. *Appl. Phys. Lett.*, 86(4):041907, 2005. ISSN 00036951. doi:10.1063/1.1855409.

H. J. Krenner, S. Stufler, M. Sabathil, E. C. Clark, P. Ester, M. Bichler, G. Abstreiter, J. J. Finley, and A. Zrenner. Recent advances in exciton-based quantum information processing in quantum dot nanostructures. *New Journal of Physics*, 7(1):184, 2005.

A. Krügel, V. M. Axt, T. Kuhn, P. Machnikowski, and A. Vagov. The role of acoustic phonons for Rabi oscillations in semiconductor quantum dots. *Appl. Phys. B*, 81:897, 2005. ISSN 1432-0649. doi:10.1007/s00340-005-1984-1. URL `http://dx.doi.org/10.1007/s00340-005-1984-1`.

A. Krügel, V. M. Axt, and T. Kuhn. Back action of nonequilibrium phonons on the optically induced dynamics in semiconductor quantum dots. *Phys. Rev. B*, 73(3):035302, 2006.

A. V. Kuhlmann, J. Houel, D. Brunner, A. Ludwig, D. Reuter, A. D. Wieck, and R. J. Warburton. A dark-field microscope for background-free detection of resonance fluorescence from single semiconductor quantum dots operating in a set-and-forget mode. *Rev. Sci. Instrum.*, 84(7):073905, 2013a. ISSN 00346748. doi:10.1063/1.4813879.

A. V. Kuhlmann, J. Houel, A. Ludwig, L. Greuter, D. Reuter, A. D. Wieck, M. Poggio, and R. J. Warburton. Charge noise and spin noise in a semiconductor quantum device. *Nat. Phys.*, 9(9):570–575, 2013b. ISSN 1745-2473. doi:10.1038/nphys2688.

A. Kurzmann, A. Ludwig, A. D. Wieck, A. Lorke, and M. Geller. Auger Recombination in Self-Assembled Quantum Dots: Quenching and Broadening of the Charged Exciton Transition. *Nano Lett.*, 16(5): 3367–3372, 2016. ISSN 15306992. doi:10.1021/acs.nanolett.6b01082.

P. G. Kwiat, K. Mattle, H. Weinfurter, A. Zeilinger, A. V. Sergienko, and Y. Shih. New High-Intensity Source of Polarization-Entangled Photon Pairs. *Phys. Rev. Lett.*, 75(24):4337–4341, dec 1995. ISSN 0031-9007. doi:10.1103/PhysRevLett.75.4337.

L. Landau. On the theory of transfer of energy at collisions II. *Phys. Z. Sowjetunion*, 2:46, 1932.

W. Langbein, P. Borri, U. Woggon, V. Stavarache, D. Reuter, and A. D. Wieck. Control of fine-structure splitting and biexciton binding in $in_xga_{1-x}As$ quantum dots by annealing. *Phys. Rev. B*, 69:161301, Apr 2004. doi:10.1103/PhysRevB.69.161301.

H. Li, Q. Zhuang, Z. Wang, and T. Daniels-Race. Influence of indium composition on the surface morphology of self-organized in[sub x]ga[sub 1 - x]as quantum dots on gaas substrates. *Journal of Applied Physics*, 87 (1):188–191, 2000a. doi:10.1063/1.371842.

H. Li, Q. Zhuang, Z. Wang, and T. Daniels-Race. Influence of indium composition on the surface morphology of self-organized $In_xGa_{1-x}As$ quantum dots on GaAs substrates. *Journal of Applied Physics*, 87(1): 188–191, 2000b. doi:10.1063/1.371842.

D. Loss and D. P. DiVincenzo. Quantum computation with quantum dots. *Phys. Rev. A*, 57(1):120–126, jan 1998. ISSN 1050-2947. doi:10.1103/PhysRevA.57.120.

M. M. T. Loy. Observation of population inversion by optical adiabatic rapid passage. *Phys. Rev. Lett.*, 32: 814–817, Apr 1974. doi:10.1103/PhysRevLett.32.814.

S. Lüker, K. Gawarecki, D. E. Reiter, A. Grodecka-Grad, V. M. Axt, P. Machnikowski, and T. Kuhn. Influence of acoustic phonons on the optical control of quantum dots driven by adiabatic rapid passage. *Phys. Rev. B*, 85(12):121302, mar 2012. ISSN 1098-0121. doi:10.1103/PhysRevB.85.121302.

P. Machnikowski and L. Jacak. Resonant nature of phonon-induced damping of rabi oscillations in quantum dots. *Phys. Rev. B*, 69:193302, 2004.

V. S. Malinovsky and J. L. Krause. General theory of population transfer by adiabatic rapid passage with intense, chirped laser pulse. *Eur. Phys. J. D*, 14(2):147, 2001. ISSN 1434-6079. doi:10.1007/s100530170212.

J. Márquez, L. Geelhaar, and K. Jacobi. Atomically resolved structure of InAs quantum dots. *Applied Physics Letters*, 78(16):2309–2311, 2001. doi:10.1063/1.1365101.

O. Martinez. 3000 times grating compressor with positive group velocity dispersion: Application to fiber compensation in 1.3-1.6 μm region. *IEEE J. Quantum Electron.*, 23(1):59–64, 1987. ISSN 0018-9197. doi:10.1109/JQE.1987.1073201.

R. Mathew, E. Dilcher, A. Gamouras, A. Ramachandran, H. Y. S. Yang, S. Freisem, D. Deppe, and K. C. Hall. Subpicosecond adiabatic rapid passage on a single semiconductor quantum dot: Phonon-mediated dephasing in the strong-driving regime. *Phys. Rev. B*, 90(3):035316, jul 2014. ISSN 1098-0121. doi:10.1103/PhysRevB.90.035316.

C. Matthiesen, A. N. Vamivakas, and M. Atatüre. Subnatural Linewidth Single Photons from a Quantum Dot. *Phys. Rev. Lett.*, 108(9):093602, feb 2012. ISSN 0031-9007. doi:10.1103/PhysRevLett.108.093602.

J. S. Melinger, S. R. Gandhi, A. Hariharan, D. Goswami, and W. S. Warren. Adiabatic population transfer with frequency-swept laser pulses. *The Journal of Chemical Physics*, 101(8):6439–6454, 1994. doi:10.1063/1.468368.

P. Michler, A. Kiraz, C. Becher, W. V. Schoenfeld, P. M. Petroff, L. Zhang, E. Hu, and A. Imamoglu. A quantum dot single-photon turnstile device. *Science*, 290(5500):2282–2285, 2000. ISSN 0036-8075. doi:10.1126/science.290.5500.2282.

P. W. Milonni and J. H. Eberly. *Lasers (Wiley Series in Pure and Applied Optics)*. Wiley-Blackwell, 12 1988. ISBN 9780471627319.

A. Muller, E. B. Flagg, P. Bianucci, X. Y. Wang, D. G. Deppe, W. Ma, J. Zhang, G. J. Salamo, M. Xiao, and C. K. Shih. Resonance Fluorescence from a Coherently Driven Semiconductor Quantum Dot in a Cavity. *Phys. Rev. Lett.*, 99(18):187402, nov 2007. ISSN 0031-9007. doi:10.1103/PhysRevLett.99.187402.

M. Müller, S. Bounouar, K. D. Jöns, M. Glässl, and P. Michler. On-demand generation of indistinguishable polarization-entangled photon pairs. *Nat. Photonics*, 8(3):224–228, feb 2014. ISSN 1749-4885. doi:10.1038/nphoton.2013.377.

B. Neupane, F. Chen, W. Sun, D. T. Chiu, and G. Wang. Tuning donut profile for spatial resolution in stimulated emission depletion microscopy. *Rev. Sci. Instrum.*, 84(4):043701, apr 2013. ISSN 1089-7623. doi:10.1063/1.4799665.

H. S. Nguyen, G. Sallen, C. Voisin, P. Roussignol, C. Diederichs, and G. Cassabois. Ultra-coherent single photon source. *Appl. Phys. Lett.*, 99(26):261904, 2011. ISSN 00036951. doi:10.1063/1.3672034.

B. Patton, U. Woggon, and W. Langbein. Coherent control and polarization readout of individual excitonic states. *Phys. Rev. Lett.*, 95(26):266401, dec 2005. ISSN 0031-9007. doi:10.1103/PhysRevLett.95.266401.

J. H. Prechtel, A. V. Kuhlmann, J. Houel, A. Ludwig, S. R. Valentin, A. D. Wieck, and R. J. Warburton. Decoupling a hole spin qubit from the nuclear spins. *Nat. Mater.*, 15(9):981–986, jul 2016. ISSN 1476-1122. doi:10.1038/nmat4704.

J. H. Quilter, A. J. Brash, F. Liu, M. Glässl, A. M. Barth, V. M. Axt, A. J. Ramsay, M. S. Skolnick, and A. M. Fox. Phonon-assisted population inversion of a single InGaAs/GaAs quantum dot by pulsed laser excitation. *Phys. Rev. Lett.*, 114(13):137401, 2015. ISSN 0031-9007. doi:10.1103/PhysRevLett.114.137401.

A. J. Ramsay. A review of the coherent optical control of the exciton and spin states of semiconductor quantum dots. *Semicond. Sci. Technol.*, 25(10):103001, 2010.

A. J. Ramsay, T. M. Godden, S. J. Boyle, E. M. Gauger, A. Nazir, B. W. Lovett, A. M. Fox, and M. S. Skolnick. Phonon-induced Rabi-frequency renormalization of optically driven single InGaAs/GaAs quantum dots. *Phys. Rev. Lett.*, 105(17):177402, oct 2010a. ISSN 0031-9007. doi:10.1103/PhysRevLett.105.177402.

A. J. Ramsay, A. V. Gopal, E. M. Gauger, A. Nazir, B. W. Lovett, A. M. Fox, and M. S. Skolnick. Damping of exciton Rabi rotations by acoustic phonons in optically excited InGaAs/GaAs quantum dots. *Phys. Rev. Lett.*, 104(1):017402, jan 2010b. ISSN 0031-9007. doi:10.1103/PhysRevLett.104.017402.

D. E. Reiter, S. Lüker, K. Gawarecki, A. Grodecka-Grad, P. Machnikowski, V. M. Axt, and T. Kuhn. Phonon effects on population inversion in quantum dots: Resonant, detuned and frequency-swept excitations. *Acta Phys. Pol. A*, 122(6):1065–1068, 2012. ISSN 05874246.

D. E. Reiter, T. Kuhn, M. Glässl, and V. M. Axt. The role of phonons for exciton and biexciton generation in an optically driven quantum dot. *J. Phys. Condens. Matter*, 26(42):423203, oct 2014. ISSN 0953-8984. doi:10.1088/0953-8984/26/42/423203.

E. Rittweger, K. Y. Han, S. E. Irvine, C. Eggeling, and S. W. Hell. STED microscopy reveals crystal colour centres with nanometric resolution. *Nat. Photonics*, 3(3):144–147, mar 2009. ISSN 1749-4885. doi:10.1038/nphoton.2009.2.

S. Rodt, A. Schliwa, K. Pötschke, F. Guffarth, and D. Bimberg. Correlation of structural and few-particle properties of self-organized InAs/GaAs quantum dots. *Phys. Rev. B*, 71(15):155325, apr 2005. ISSN 1098-0121. doi:10.1103/PhysRevB.71.155325.

M. J. Rust, M. Bates, and X. W. Zhuang. Sub-diffraction-limit imaging by stochastic optical reconstruction microscopy (STORM). *Nat Methods*, 3(10):793–795, 2006. ISSN 1548-7091. doi:10.1038/Nmeth929.

S. Seidl, B. Gerardot, P. Dalgarno, K. Kowalik, A. Holleitner, P. Petroff, K. Karrai, and R. Warburton. Statistics of quantum dot exciton fine structure splittings and their polarization orientations. *Phys. E Low-dimensional Syst. Nanostructures*, 40(6):2153–2155, apr 2008. ISSN 13869477. doi:10.1016/j.physe.2007.10.046.

K. A. Serrels, E. Ramsay, P. A. Dalgarno, B. Gerardot, J. O'Connor, R. H. Hadfield, R. J. Warburton, and D. Reid. Solid immersion lens applications for nanophotonic devices. *Journal of Nanophotonics*, 2(1): 021854–021854–29, 2008. doi:10.1117/1.3068652.

S. Shevchenko, S. Ashhab, and F. Nori. Landau-Zener-Stückelberg interferometry. *Phys. Rep.*, 492(1):1–30, jul 2010. ISSN 03701573. doi:10.1016/j.physrep.2010.03.002.

C.-M. Simon, T. Belhadj, B. Chatel, T. Amand, P. Renucci, A. Lemaître, O. Krebs, P. A. Dalgarno, R. J. Warburton, X. Marie, and B. Urbaszek. Robust Quantum Dot Exciton Generation via Adiabatic Passage with Frequency-Swept Optical Pulses. *Phys. Rev. Lett.*, 106(16):166801, apr 2011. ISSN 0031-9007. doi:10.1103/PhysRevLett.106.166801.

T. Skauli, P. S. Kuo, K. L. Vodopyanov, T. J. Pinguet, O. Levi, L. A. Eyres, J. S. Harris, M. M. Fejer, B. Gerard, L. Becouarn, and E. Lallier. Improved dispersion relations for GaAs and applications to nonlinear optics. *J. Appl. Phys.*, 94(10):6447–6455, 2003. ISSN 00218979. doi:10.1063/1.1621740.

R. M. Stevenson, R. J. Young, P. See, D. G. Gevaux, K. Cooper, P. Atkinson, I. Farrer, D. A. Ritchie, and A. J. Shields. Magnetic-field-induced reduction of the exciton polarization splitting in InAs quantum dots. *Phys. Rev. B*, 73(3):033306, jan 2006. ISSN 1098-0121. doi:10.1103/PhysRevB.73.033306.

T. H. Stievater, X. Li, D. G. Steel, D. Gammon, D. S. Katzer, D. Park, C. Piermarocchi, and L. J. Sham. Rabi oscillations of excitons in single quantum dots. *Phys. Rev. Lett.*, 87:133603, Sep 2001. doi:10.1103/PhysRevLett.87.133603.

S. Stufler, P. Ester, A. Zrenner, and M. Bichler. Quantum optical properties of a single $In_xGa_{1-x}As/GaAs$ quantum dot two-level system. *Phys. Rev. B*, 72:121301, Sep 2005. doi:10.1103/PhysRevB.72.121301.

S. Stufler, P. Machnikowski, P. Ester, M. Bichler, V. M. Axt, T. Kuhn, and A. Zrenner. Two-photon rabi oscillations in a single $In_xGa_{1-x}As/GaAs$ quantum dot. *Phys. Rev. B*, 73:125304, Mar 2006a. doi:10.1103/PhysRevB.73.125304.

S. Stufler, P. Machnikowski, P. Ester, M. Bichler, V. M. Axt, T. Kuhn, and A. Zrenner. Two-photon Rabi oscillations in a single Inx Ga1-x As GaAs quantum dot. *Phys. Rev. B*, 73(12):1–7, 2006b. ISSN 10980121. doi:10.1103/PhysRevB.73.125304.

A. I. Tartakovskii, J. Cahill, M. N. Makhonin, D. M. Whittaker, J.-P. R. Wells, A. M. Fox, D. J. Mowbray, M. S. Skolnick, K. M. Groom, M. J. Steer, and M. Hopkinson. Dynamics of Coherent and Incoherent Spin Polarizations in Ensembles of Quantum Dots. *Phys. Rev. Lett.*, 93(5):057401, jul 2004. ISSN 0031-9007. doi:10.1103/PhysRevLett.93.057401.

R. Trotta, J. S. Wildmann, E. Zallo, O. G. Schmidt, and A. Rastelli. Highly Entangled Photons from Hybrid Piezoelectric-Semiconductor Quantum Dot Devices. *Nano Lett.*, 14(6):3439–3444, jun 2014. ISSN 1530-6984. doi:10.1021/nl500968k.

A. Vagov, M. D. Croitoru, V. M. Axt, T. Kuhn, and F. M. Peeters. Nonmonotonic field dependence of damping and reappearance of Rabi oscillations in quantum dots. *Phys. Rev. Lett.*, 98:227403, Jun 2007. doi:10.1103/PhysRevLett.98.227403.

A. N. Vamivakas, Y. Zhao, C.-Y. Lu, and M. Atatüre. Spin-resolved quantum-dot resonance fluorescence. *Nat. Phys.*, 5(3):198–202, mar 2009. ISSN 1745-2473. doi:10.1038/nphys1182.

R. J. Warburton. Single spins in self-assembled quantum dots. *Nat. Mater.*, 12(6):483–493, may 2013. ISSN 1476-1122. doi:10.1038/nmat3585.

R. J. Warburton, B. T. Miller, C. S. Dürr, C. Bödefeld, K. Karrai, J. P. Kotthaus, G. Medeiros-Ribeiro, P. M. Petroff, and S. Huant. Coulomb interactions in small charge-tunable quantum dots: A simple model. *Phys. Rev. B*, 58:16221–16231, Dec 1998. doi:10.1103/PhysRevB.58.16221.

R. J. Warburton, C. Schäflein, D. Haft, F. Bickel, A. Lorke, K. Karrai, J. M. Garcia, W. Schoenfeld, and P. M. Petroff. Optical emission from a charge-tunable quantum ring. *Nature*, 405(6789):926–9, 2000. ISSN 1476-4687. doi:10.1038/35016030.

R. J. Warburton, C. Schulhauser, D. Haft, C. Schäflein, K. Karrai, J. M. Garcia, W. Schoenfeld, and P. M. Petroff. Giant permanent dipole moments of excitons in semiconductor nanostructures. *Phys. Rev. B*, 65 (11):113303, 2002.

Y.-J. Wei, Y.-M. He, M.-C. Chen, Y.-N. Hu, Y. He, D. Wu, C. Schneider, M. Kamp, S. Höfling, C.-Y. Lu, and J.-W. Pan. Deterministic and Robust Generation of Single Photons from a Single Quantum Dot with 99.5% Indistinguishability Using Adiabatic Rapid Passage. *Nano Lett.*, 14(11):6515–6519, nov 2014. ISSN 1530-6984. doi:10.1021/nl503081n.

A. M. Weiner. Femtosecond pulse shaping using spatial light modulators. *Rev. Sci. Instrum.*, 71(5):1929–1960, 2000. doi:10.1063/1.1150614.

A. M. Weiner. *Ultrafast Optics*. Wiley, Hoboken, N.J, 2009. ISBN 0471415391.

A. M. Weiner, D. E. Leaird, J. S. Patel, and J. R. Wullert. Programmable shaping of femtosecond optical pulses by use of 128-element liquid crystal phase modulator. *IEEE J. Quantum Electron.*, 28(4):908–920, apr 1992. ISSN 00189197. doi:10.1109/3.135209.

S. Weisenburger and V. Sandoghdar. Light microscopy: an ongoing contemporary revolution. *Contemp. Phys.*, 56(2):123–143, apr 2015. ISSN 0010-7514. doi:10.1080/00107514.2015.1026557.

V. Westphal and S. W. Hell. Nanoscale resolution in the focal plane of an optical microscope. *Phys. Rev. Lett.*, 94(14):1–4, 2005. ISSN 00319007. doi:10.1103/PhysRevLett.94.143903.

D. Wigger, S. Lüker, D. E. Reiter, V. M. Axt, P. Machnikowski, and T. Kuhn. Energy transport and coherence properties of acoustic phonons generated by optical excitation of a quantum dot. *J. Phys. Condens. Matter*, 26(35):355802, 2014. ISSN 1361-648X. doi:10.1088/0953-8984/26/35/355802.

D. Wildanger, J. R. Maze, and S. W. Hell. Diffraction Unlimited All-Optical Recording of Electron Spin Resonances. *Phys. Rev. Lett.*, 107(1):17601, jul 2011. doi:10.1103/PhysRevLett.107.017601.

D. Wildanger, B. R. Patton, H. Schill, L. Marseglia, J. P. Hadden, S. Knauer, A. Schönle, J. G. Rarity, J. L. O'Brien, S. W. Hell, and J. M. Smith. Solid Immersion Facilitates Fluorescence Microscopy with Nanometer Resolution and Sub-Ångström Emitter Localization. *Adv. Mater.*, 24(44):OP309—-OP313, 2012. ISSN 1521-4095. doi:10.1002/adma.201203033.

K. I. Willig, B. Harke, R. Medda, and S. W. Hell. STED microscopy with continuous wave beams. *Nat. Methods*, 4(11):915–918, nov 2007. ISSN 1548-7091. doi:10.1038/nmeth1108.

Y. Wu, I. M. Piper, M. Ediger, P. Brereton, E. R. Schmidgall, P. R. Eastham, M. Hugues, M. Hopkinson, and R. T. Phillips. Population Inversion in a Single InGaAs Quantum Dot Using the Method of Adiabatic Rapid Passage. *Phys. Rev. Lett.*, 106(6):067401, feb 2011. ISSN 0031-9007. doi:10.1103/PhysRevLett.106.067401.

S. T. Yilmaz, P. Fallahi, and A. Imamoglu. Quantum-Dot-Spin Single-Photon Interface. *Phys. Rev. Lett.*, 105(3):033601, jul 2010. ISSN 0031-9007. doi:10.1103/PhysRevLett.105.033601.

R. J. Young, R. M. Stevenson, A. J. Shields, P. Atkinson, K. Cooper, D. A. Ritchie, K. M. Groom, A. I. Tartakovskii, and M. S. Skolnick. Inversion of exciton level splitting in quantum dots. *Phys. Rev. B*, 72 (11):113305, sep 2005. ISSN 1098-0121. doi:10.1103/PhysRevB.72.113305.

M. Zecherle, C. Ruppert, E. C. Clark, G. Abstreiter, J. J. Finley, and M. Betz. Ultrafast few-fermion optoelectronics in a single self-assembled InGaAs/GaAs quantum dot. *Phys. Rev. B*, 82:125314, Sep 2010. doi:10.1103/PhysRevB.82.125314.

C. Zener. Non-Adiabatic Crossing of Energy Levels. *Proc. R. Soc. A Math. Phys. Eng. Sci.*, 137(833): 696–702, 1932. ISSN 1364-5021. doi:10.1098/rspa.1932.0165.

S. Zhdanovich, E. A. Shapiro, M. Shapiro, J. W. Hepburn, and V. Milner. Population transfer between two quantum states by piecewise chirping of femtosecond pulses: Theory and experiment. *Phys. Rev. Lett.*, 100:103004, Mar 2008. doi:10.1103/PhysRevLett.100.103004.

A. Zrenner, E. Beham, S. Stufler, F. Findeis, M. Bichler, and G. Abstreiter. Coherent properties of a two-level system based on a quantum-dot photodiode. *Nature*, 418(6898):612–614, aug 2002. ISSN 0028-0836. doi:10.1038/nature00912.